Development of three-dimensional, *ex vivo* optical imaging

Angela Maria d'Esposito, MPhys, MRes.

Submitted for the degree of

Doctor of Philosophy in Medical Physics

June 2016

Department of Medical Physics and Biomedical Engineering
and
Centre for Advanced Biomedical Imaging, Division of Medicine
University College London

it's all about which way you look

Declaration

I, Angela Maria d'Esposito, confirm that the work presented in this thesis is my own, except where stated otherwise in the text. This work is based on research which has been conducted by me during the time period from October 2012 to September 2015 at University College London.

Angela Maria d'Esposito
June 2016

Abstract

The ability to analyse tissue in 3-D at the mesoscopic scale (resolution: 2-50 μm) has proven essential in the study of whole specimens and individual organs. Techniques such as *ex vivo* magnetic resonance imaging (MRI) and X-ray computed tomography (CT) have been successful in a number of applications. Although MRI has been used to image embryo development and gene expression in 3-D, its resolution is not sufficient to discriminate between the small structures in embryos and individual organs. Furthermore, since neither MRI nor X-ray CT are optical imaging techniques, none of them is able to make use of common staining techniques. 3-D images can be generated with confocal microscopy by focusing a laser beam to a point within the sample and collecting the fluorescent light coming from that specific plane, eliminating therefore out-of-focus light. However, the main drawback of this microscopy technique is the limited depth penetration of light (~1 mm). Tomographic techniques such as optical projection tomography (OPT) and light sheet fluorescence microscopy (also known as single plane illumination microscopy, SPIM) are novel methods that fulfil a requirement for imaging of specimens which are too large for confocal imaging and too small for conventional MRI. To allow sufficient depth penetration, these approaches require specimens to be rendered transparent via a process known as optical clearing, which can be achieved using a number of techniques.

The aim of the work presented in this thesis was to develop methods for three-dimensional, *ex vivo* optical imaging. This required, in first instance, sample preparation to clear (render transparent) biological tissue. In this project several optical clearing techniques have been tested in order to find the optimal method per each kind of tissue, focusing on tumour tissue. Indeed, depending on its structure and composition (e.g. amount of lipids or pigments within the tissue) every tissue clears at a different degree. Though there is currently no literature reporting quantification of the degree of optical clearing. Hence a novel, spectroscopic technique for measuring the light attenuation in optically cleared samples is described in this thesis and evaluated on mouse brain.

Optical clearing was applied to the study of cancer. The main cancer model investigated in this report is colorectal carcinoma. Fluorescently labelled proteins were used to analyse the vascular network of colorectal xenograft tumours and to prove the effect of vascular disrupting agents on the vascular tumour network. Furthermore, optical clearing and fluorescent compounds were used for *ex vivo* analysis of perfusion of a human colorectal liver metastasis model.

Acknowledgements

My special thanks are directed towards my supervisors Dr Simon Walker-Samuel, Professor Mark Lythgoe and Dr Adrien Desjardins for their precious advice and support. Most of all, I am indebted to Dr Simon Walker-Samuel, who phoned me all the way to Thailand to invite me to work on my PhD in London at CABI. Since then, he has always been extremely encouraging, especially after suggesting to work on yet another of the hundreds brilliant but also crazy ideas he has! I could not imagine my PhD without him on my side. Many thanks to Dr Adrien Desjardins for his highly valuable technical advice and to Professor Mark Lythgoe for his exceptional support. I cannot thank him enough for all the guidance he gave me, both at work and in everyday life when the sea was rough.

A special mention must be passed to Dr Bertrand Vernay from UCL Institute for Child Health, who has been a collaborator and a friend. He has not only introduced me to the magical world of microscopy, but has also inspired me with his curiosity and taught me a lot in the beginning of my Phd, when everything was new and it was easy to feel lost.

I am appreciative to have had the opportunity to work with all my colleagues and friends at CABI. I feel they have all put at least one piece of the puzzle which is both my PhD and the person I am today. Especially, I would like to acknowledge Val for her powerful hugs; Laurence, who I have already proclaimed “the best desk neighbour ever”; Raj and Tom who are the funniest scientists I know and made everything smoother and even more enjoyable; Morium for her precious help in the lab. I am thankful to have had Peter Johnson around as a cool collaborator. He is the one who taught me all I know in surgery. I would also like to thank John, Ana, Oz and May for being there.

I am grateful to all my friends for their love. Especially, I want to mention Elda, Federica, Cleo, Gül, Thomas, Sara, Maura, Gabi, Claudia, and Simone.

And am grateful for Umb., the oak which one day came (back) up in the garden of my life.

Big thanks go to my family who, despite the initial startling surprise, has always supported my life choices, one after the other, and has always been there for me.

Publications and conference proceedings from research conducted

Publications

d'Esposito A, Nikitichev D, Desjardins A, Walker-Samuel S, Lythgoe MF, "Quantification of light attenuation in optically cleared mouse brains", *Journal of Biomedical Optics*, 20(8): 80503 (2015)

Brzóska HL, **d'Esposito A**, Kolatsi-Joannou M, Patel V, Igarashi P, Finnell RH, Lythgoe MF, Woolf AS, Papakrivopoulou E, Long DA, "Planar cell polarity genes *Celsr1* and *Vangl2* control mammalian kidney growth, differentiation and rostrocaudal patterning", *Kidney International*- in press.

Portions of chapter 5 are in process of being submitted for publication to the paper: "Numerical simulation and experimental validation of vascular-targeting therapy using whole-tumour optical imaging data", **d'Esposito A**, Sweeney P, Desjardins A, Lythgoe M, Pedley B, Shipley R, Walker-Samuel S.

Conference proceedings

L. Jackson, **A. d'Esposito**, B. Siow, D. Stuckey, M. Lythgoe, "*Ex vivo* Cardiac Fibre Imaging using Diffusion MRI and Optical Projection Tomography", Proc Intl Soc Mag Reson Med. 2012

A. d'Esposito, D. Nikitichev , A. Desjardins, S. Walker-Samuel, M.F. Lythgoe, "To what extent is your tissue clear? Optical clearing and absorbance quantitation in the mouse brain", Proc Eur Mol Im Congr 2014

A. d'Esposito, D. Nikitichev , A. Desjardins, S. Walker-Samuel, M.F. Lythgoe, "Light attenuation quantitation in the mouse brain", Proc REMOA 2014

P. Sweeney, **A. d'Esposito**, R. Ramasawmy, S. Walker-Samuel, R. Shipley, "Mathematical modelling of blood perfusion and oxygenation in microvascular networks with applications in stroke research", Proc ISOTT 2014

A. d'Esposito, D. Nikitichev , A. Desjardins, S. Walker-Samuel, M.F. Lythgoe, "Optical clearing of the mouse brain and light attenuation quantitation", Proc. SPIE 9321, Optical Interactions with Tissue and Cells XXVI, 93210R, 2015

A. d'Esposito, R. Ramasawmy, T.A. Roberts, S.P. Johnson, A. Desjardin, M.F. Lythgoe, S. Walker-Samuel, "Three dimensional in *vivo* and *ex vivo* visualization of metastatic liver vasculature with Magnetic Resonance Imaging and Optical Projection Tomography", Proc World Mol Im Congr 2015

A. d'Esposito, P. Johnson, B. Pedley, A. Desjardins, M. Lythgoe, S. Walker-Samuel, "Optical projection tomography for three-dimensional analysis of cancer models following anti-vascular therapy", Proc Foc on Mic 2016

M. Ali, A. Gomez Ramirez, **A. d'Esposito**, T. L. Kalber, Mark F. Lythgoe, "Imaging Fluorescent Cells within the Brain Using Optical projection tomography", Proc World Mol Im Congr 2016

Table of Contents

List of figures

List of tables

List of Abbreviations

BABB	Benzyl Alcohol- Benzyl Benzoate
BSA	Bovine Serum Albumin
CA	Carbonic Anhydrase
CCD	Charged Coupled Device
CLSM	Confocal Laser Scanning Microscopy
CMOS	Complementary Metal Oxide Semiconductor
COLM	CLARITY- Optimized Light-sheet Microscopy
COSM	Computational Optical Sectioning Microscopy
CRC	Colorectal Cancer
CT	Computerized Tomography
DBE	Dibenzyl Ether
DMSO	Dimethyl Sulfoxide
EM	Electron Microscopy
ETC	Electrophoretic Tissue Clearing
FITC	Fluorescein Isothiocyanate
FOV	Field Of View
FRET	Forster (or Fluorescence) Resonance Energy Transfer
GFP	Green Fluorescent Protein
HCC	Hepatocellular Carcinoma
IFP	Interstitial Fluid Pressure
IFV	Interstitial Fluid Velocity
IVC	Individually Ventilated Cage

IVC	Inferior Vena Cava
IV injection	Intravenous injection
IP injection	Intraperitoneal injection
LP filter	Long Pass filter
LSFM	Light Sheet Fluorescence Microscopy
μCT	Micro-Computed Tomography
μMRI	Micro-Magnetic Resonance Imaging
MFP	Mean Free Path
MRI	Magnetic Resonance Imaging
NA	Numerical Aperture
ND filter	Neutral Density filter
NIR	Near InfraRed
OCA	Optical Clearing Agent
OCT	Optical Coherence Tomography
OCP	Optical Clearing Potential
OPFOS	Orthogonal-Plane Fluorescence Optical Sectioning
OPT	Optical Projection Tomography
PA	Photoacustic
PBS	Phosphate Buffered Saline
PET	Positron Emission Tomography
PFA	Paraformaldehyde
PTFA	Polytetrafluoroethylene
QE	Quantum Efficiency

RF	Radio Frequency
RT	Room Temperature
SDS	Sodium Dodecyl Sulfate
SEM	Scanning Electron Microscopy
SNR	Signal to Noise Ratio
SPIM	Selective Plane Illumination Microscopy
STED	Stimulated Emission Depletion
TBF	Tumour Blood Flow
THF	Tetrahydrofuran
TMFP	Transport Mean Free Path
TOC	Tissue Optical Clearing
TRITC	Tetramethyl Rhodamine Isothiocyanate
TTC	2,3,5-Triphenyltetrazolium chloride
US	Ultrasounds
VDA	Vascular Disrupting Agent
VEGF	Vascular Endothelial Growth Factor
2 PM	Two Photon Microscopy
2-D	Two dimensional
3-D	Three dimensional

Chapter 1: Introduction, theory and background

The aim of this chapter is to provide an overview of the thesis structure and its aims as well as of relevant background theory. The principles of optical imaging are introduced, and the most relevant imaging techniques for this research are discussed. This includes wide-field, confocal and multiphoton microscopy, light sheet fluorescence microscopy, and particular emphasis is given to optical projection tomography, which was extensively used in this thesis. For each of these techniques, the operational principle is illustrated and their applications are discussed. Optical clearing of tissue samples is also introduced. The principles of light attenuation in tissues are discussed, and several recently developed optical clearing techniques are covered.

1.1 Biomedical imaging

Imaging sciences have nowadays become indispensible for both fundamental cell biological research and clinical practice. They have developed from a means of obtaining simple anatomical or topographical information, to powerful instruments for the investigation of function in organs and whole organisms. By determining profiles of biological macromolecules, associations can be made with a given condition and followed during the course of a metabolic change such as signalling, growth, development and, in particular, during the onset of disease. Living organisms exist in a time-evolving 3-dimensional (3-D) space; accordingly, to understand their behaviour or function (and/or to assess their health), information must be accrued over similar dimensions. Thus, many novel imaging modalities have emerged to address function across many length/volume scales, depending on the relevant biological or biomedical demand.

Imaging is essentially a measurement made over a defined region with the prominence of spatial/volume discrimination. There are major demands and challenges to the acquisition of images. Some of these reside in the need to acquire information from noisy backgrounds, or at a considerable depth within the body. These problems are common to all the imaging techniques described in this chapter, with tailored practical solutions arising for each imaging modality.

1.1.1 Principles of CT, US and MRI

In this section, some of the imaging modalities most commonly used to visualize and study anatomical structures are described. These include computerized tomography (CT), ultrasound (US), and magnetic resonance imaging (MRI).

1.1.1.1 Tomography and reconstruction with back projection

The word tomography is derived from the Greek τόμος (*tomos*, cut or slice) and γράφω (*graphō*, to write) and it refers to imaging techniques that are able to recreate a 3-D object from sections or projections formed by the detection of a penetrating wave.

In most of the technologies labelled as tomography, various types of beams are either transmitted through or emitted from the specimen. The rays in question (X-rays for CT and μCT, visible light for optical projection tomography, OPT) pass through the sample in straight lines that approximate projections (1). The attenuation of rays or the emission of photons along each projection are measured, then a back-projection algorithm (2) is used to reconstruct the distribution of either absorbance or emission. This involves backprojecting an individual sample by setting all the image pixels along the ray pinpointing to the sample to the same value, hence projecting each view back through the image in the direction it was originally acquired. The final backprojected image is then taken as the sum of all the backprojected views. Since the projections are straight lines, one of the methods that can be used to solve this inverse problem is the Radon transform (2). As the reconstructed image appears blurry, a filtered backprojection is used in order to improve the quality of this backprojection. Each of the one-dimensional views is convolved with a one-dimensional filter mask to create a set of filtered views, which are then backprojected to provide the reconstructed image. Standard tomographic algorithms and modified back-projection, which is the approach used by OPT, are described in section 3.2.

1.1.1.2 Computerized tomography

In X-ray CT, a motorized table moves the patient through a circular opening in the CT imaging system (Figure 1.1). As the patient passes through, a source of X-rays rotates around the inside of the circular opening. A single rotation typically takes about 1 second. The X-ray source produces a narrow, fan-shaped beam of X-rays used to irradiate a section of the patient's body. The thickness of the fan beam may be as small as 1 mm or as large as 10 mm. Detectors on the opposite side of the patient record the x rays exiting the section of the patient's body being irradiated as an X-ray image at one angle of the source of X-rays. Many different views are collected during one complete rotation. The data are then sent to a computer to be reconstructed with a back-projection algorithm into a cross-sectional image of the internal organs and tissues for each complete rotation of the source of X-rays. In X-ray CT, the contrast within the body is provided by intrinsic differences in X-ray absorption between water, bone, fat, and air. The high-energy waves used in X-ray CT are termed *ionizing radiation* because they contain sufficient energy to displace

an electron from its orbit around a nucleus. The most important consequence of this displaced electron on human tissue is the potential damage it can inflict on DNA. This can have several consequences on the human body. For instance, leukaemia and most solid cancers have been linked with radiation and DNA damage (3, 4). However, the exposure of the specimen to damaging ionizing radiation is a limitation of CT only when used for imaging live organisms.

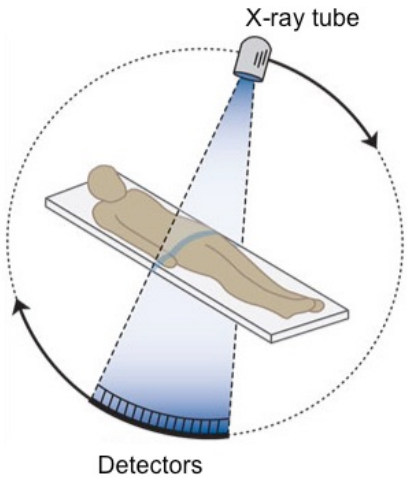

Figure 1.1: Functioning principle of X-ray CT. A beam of X-rays is used to irradiate a section of the patient's body. The X rays exiting the section of the patient's body are recorded on an array of detectors and used to form an image.

1.1.1.3 Ultrasound imaging

Ultrasound imaging involves exposing the subject to high-frequency sound waves (20 kHz- 200 MHz) to produce images from the echoes produced by reflections from boundaries between internal structures. When acoustic waves travel across an interface between materials with different acoustical impedance, part of the sound wave is reflected. This echo can be detected by a suitably positioned probe.

In US imaging (Figure 1.2), a hand-held probe is moved over the sample, using a water-based gel to ensure good acoustic coupling. The probe contains one or more acoustic transducers and sends pulses of acoustic energy into the patient. The time it takes for the echo to travel back to the probe is measured and used to calculate the depth of the tissue interface causing the echo. The greater the difference between acoustic impedances, the larger the echo is. So the transducer alternates between two

major functions: 1) producing ultrasound pulses and 2) receiving or detecting the returning echoes. Within the transducer are one or more piezoelectric elements. When an electrical pulse is applied to the piezoelectric element, it vibrates and produces the ultrasound wav. Conversely, when the piezoelectric element is vibrated by the returning echo pulse it produces a pulse of electricity. Finally, a computer is used to interpret these echo waveforms to construct an image (5). Hence an ultrasound image is a display showing the location of reflecting structures or echo sites within the body.

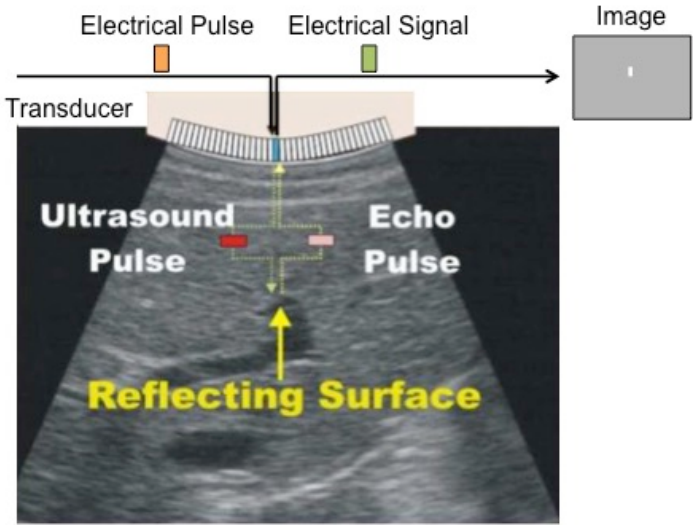

Figure 1.2: Functioning principle of ultrasound imaging. An electrical pulse is converted in an ultrasound pulse by the transducer. When a sound wave encounters a material with different acoustical impedance, part of the sound wave is reflected and detected by the probe as an echo, which is converted in electrical signal to form an image.

The axial resolution in US, which is the minimum separation between structures the ultrasound beam can distinguish parallel to its path (Figure 1.3 a), mainly depends on wavelength: the axial resolution will be higher at shorter wavelengths. The lateral resolution is the minimum separation between structures the ultrasound beam can distinguish in a plane perpendicular to its path (Figure 1.3 b). It depends on the depth of the imaged structures and the width of the beam: the thinner the beam, the higher the lateral resolution.

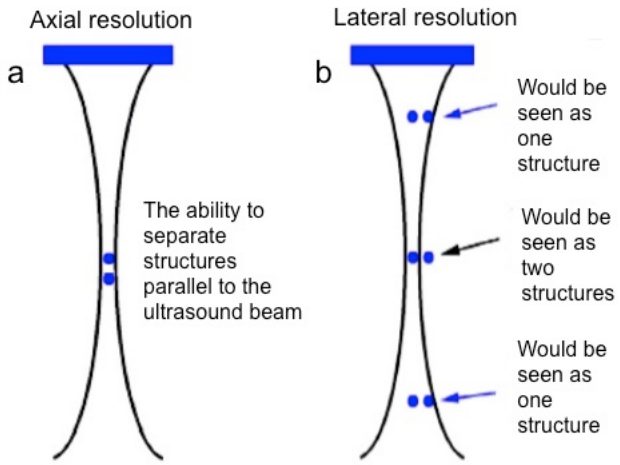

Figure 1.3: Axial and lateral resolution in ultrasound imaging. a) The axial resolution is the ability to separate structures parallel to the ultrasound beam. b) The lateral resolution is the ability to separate structures that are perpendicular to the path of the beam.

1.1.1.4 Magnetic resonance imaging

As shown schematically in Figure 1.4, in MRI/ μMRI samples are placed in a strong magnetic field (typically 1 to 3 T), which aligns the hydrogen nuclear spins in a direction parallel or antiparallel to the field. Nuclear spins precess around magnetic filed lines at the Larmor frequency, the magnitude of which depends on the magnetic field strength and the gyromagnetic ratio of the nucleus. A radio frequency (RF) pulse is applied to the sample at or around the Larmor frequency, in an orientation that causes the nuclear spins to be rotated into a plane orthogonal to the external field. This can then be detected as an induced voltage in an RF receiver (6). After the removal of the RF pulse, spins relax back towards alignment with the main magnetic field, with a time constant of T1 (the value of which is tissue-dependent). Signal strength also decreases in time due to loss of phase coherence of the spins, which occurs according to a time constant T2 (which is also tissue-dependent).

Magnetic field gradients are used to localize spins in space using phase and frequency-encoding, enabling an image to be formed via Fourier transform, and images can be weighted to enable contrast to be formed according to differences in T1, T2, proton density (in addition to several other parameters). μMRI, which aims to acquire magnetic resonance images at high resolution, has advanced to the point at which individual cells, and their organelles, can be imaged with spatial resolution of

<4 μm through the use of very high field strengths and innovative RF coil technology.

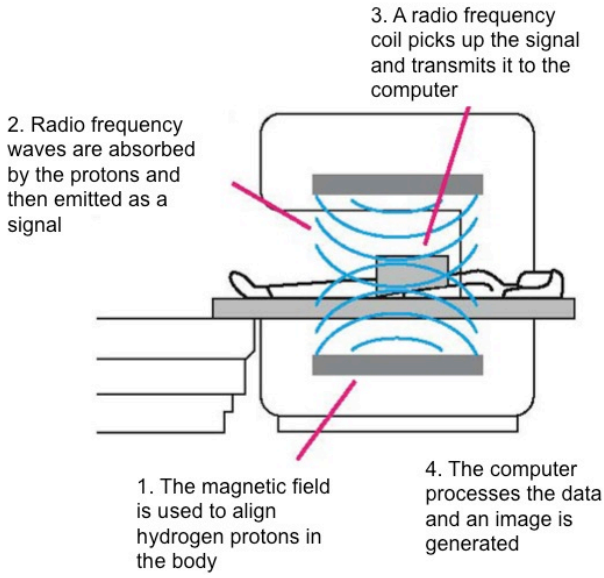

Figure 1.4: Functioning principle of MRI.

1.2 Aim of thesis

This thesis is focused around the use of new *ex vivo* optical imaging techniques, such as optical projection tomography, to acquire high resolution 3-images (~5 μm) of the internal structure of intact tumour samples over a large field of view.

Techniques like OPT require large specimens (~1 cm^3) to be rendered transparent via a process known as *optical clearing*, which was extensively used in this thesis and which can be achieved using a number of methods. The first objective of the thesis was to develop a spectroscopy-based method to quantify optical clearing efficacy of different approaches in order to quantitatively compare them.

The main aim of the thesis was to investigate in 3-D vascular networks of healthy tissues as well as tumours in order to ultimately study the effect of vascular disrupting agents on tumour vascular networks at different time points. After testing different approaches (vasculature perfusion with radiopaque polymer injection media versus fluorescently labelled proteins, μCT versus OPT), this was achieved with the

combination of OPT and fluorescent compounds that bind to the vascular endothelium.

The final objective of the thesis was to compare the ability of OPT and high resolution episcopic microscopy (HREM) to analyse tumour vasculature in a model of metastatic liver.

1.3 Introduction to optical imaging and historical background

For more than three centuries, optical microscopy has made a fundamental impact on biological discovery and biomedical research. The latest developments are moving the technology towards the ability to resolve structures at increasingly small length scales through techniques such as super resolution microscopy, but also across whole organs and organisms, in three dimensions. Such high-resolution 3-D imaging techniques have been spurred on by the increasing use of embryos and animal models of disease, in which a 3-D representation of tissues is crucial for understanding gene expression and complex dynamics in healthy and diseased organisms.

Microscopy has its origins in the simple magnifying glass, which was known as a "flea glass" due to its application to the study of fleas and other small insects. In 1590 Zaccharias and Hans Janssen made the first recognisable microscope, composed of 3 sliding tubes, measuring 18 inches long when fully extended, and two inches in diameter. The magnification of this instrument was 3X when fully closed and 9X when fully extended. No Janssen microscope has survived.

In 1609 Galileo Galilei made a microscope by converting one of his telescopes, and featured a diverging lens as an eyepiece and a converging lens as an objective. An early microscope made of two converging lenses was also presented around 1620 by the astronomer Cornelius Drebbel. Antony Van Leeuwenhoek in the late 17th century made his own simple microscope, which was hand-held, had a single lens and a magnification of 270X. This microscope lead to his discovery of red blood cells in 1673, as well as the discovery of bacteria and human sperm.

Magnification is often considered the key property of a microscope. However, to increase the magnification of a single-lens microscope, the focal length has to be reduced by reducing the lens diameter, and after a point, the lens becomes difficult to see through. To solve this problem, the compound microscope system was invented in the 17th century. This type of microscope incorporates more than one lens so that the image magnified by one lens can be further magnified by another. Nowadays the lens closer to the object to be viewed is refers to as "objective", while the lens closer to the eye is called "eyepiece".

All of the early microscopists saw quite distorted images due to the low quality of the glass and imperfect shape of their lenses. Little was done to improve the microscope until the middle of the 19th century, when companies like Leitz and Zeiss began producing precision optical instruments. In the first half of the 20th century fundamental principles were established for fluorescence microscopy and in 1957 Marvin Minsky applied for the first patent for confocal microscopy (7) (described in section 1.6.2).

1.4 Optical systems basic concepts

Several physical principles are key to the operation of a microscope, such as lens resolution and numerical aperture. These are discussed in this section.

1.4.1 Numerical aperture

The numerical aperture (NA) of a microscope objective lens (Figure 1.5) is a measure of its ability to gather light and resolve fine specimen detail at a fixed object distance. It is a measure of the acceptance angle and relates to the width of the cone of light, and it is defined by

$$NA = n\,sin\theta \qquad \text{Eq. 1.1}$$

Where n is the refractive index of the imaging medium between the front lens of the objective and the specimen cover glass (n is 1.00 for air, 1.33 for pure water, and typically 1.52 for immersion oil). θ is one-half the angular aperture (A) of the

objective. Because the aperture angle cannot exceed 90° and the refractive index is never less than 1, NA is always around 1 for air. When immersion oil is used (n > 1), the numerical aperture increases and, along with it, the resolution.

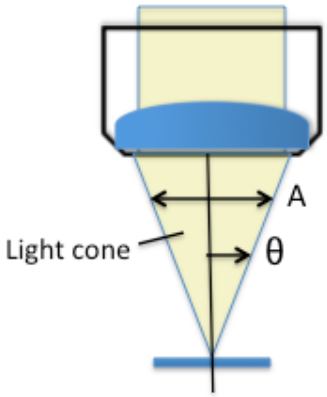

Figure 1.5: Numerical aperture of an objective lens. Image-forming light waves pass through the specimen and enter the objective in the shape of an inverted cone.

1.4.2 Lateral resolution

The lateral resolution of a microscope objective (R), also called spatial resolution or horizontal resolving power, is defined as the smallest distance between two points on a specimen that can still be distinguished as two separate entities. Resolution is a subjective value in microscopy as at high magnification an image may appear unsharp but still be resolved to the maximum ability of the objective. As shown in Eq. 1.2, the numerical aperture determines the resolving power of an objective: the higher the numerical aperture, the better the resolution. The wavelength spectrum of light used to image a specimen is also a determining factor in resolution: at shorter wavelengths details can be resolved to a greater degree than at longer wavelengths. The Abbe formula for the lateral resolution is

$$R = \frac{1.22\,\lambda}{2NA} \qquad \text{Eq. 1.2}$$

Where R is resolution (the smallest resolvable distance between two objects) and λ is the wavelength of light.

1.4.3 Depth of field

The depth of field (DOF) of a microscope, often referred to as axial or longitudinal resolving power, is determined by the distance from the nearest object plane in focus to that of the farthest plane also simultaneously in focus (Figure 1.6). In microscopy, the depth of field is very short and usually measured in units of microns.

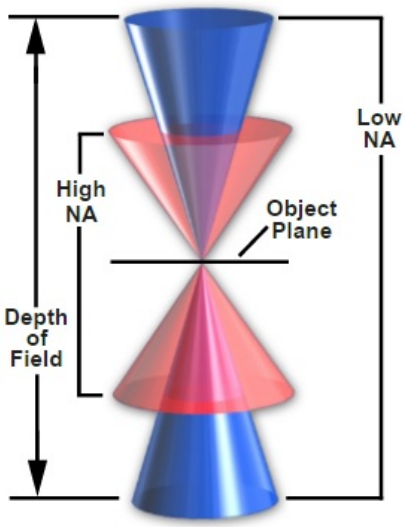

Figure 1.6: Diagram showing the relation of depth of field and numerical aperture.

The DOF can be improved by closing the aperture on the objective, yet at the expense of optical resolution and with a significant loss of light. The depth of field, d, is defined as

$$d = \frac{\lambda\sqrt{n^2-(NA)^2}}{(NA)^2} \qquad \text{Eq. 1.3}$$

1.5 Theoretical basis of fluorescence imaging

1.5.1 Fluorescence

Fluorescent molecules, also called fluorophores, are used in biological research to mark proteins, tissues, and cells for examination. These molecules absorb light of one wavelength and emit light of another wavelength, usually longer. The

mechanism of fluorescence is illustrated in the Jablonski energy diagram (Figure 1.7).

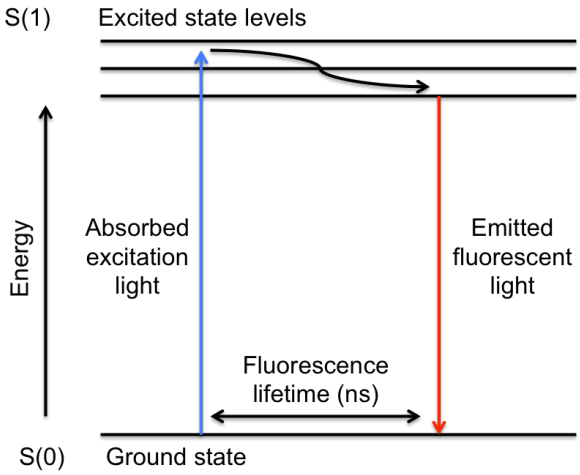

Figure 1.7: Jablonski energy diagram for fluorescence. Fluorescent light (red arrow) is emitted at higher wavelength than absorbed excitation light (blue arrow).

A photon of excitation light is absorbed by an electron of a fluorescent particle, which raises the energy level of the electron to an excited state. During this short excitation period (order of nanoseconds), some of the energy is dissipated by molecular collisions or transferred to a proximal molecule, and then the remaining energy is emitted as a photon as the electron relaxes back to the ground state.

The electronic state of a molecule determines the distribution of negative charge and the overall molecular geometry. For any particular molecule, several different electronic states exist (illustrated as S(0), S(1) in Figure 1.7), depending on the total electron energy and the symmetry of various electron spin states. Each electronic state is subdivided into a number of vibrational and rotational energy levels associated with the atomic nuclei and bonding orbitals. The ground state for most organic molecules is an electronic singlet in which all electrons are spin-paired (have opposite spins). At room temperature, very few molecules have enough internal energy to exist in any state other than the lowest vibrational level of the ground state, and thus, excitation processes usually originate from this energy level.

Because the emitted photon usually carries less energy and therefore has a longer wavelength than the excitation photon, the emitted fluorescence can be distinguished from the excitation light. The difference in energy between excitation and emission maxima (Figure 1.8) is called Stokes shift. The size of the shift varies with molecular structure, but can range from just a few nanometres to over several hundred nanometres. For example, the Stokes shift for fluorescein isothiocyanate (FITC) is approximately 20 nm, while the shift for quinine is 110 nm.

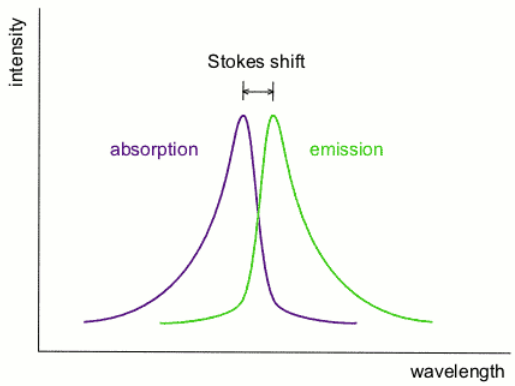

Figure 1.8: Stokes shift is the difference in wavelength between positions of the band maxima of the absorption and emission spectra of the same electronic transition.

Fluorophores can be repeatedly excited, until they are irreversibly damaged (photobleached). Because fluorophores can therefore emit numerous photons through this cycle of excitation and emission, fluorescent molecules are useful in a broad range of research applications. For example, FITC can undergo excitation and relaxation for approximately 30,000 cycles before the molecule no longer responds to incident illumination.

1.5.2 Fluorescence quenching

Fluorescence quenching refers to any process that decreases the intensity of emitted fluorescent light. The most common form of quenching in fluorescence is collisional quenching. This occurs when a certain molecule, or quencher, comes into contact with the fluorophore in its excited state. This collision results in a non-radiative decay back to the ground state of the fluorophore. This decrease in fluorescence due to collisional quenching is described by the Stern-Volmer equation:

$$\frac{F_0}{F} = 1 + k_q t_0 [Q] \qquad \text{Eq. 1.4}$$

where F is the measured fluorescence, F_0 is the initial, unquenched fluorescence, κ_q is the biomolecular quenching constant (s^{-1}), t_0 is the unquenched fluorescence lifetime (s), and [Q] is the quencher concentration. The biomolecular quenching constant (s^{-1}) can be calculated based on temperature and viscosity or experimentally determined. The usual lifetime of fluorescence (10^{-8} to 10^{-10} s) is ample time for quenchers to collide with excited state fluorophores and cause quenching. Many substances can behave as a quencher, but the most prominent in biological tissue is oxygen (8).

1.5.3 Photobleaching

Photobleaching is an irreversible photo-physical process that can occur during excitation, which leads to the destruction of the fluorophore through the modification of chemical bonds within the molecule. This occurs during the transition from the excited singlet ground state S(0) to the excited triplet state S(1), when fluorophores may interact with other molecules in the environment, such as oxygen. This oxidation of the fluorophore destroys its fluorescence. As mentioned in the previous section, fluorophores can undergo a series of excitation and emission cycles before photobleaching, and the number of cycles depends on the molecular structure of the fluorophore and the local environment. It can be minimized or avoided by exposing the fluorophore to the lowest possible level of excitation light intensity for the shortest length of time (which must be balanced against the need for sufficient signal detection).

Figure 1.9 shows an example of cell photobleaching. The HeLa cells shown in the image were labelled with FITC-conjugated phalloidin. Image 1.9 a shows the initial intensity of the FITC, and the degree of photobleaching after 36 seconds of constant illumination is showed in Image 1.9 b, in which the signal is markedly reduced.

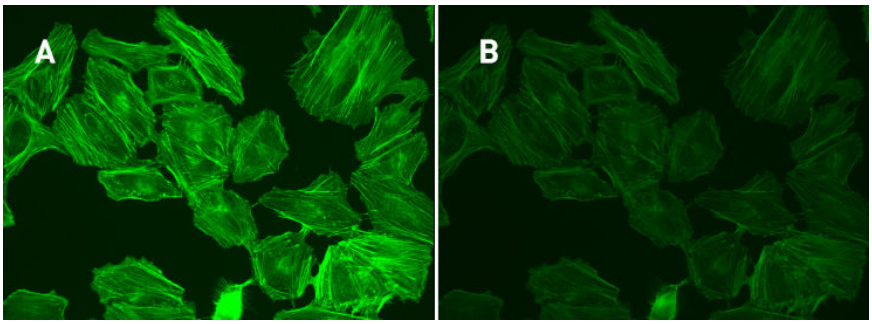

Figure 1.9: Example of photobleaching. HeLa cells were labelled with FITC-conjugated phalloidin. a) Initial intensity of the fluorophore. b) Photobleaching that occurs after 36 seconds of constant illumination. The figure was adapted from ref. (9)

1.5.4 Fluorophore brightness

The brightness of a given fluorophore is determined by the molar extinction coefficient and quantum yield, both of which are specific for each fluorophore. The molar extinction coefficient (ε) is defined as the quantity of light that can be absorbed by a fluorophore at a given wavelength and is measured in M^{-1} cm^{-1}:

$$\varepsilon = \frac{A}{lc} \qquad \text{Eq. 1.5}$$

where A is the absorbance of the sample, l is the length of the light path through the sample, and c is the concentration of the solution.

The quantum yield (Φ) is defined as number of photons that are emitted by the fluorophore divided by the number of photons that are absorbed:

$$\Phi = \frac{\#\ \text{photons emitted}}{\#\ \text{photons absorbed}} \qquad \text{Eq. 1.6}$$

This range from 0 to 1 and provides a measure of the efficiency of a fluorophore. The brightness of a fluorophore is then calculated as the product of ε and Φ.

1.5.5 Fluorescent probes

Fluorophores can generally be divided into three general groups: organic dyes, biological fluorophores and quantum dots. These are discussed in the following sections.

1.5.5.1 Organic dyes

Synthetic organic dyes, such as fluorescein, were the first fluorescent compounds to be used in biological research. Derivatives of these original compounds have been produced to improve their photostability and solubility. These dyes are also derivatized to use in bioconjugation, especially fluorescein isothiocyanate (FITC), rhodamine (tetramethyl rhodamine isothiocyanate, TRITC) and commercial variants with greater performance. The small size of these fluorophores allows crosslinking with macromolecules, such as antibodies, without interfering with proper biological function. Organic dyes are the fluorescent compounds mainly used in this thesis.

1.5.5.2 Biological fluorophores

The first use of a biological fluorophore for research applications occurred in the 1990s, when the green fluorescent protein (GFP) was cloned from the jellyfish *Aequorea victoria* and used as a gene expression reporter (10). Since that time, derivatives of the original GFP and many other proteins have been designed for use in biological expression systems, and their use is now commonplace in biological research.

The benefit of these types of fluorophores is that expression plasmids can be introduced into either bacteria, cells, organs or whole organisms, to drive expression of that fluorophore either alone or fused to a protein of interest in the context of the biological processes studied. The use of fluorescent proteins can be time-consuming, and expressing large amounts of light-producing proteins can cause reactive oxygen species through photobleaching and induce artifactual responses or toxicity. Additionally, the size of the fluorescent protein can change the normal biological function of the cellular protein to which the fluorophore is fused, and biological fluorophores do not typically provide the level of photostability and sensitivity offered by synthetic fluorescent dyes.

1.5.5.3 Quantum dots

Quantum dots are nanocrystals with unique chemical properties that provide tight control over the spectral characteristics of the fluorophore. Quantum dots were developed in the 1980s and since the 1990s have been increasingly used in fluorescence applications in biological research. They are nanoscale-sized (2-50 nm) semiconductors that, when excited, emit fluorescence at a wavelength based on the size of the particle; smaller quantum dots emit higher energy than large quantum dots, and therefore the emitted light shifts from blue to red as the size of the nanocrystal increases. Because quantum dot size can be tightly controlled, there is greater specificity for distinct excitation and emission wavelengths than other fluorophores.

Quantum dots have also been reported to be more photostable than other fluorophores, as one report showed that quantum dots remained fluorescent for 4 months in an *in vivo* imaging study (11). Additionally, quantum dots can be coated for use in different biological applications such as protein labelling. While the use of quantum dots in biological applications is increasing, there are reports of cell toxicity (of cadmium, for example, (12)) in response to the breakdown of the particles, and their use can be cost-prohibitive (13, 14).

1.5.6 Autofluorescence

Autofluorescence can be either “natural” or “fixative-induced” fluorescence. It is caused by molecules within the tissue that are either inherently fluorescent or are made fluorescent by tissue processing (15). Natural fluorescence is mainly due to the presence of endogenous flavins, coenzymatic oxidation reduction carriers involved in the metabolism of most organisms (16). Other common species include nicotinamide adenine dinucleotide (NADH) and its derivatives, which are crucial to many biochemical reactions in most types of cells (17). Another cause of autofluorescence are lipofuscins, substances found to positively stain for lipids, carbohydrates and proteins (18). Natural fluorescence is also due to the presence of reticulin fibres, collagen and elastin in tissues (19). Autofluorescence can also be caused by fixatives: aldehyde fixatives react with amines and proteins to generate fluorescent products.

Despite being used for the creation of images of internal structures of organs and organisms or to discriminate between different kind of tissues without the use of exogenous fluorophores or dyes (20), the presence of autofluorescence often leads to low signal-to-noise ratios and loss of contrast and clarity in fluorescence microscope images (21, 22). This is a challenge that can be addressed both with chemical treatments or optical approaches, which include the optimization of the optical filters used for fluorescence excitation and emission. However, this is not always easy as the emission spectra of natural fluorescence and fixation-induced fluorescence are very broad compared to the spectra of the dyes, probes and proteins used for labelling specific structures in tissues. Autofluorescence makes it difficult to separate wanted from unwanted fluorescence by optimization of the optical filters used for fluorescence excitation and emission (as discussed in Chapter 3).

The simplest way to inhibit aldehyde-induced fluorescence is to use a fixative that does not contain an aldehyde, or to use low concentrations of aldehyde. Fluorescence from fixatives can also be reduced (quenched) chemically, for example with sodium borohydride (23, 24).

1.6 Modern developments in optical imaging

An important step in the development of fluorescence microscopy was the discovery of the GFP, which is derived from the jellyfish *aequorea victoria* and was described for the first time in 1961 by Osamu Shimomura (25). In the 1990s Douglas Prasher and Martin Chalfie worked on the sequencing and cloning of GFP and managed to express it in the bacterium *Escherichia coli* for the first time so that it could be used as a tracer molecule for other proteins (10, 26), that is it could be attached to genes of interest in bacteria, cell culture, animals or plants with the aim of analysing them. Using GFP and its mutated derivatives, many fluorescence techniques were developed and improved in the following years that still play an important role in modern microscopy.

One of these is förster (or fluorescence) resonance energy transfer (FRET). The mechanism of FRET involves a donor fluorophore in an excited electronic state,

which may transfer its excitation energy to a nearby acceptor non-radiatively through long-range dipole-dipole interactions. FRET occurs between two fluorophores only when the distance separating them is 3 to 8 nanometres or less (27). Over the last few decades the development of intensity-based imaging techniques applying the method of FRET microscopy (wide field, confocal, and 2P microscopy) facilitated the study of interactions between proteins inside intact living cells (28). This is crucial in the investigation of cellular events such as signal transduction and gene transcription, which require the assembly of proteins into specific macromolecular complexes (29).

1.6.1 Wide-field fluorescence microscopy

In wide-field microscopy (Figure 1.10), which is generally used for looking at cells or tissue sections, the entire field is simultaneously illuminated throughout its full width and depth. In a typical wide-field fluorescence microscopy setup three filters are used: an excitation filter, an emission filter and a dichroic filter. Excitation light, usually provided by a mercury lamp, is filtered (by the excitation filter) and directed to the sample via a dichroic mirror, which is specifically designed to reflect the excitation wavelengths and transmit the emission light. Dichroic mirrors are generally made by alternating layers of optical coatings with different refractive indices built on a glass substrate. The interfaces between the layers of different refractive index produce phased reflections, selectively reinforcing certain wavelengths of light and interfering with other wavelengths. The passband of the filter is tuned by changing the thickness and number of the layers.

After being directed by the dichroic mirror, the light emitted by the fluorophore, characterized by a different range of wavelengths, is filtered through the emission filter, which transmits only the emission wavelengths and detected by a camera. Thus in wide-field fluorescence microscopy the entire sample is illuminated at all times during image acquisition, and both illumination and detection of light covering the whole visual field of the chosen microscope objective is achieved simultaneously. Hence the images consist of both in-focus light at the focal plane of the lens and out-of-focus light coming from other focal planes in the image.

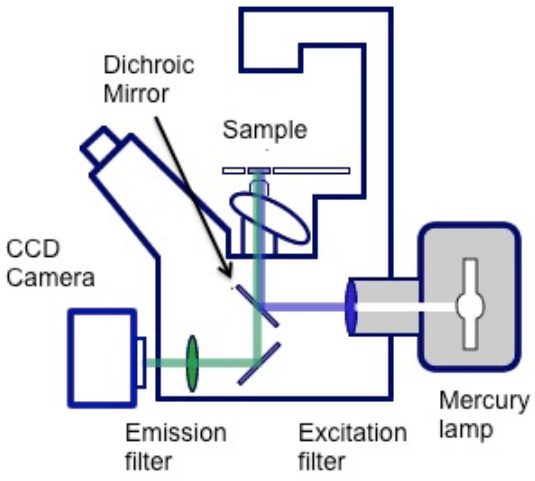

Figure 1.10: Schematic of wide-field microscopy. The excitation light (blue line) coming from a mercury lamp is filtered and directed to the sample through a dichroic mirror. Fluorescent light coming from the sample (green line) is detected by a CCD camera.

Compared to other imaging techniques such as electron microscopy (EM), conventional fluorescence microscopy is limited by the diffraction of light. This diffraction limit, about 200–300 nm in the lateral direction (perpendicular to the axis of the light beam) and 500–700 nm in the axial direction (along the axis of the light beam), is comparable to or larger than many subcellular structures, leaving them too small to be observed in detail.

1.6.2 Confocal and multiphoton microscopy

Confocal microscopy was first developed by Minsky in 1955 (7). In the late 1980s, with the advent of lasers, confocal microscopy became more widespread and known as confocal laser scanning microscopy (CLSM). CSLM has been used extensively for imaging of fluorescent proteins or dyes to investigate structure and function of a wide spectrum of tissues and cells. Figure 1.11 shows the operational principle of a confocal microscope, in which out-of-focus light is removed by inserting a pinhole at the image plane such that out-of-focus light does not reach the detector. Only light focussed at the pinhole passes through it, and all other light is scattered. However, the generation of a focussed spot of illumination through the use of spatial filtering only provides information of a single point at one time. To create an image, the focussed spot of light has to be scanned across the specimen. In the system

developed by Minsky, as well as in later generations of confocal microscopes, this was achieved by moving the stage under the illumination source. This solution became impractical due to the mass of the stage, which made scanning times extremely slow, and White, Amos and Fordham developed a new configuration, where the light beam was scanned over the specimen rather than moving the microscope stage (30). The principle was to scan and collect light using two oscillating mirrors mounted on galvanometers. One mirror, the fast (line) scanning mirror, scanned in the x-axis, and the other (frame) mirror scanned more slowly in the y-axis. By coordinating the two scan axes, it was possible to build a complete image.

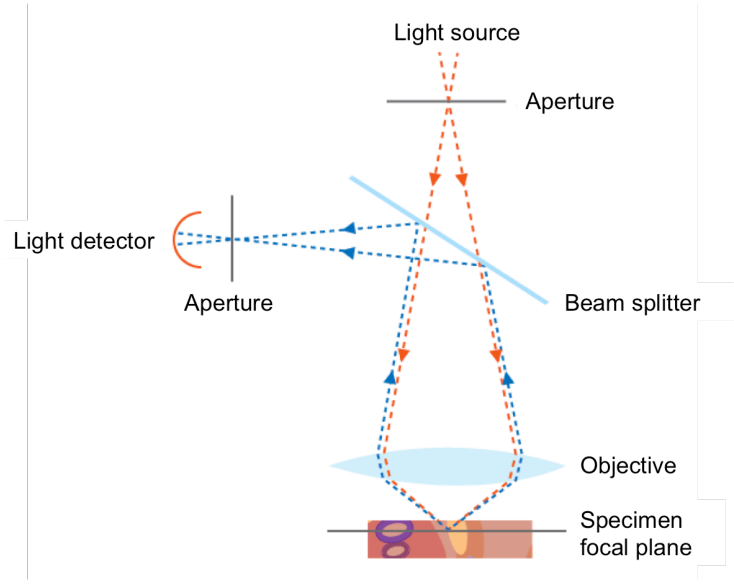

Figure 1.11: Operational principle of confocal microscopy: a confocal microscope uses point illumination and a pinhole in an optically conjugate plane in front of the detector to eliminate out-of-focus light. As only light produced by fluorescence very close to the focal plane can be detected, the image resolution, particularly in the sample depth direction, is much better than that of wide-field microscopes. However as much of the light from sample fluorescence is blocked at the pinhole this increased resolution is at the cost of decreased signal intensity so long exposures are often required.

In 1997 CLSM underwent significant modifications by the implementation of two-photon (2P) excitation, a technique introduced by Göppert-Mayer in 1931 (31). In 2P microscopy the fluorophore is excited by two photons, each of which carries half of the energy necessary to excite the molecule of interest. As the probability of the near-simultaneous absorption of two photons is extremely low, a high flux of

excitation photons is required. Whereas 2P microscopy uses laser-scanning principles like CLSM, in 2P microscopy, focussed femtosecond laser pulses are used for illumination and scanned through the tissue. These pulses are concentrated in a confined area within the tissue, hence the fluorescent signal comes from a restricted volume. The narrow localization of two-photon excitation to the illumination focal point is the basis for the main advantages of 2P over confocal microscopy. In a confocal microscope, although fluorescence is excited throughout the specimen illuminated volume, only signals originating in the focal plane pass through the confocal pinhole, allowing background-free data to be collected. In contrast, two-photon excitation only generates fluorescence at the focal plane, and since no background fluorescence is produced, a pinhole is not required. Because in 2P there is no absorption in out-of-focus specimen areas, more of the excitation light penetrates through the specimen to the plane of focus. The result is greatly increased specimen penetration, which is generally two or three times greater than is possible with confocal microscopy. Another benefit of utilization of two-photon excitation is the minimization of photobleaching, one of the most severe limitations in fluorescence microscopy (discussed in section 1.5.3).

Whereas because of the use of near infrared (NIR) light multiphoton microscopy can achieve higher penetration depth (2-3 times higher) of confocal microscopy (which does not go beyond 1 mm), the resolution of 2P microscopy is generally worse than that of confocal since the diffraction-limitation of focal spots increases with higher wavelengths (32). Confocal and 2P microscopy have revolutionized biological discovery by allowing non-invasive study of life processes in unperturbed environments. Indeed, one of the main advantages of CLSM and 2P microscopy is their ability to create 3-D images without the need to physically slice the sample (32, 33).

1.6.3 Super-resolution microscopy

Optical imaging has recently moved towards greater resolution with super-resolution microscopy, which was first developed in the 1990s by Stefan Hell. Using techniques such as stimulated emission depletion (STED) and photoactivated localization microscopy (PALM) it is now possible to achieve a spatial resolution of ~8-25 nm

(34) thereby allowing subcellular structures to be resolved that are not visible with conventional light microscopy (35, 36). Stefan Hell was awarded the Nobel Prize 2014 in Chemistry together with Eric Betzig and William Moerner for the development of super-resolved fluorescence microscopy (37).

1.6.4 Photoacustic imaging

Photoacustic (PA) is a non-invasive imaging technique that relies upon the generation of ultrasounds through the absorption of low-energy nanoseconds laser pulses by tissue chromophores, such as melanin and haemoglobin (38). The ultrasound waves are generated by the temporal thermoelastic expansion of light absorbing structures, following transient local temperature rise, and are detected on the tissue surface using ultrasound receivers (Figure 1.12).

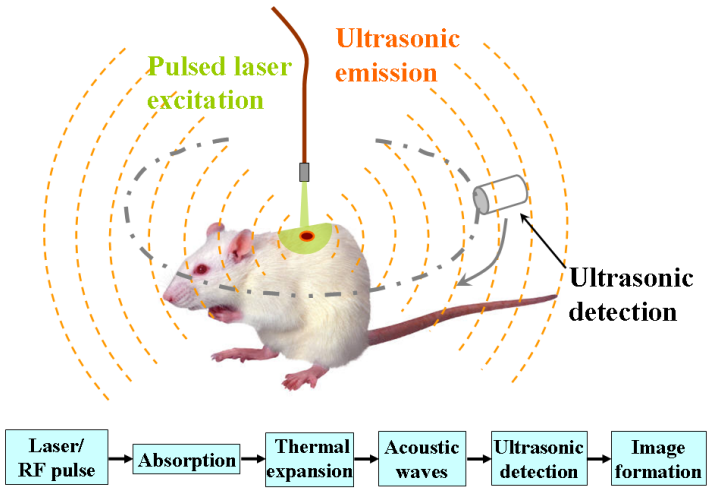

Figure 1.12: Functioning principle of Photoacustic Imaging. Non-ionizing laser pulses are delivered into biological tissues. The delivered energy is absorbed within the tissue and converted into heat, leading to transient thermoelastic expansion and thus ultrasonic emission. The generated ultrasonic waves are detected by ultrasonic transducers and then analysed to produce images.

The main advantage of PA relies in the optical contrast, as scattering of ultrasound in biological tissues is two to three orders of magnitude weaker than optical scattering (39). This allows much greater penetration depths (a few centimetres) compared to purely optical imaging techniques based on the emission and absorption of photons (40). Due to the strong absorption of haemoglobin at visible and near infrared

wavelengths, PA imaging is able to visualize vascular structures without the need for contrast agents.

1.7 Challenges and approaches to imaging thick tissues with visible light

One challenge of biological research is to study the structure of cells and their interactions deep in tissue, in 3-D and at high resolution. At the beginning of this century electron microscopy emerged as a way to investigate the ultrastructures of several specimens (41). Despite its revolutionary imaging principle, electron microscopy was limited to the study of 60-90 nm thick slices. Standard fluorescence microscopy techniques such as confocal microscopy and 2P microscopy have since increased the imaging depth to hundreds of micrometres. These techniques are used to image fluorescently labelled small samples (<mm scale) (42), but are not suitable for 3-D high-resolution imaging of larger samples ('mesoscopic', ~0.5 - 10 mm scale). One of the main reasons is that these imaging systems can only image a relatively small field of view due to limitations in their optics. Also, they use visible light to obtain detailed images of organs and tissues, as well as smaller structures including cells. Light travelling through the sample is absorbed (e.g. by blood, lipids, melanin) and scattered at the interface of media with different refractive indices, resulting in low contrast and spatial resolution with increasing penetration within the sample (43-45) providing a fundamental limitation to the depth penetration of most optical imaging techniques.

Imaging techniques such as optical projection tomography and light sheet fluorescence microscopy, discussed in sections 1.10.1 and 1.10.2, allow the fast acquisition of images of whole organs or organisms without the need to physically section them. This not only speeds up the imaging process, but also allows the study of the interaction between different structural components within tissues. However, with these techniques thick biological tissues (>100 nm) have to be made transparent through a process called *optical clearing* in order to be imaged without previous sectioning. This is a process that aims at rendering the biological tissue optically transparent. A few optical clearing methods are examined in detail in section 1.9.

Moreover, strategies such as imaging in the NIR window, with emission wavelengths between 700 and 1300 nm, have been developed to image deep in tissues. At these wavelengths, absorption of light by haemoglobin, lipids, and water is lowest (Figure 1.14), hence light penetration in tissue is maximized. Also, the natural fluorescence of tissues, referred to as autofluorescence and discussed in section 1.5.6, is greatly reduced (46). In the next section the behaviour of light travelling through biological tissues will be analysed.

1.8 Optical properties of tissues

The optical properties of tissues are mainly described in terms of:

- Attenuation (absorption and scattering)
- Refractive index

These parameters, which are described below, are dependent on the wavelength of the light used for imaging.

1.8.1 Attenuation

A beam of light passing through matter is attenuated: its intensity decreases as the light penetrates farther into the medium and its velocity will be less in the medium than in free space. Attenuation is the term used to describe the loss of light due to both *scattering* and *absorption* effects. Light attenuation is a phenomenon that interests and limits both the excitation light entering a tissue and the fluorescent light emitted by the tissue. If absorption and scatter occur and both contribute to attenuation, a total (linear) attenuation coefficient μ_t is defined:

$$I = I_0 e^{-\mu_T x} \qquad \text{Eq. 1.7}$$

where I is the transmitted light intensity, I_0 is the incident light intensity, and x is thickness of the material crossed by light.

The total attenuation coefficient can be expressed as:

$$\mu_t = \mu_a + \mu_s \qquad \text{Eq. 1.8}$$

where μ_a is the absorption coefficient (mm^{-1}), and μ_s it the scattering coefficient (mm^{-1}).

1.8.1.1 Absorption

For a non-scattering medium illuminated with a collimated beam of light of intensity I_0 and wavelength λ, the intensity of the emerging light will be:

$$I = Ie^{-\mu_a(\lambda)x} \qquad \text{Eq. 1.9}$$

where μ_a is the absorption coefficient of the medium and x is the width of the sample.

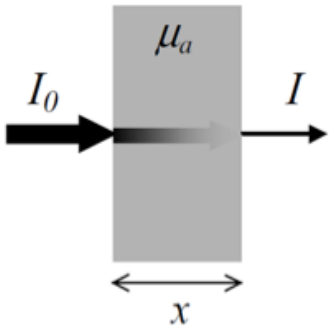

Figure 1.13: Attenuation of light through a non-scattering medium.

The absorption coefficient represents the probability per unit length of a photon being absorbed. The μ_a of a medium may be due to a number of absorbing substances, named chromophores, mixed together. The individual extinction coefficients of each chromophore represent their absorption at a particular concentration. The absorption coefficient of a mixture of chromophores can be expressed as the sum of the products of the concentration of each chromophore c_n with its extinction coefficient ε_n:

$$\mu_a(\lambda) = \sum_n \varepsilon_n(\lambda) c_n \qquad \text{Eq. 1.10}$$

The main absorbers in the body are haemoglobin, melanin, lipids and myoglobin (Figure 1.14). Haemoglobin, contained in red blood cells, is the molecule that carries oxygen from the respiratory organs to the rest of the body. It can be washed out by

perfusing the animal with a clear saline solution that replaces the blood in the whole circulatory system. Melanin, mainly present in skin, hair and the iris of the eye, can be avoided in albino mutant animals. Lipids, that can comprise 10 – 40 % of tissue, are present in subcutaneous tissues and particularly in the brain, mainly in the form of myelin. As it will be explained in detail later in this chapter, lipids can be eliminated and replaced with hydrogels to maintain the tissue structure. Myoglobin, the absorbing pigment in skeletal muscle, can be decoloured by perfusion, and further bleached with hydrogen peroxide. However, this approach can damage the tissue structure and affect fluorescent protein emission (47).

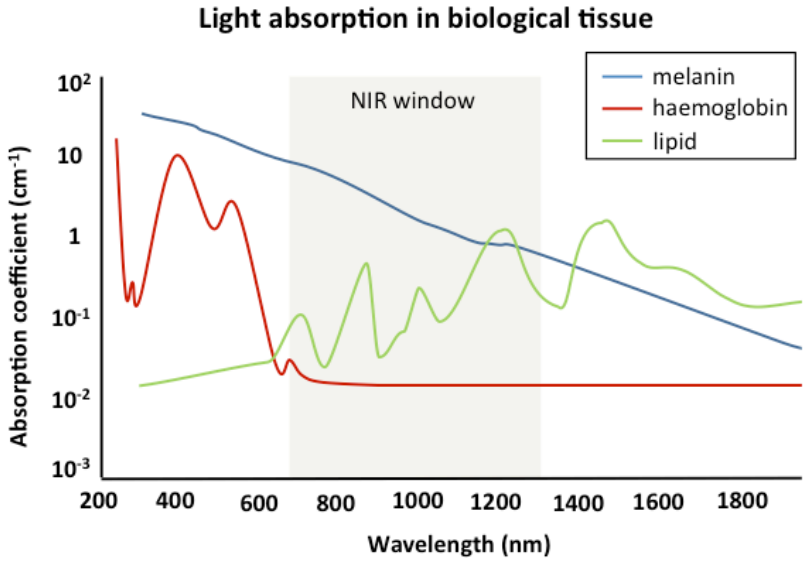

Figure 1.14: Absorption in tissue relative to some tissue chromophores: melanin (blue), haemoglobin (red), lipid (green). Haemoglobin demonstrates major absorption peaks in the UV and in the visible region, around 400 and 550 nm. Melanin is a highly effective attenuator, especially in the UV region. Melanin granules (diameter ≈ 1μm) are arranged in a periodic structure producing highly effective light scattering. This means that light is distributed throughout the cell avoiding local regions of high absorption and potential for cell damage. The absorption spectrum of lipids is relatively flat with some broad resonances in the NIR region (650 – 1300 nm).

1.8.1.2 Scattering

The scattering properties of a medium are described by its scattering coefficient μ_s, which is the product of the number density of scattering particles and the scattering cross section of the particles. Therefore μ_s represents the probability per unit length of a photon being scattered. Compared to the non-scattering case above, if a medium

is scattering the paths taken by the photons traversing it are no longer direct (Figure 1.15). This has two effects: not all the emerging photons can be detected unless the detector can collect over all angles and at all points on the surface of the medium, and the photons will have travelled varying distances through the scattering media.

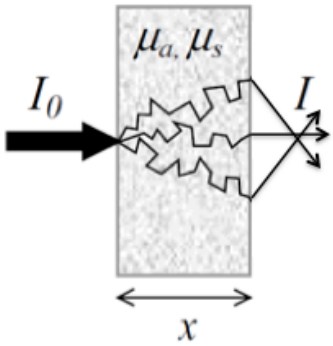

Figure 1.15: Attenuation of light through a scattering medium.

Light scattering can be quantified using the mean free path (MFP) of a photon. The MFP describes the average distance travelled by a photon between successive scattering events. Scattering depends on both the wavelength of light and the composition of the tissue; it is shorter in highly scattering tissues, such as unprocessed organs, and longer in low scattering tissues such as embryos or optically cleared organs. The MFP is defined as:

$$MFP = \frac{1}{\mu_t} \qquad \text{Eq. 1.11}$$

As in most of the biological tissue scattering is dominant over absorption ($\mu_s >> \mu_a$), the MFP can be approximated as:

$$MFP = \frac{1}{\mu_s} \qquad \text{Eq. 1.12}$$

While the MFP describes two scattering events, the transport mean free path (TMFP) denotes the total scattering, taking into account the MFP and the average angle by which photons are scattered in each collision (48).

Assuming again that $\mu_s >> \mu_a$, the TMFP can be defined as:

$$TMFP = \frac{1}{\mu'_s} \quad \text{Eq. 1.13}$$

where μ'_s is the reduced scattering coefficient and is expressed as

$$\mu'_s = \mu_s (1-g) \quad \text{Eq. 1.14}$$

where *g* defines the degree of forward scattering and in tissue is generally 0.8 to 1.

Hence,

$$MFP = TMFP (1-g) \quad \text{Eq. 1.15}$$

Therefore, the higher the value of *g*, the more forward the scattering. This results in light becoming diffused at longer distances, therefore producing higher penetration into tissue (43, 49). On average, biological tissue has an MFP of approximately 100 μm and the TMFP is around 1 mm. Table 1.1 shows the absorption coefficients and the TMFP for some biological tissues relative to the NIR spectral region.

Table 1.1: Typical optical properties of several tissues

Tissue type	μ_a(mm^{-1})	μ'_s (mm^{-1})	TMFP (mm)
Muscle (exsanguinated abdominal)	0.03 at 800nm	0.7 at 800nm	1.1
Brain (white matter)	0.0373 at 800nm	0.659 at 800nm	0.6
Brain (grey matter)	0.0460 at 800nm	0.529 at 800nm	-
Breast (glandular)	0.05 at 700nm	1.4 at 700nm	0.8
Breast (adipose)	0.07 at 700nm	0.9 at 700nm	0.3
Skin (dermis)	0.013 at 800nm	2 at 800nm	-

Table 1.1: Absorption coefficient, reduced scattering coefficient and transport mean free path for example biological tissues. Data has been collected from ref. (50-52)

1.8.2 Refractive index

The refractive index describes the effect that a medium has on the speed of light travelling through it. This speed changes when light passes between media of different refractive indices, causing its direction to change.

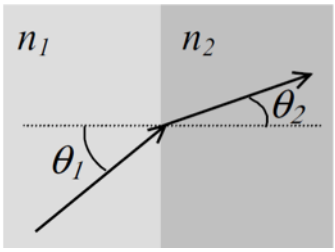

Figure 1.16: Refraction at the interface between two materials with different refractive indices.

Snell's law states that

$$n_1 sin\theta_1 = n_2 sin\theta_2 \qquad \text{Eq. 1.16}$$

where n is the refractive index of the medium, and θ is the angle between the propagation direction and the normal to the interface.
The speed of light in a medium (c) is given by

$$c = \frac{c_{vacuum}}{n} \qquad \text{Eq. 1.17}$$

1.9 Tissue optical clearing

Several optical clearing methods have been developed in order to reduce visible light opacity keeping the tissue structure intact. They generally aim at matching the refractive indices of scatterers like collagen, cell and cell membrane, melanin granules and the ground material (53) in order to increase the number of photons emitted from tissue depth.

1.9.1 Recent developments in tissue optical clearing

The optical clearing approaches can be divided in two main groups: (1) those that use sample dehydration as a first step and solvents for clearing and (2) newly developed aqueous-based techniques (Table 1.2).

Table 1.2: Comparison of optical clearing techniques

Name	Final n	Key components	Time	Alteration	Lipid preserved	Perfusion	Toxic	Reference
Spatleholz	1.55	BB/MetSal	months	shrinkage	no	no	yes	Spatleholz 1914
BABB	1.55	BA/BB	days	shrinkage	no	no	yes	Dodt 2007
3DISCO	1.56	DCM/DBE	hours/days	shrinkage	no	no	no	Ertuk 2012
iDISCO	1.56	DCM/DBE	hours/days	shrinkage	no	no	no	Renier 2014
Sucrose	1.44	Sucrose	1 day	no	no	no	no	Tsai 2009
FocusClear	1.47	Diatrizoic acid	hours/days	no	yes	no	no	Chiang 2009
ClearT	1.44	Formamide	hours/days	no	yes	no	no	Kuwajiima 2013
SeeDB	1.48	Fructose/urea thioglycerol	days	no	yes	no	no	Ke 2013
ScaleA2	1.38	Urea/ glycerol	weeks	expansion	no	no	no	Hama 2011
CUBIC	R1: 1.38 R2: 1.48	Urea/ glycerol	days	expansion	yes	no	no	Susaki 2014
CLARITY	1.45	FocusClear/ glycerol	days	expansion	yes	yes	no	Chung 2013
PACT	1.38-1.48	Histodenz	days/weeks	expansion	yes	no	no	Yang 2014
PARS	1.38-1.48	Histodenz	days/weeks	no	yes	yes	yes	Yang 2014

Table 1.2: Different approaches for optical clearing are compared. Blue: solvent based. Pink: simple immersion. Green: hyperhydration. Yellow: hydrogel embedding.
Final n: final refractive index. For CUBIC, both the refractive indices of reagent 1 (R1) and reagent 2(R2) are provided. Time: Time necessary for tissue clearing. Alteration: alteration in tissue morphology. Perfusion: perfusion of clearing agent.
Acronyms: BA: Benzyl alcohol, BB: Benzyl benzoate, MetSal: methyl salicylate, DCM: Dichloromethane, DBE: dibenzylether.
For all the mentioned techniques, independently on the type of clearing approach, the time taken to clear a sample depends on the actual size of the sample itself. The table has been adapted from ref. (54).

The first clearing agent was developed by Spalteholz back in 1914 and it consists of a mixture of benzyl alcohol and methyl salicylate (55). Generally, the process of traditional optical clearing is composed of three main steps: perfusion-fixation of the animal, dehydration of the excised organ and optical clearing. Fixation is achieved with paraformaldehyde (PFA). The dehydration step is crucial since the water has a very low refractive index (n~1.33) when compared to the cell membrane (n~1.45) (54, 56). Therefore the aim is to replace interstitial and intracellular fluids, mainly composed of water, with solutions that have a refractive index closer to the one of

the cell membrane. Common dehydrating agents are chemicals miscible with water such as ethanol, methanol and tetrahydrofuran (THF) (57). The sample is usually dehydrated through a graded series of solutions to minimize the shrinkage due to the removal of water. The refractive index of dehydrated protein (n>1.5) is higher than that of water or lipid. Hence the dehydration step has to be followed by another step, which aims to solvate lipid and matches the refractive index of the dehydrated tissue. This is the actual optical clearing step. The ideal organic solvent has to have a high lipid-solvating capacity and a high refractive index (n=1.5)(54). Several solutions have to date been used as optical clearing agents (OCAs): glucose (53), glycerol (58), a mixture of benzyl alcohol and benzyl benzoate (BABB or Murray's clear), dibenzyl ether (DBE) (59). Some solutions are preferred since they achieve a better degree of clearing, but some others have been shown to quench fluorescence to a smaller degree. Solvents like dimethyl sulfoxide (DMSO) (60) and thiazone (61) can additionally be used as penetration enhancers to increase penetration of OCAs. In fact the permeability rate of DMSO is ten times greater than that of water (62).

Although THF has proved to preserve the fluorescent signal better than other alcohols used for dehydration (53), its degree of fluorescence quenching is still high when used both in combination with BABB and with DBE (56). Whilst many clearing techniques have been developed strictly focusing on the brain, 3DISCO has a wider application spectrum. The main drawbacks of solvent-based techniques are the substantial tissue morphological changes (mainly shrinkage) due to the dehydration step, their toxicity and the quenching of fluorescent signal. Indeed, by removing water the dehydration step removes those molecules that are necessary to maintain fluorescent protein emission. This is the main reason that led a discrete number of scientists to look for a clearing approach based on aqueous solutions. These newly developed techniques can be classified by their approach that can be: (A) passive immersion in a clearing agent that matches the refractive index of the tissue, (B) lipid removal and hydration to lower further the refractive index of the tissue, (C) lipid removal and immersion in a refractive index matched solution.

Clear^{T}, a simple immersion method that uses formamide as clearing agent, is mainly used for embryos and neonatal mouse organs (Figure 1.17). Although it is

compatible with lipophilic dye tracing, it cannot be used with fluorescent proteins (63).

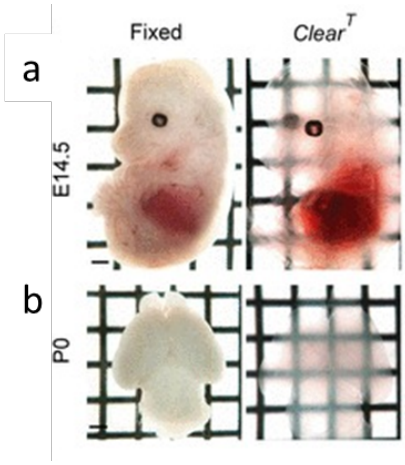

Figure 1.17: ClearT technique for optical clearing. The images on the left show the samples before clearing, while the processed cleared specimens are depicted on the right side. (a) An E 14.5 embryo and (b) a neonatal P0 mouse brain. The image was adapted from ref. (63).

Another clearing approach is based on the dissociation of collagen fibres. Indeed, collagen fibres are the major scatterers in tissues. Yeh et al. observed the dissociation of collagen structures immersed in glycerol, and recovery of the fibrous structure after removal of glycerol and subsequent application of phosphate buffered saline (PBS)(64).

Several water-based OCAs have been developed to image the mouse brain. Ke et al. have recently published the See Deep Brain method (SeeDB), based on fructose clearing (65). They found that the advantages of fructose are its high refractive index (n~1.5 at 25 °C) and also the fact that it does not change the size of samples. However, as it can be noticed in figure 1.18, SeeDB is limited to small samples such as mouse embryos or neonatal brains. Indeed, bigger samples such as a half mouse brain require high temperatures for clearing, up to 37 °C, that generally cause fluorescence loss.

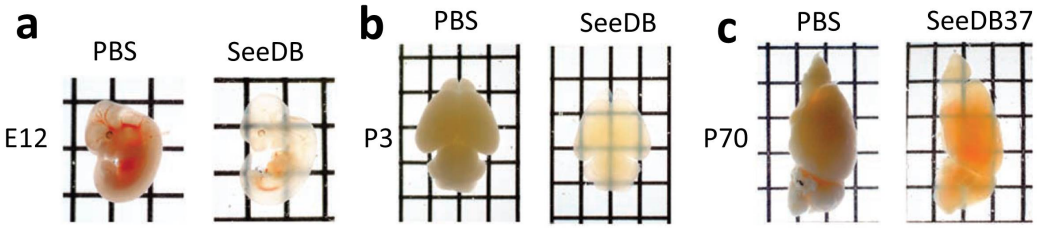

Figure 1.18: SeeDB approach for optical clearing. The images on the left show the samples in PBS, before clearing, while the processed cleared specimens are depicted on the right side. (a) An E12 Embryo and (b) a neonatal P3 brain cleared with SeeDB. (c) Adult hemi-brain (P70) cleared with SeeDB37, a modification of the SeeDB technique where the sample is incubated at 37 °C for clearing. The image is adapted from ref. (65).

Sca*l*e (Figure 1.19) is one of the recently developed techniques based on hyperhydration. The clearing agent used is mainly composed of urea and glycerol (66). The authors have shown that the fluorescence of fluorophores like EGFP and YFP is quenched less than in those samples cleared with ethanol and BABB. Olympus has manufactured a Sca*l*e friendly objective for confocal microscopy with long working distance and high NA to allow both high penetration and resolution. Although the majority of these techniques managed to achieve a high degree of transparency, none of them worked on enhancing the antibody and labels penetration which remains limited despite the higher light penetration in optically cleared samples (67).

Figure 1.19: Scale optical clearing technique. The photo shows two mouse embryos (E 13.5): a fixed embryo on the left hand side and an optically cleared embryo on the right. The image has been adapted from ref. (67).

Lipids are the main scatterers in the brain (50), hence the newer clearing techniques aim at their removal. In 2013 Deisseroth and his group have developed CLARITY to optically clear the whole mouse brain (68, 69). This technique, depicted in figure 1.20, is based on the removal of lipid bilayers with a mixture of boric acid and sodium dodecyl sulphate (SDS). Indeed, lipid barriers make the tissue poorly permeable to both clearing solutions and macromolecular antibodies, hence it is substituted by a cocktail of hydrogel monomers composed of acrylamide, bis-acrylamide, VA-044 initiator and PFA to keep the brain structure intact. The brain is then cleared. Lipids diffusion can be achieved with electrophoretic tissue clearing (ETC, active clearing) or with passive clearing (70). While the first method is considerably faster, it causes variations in the tissue (e.g. size and colour).

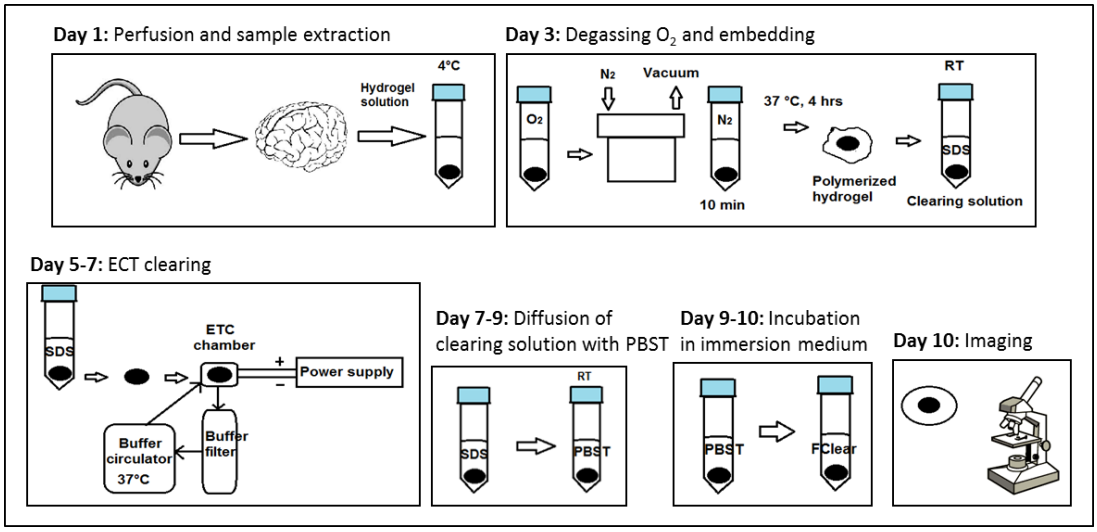

Figure 1.20: CLARITY flowchart. Day 1: Hydrogel preparation: Transcardial perfusion with hydrogel and brain incubation in hydrogel at 4°C. Day 3: degassing and hydrogel embedding, incubation in Sodium Dodecyl Sulphate (SDS) for clearing. Days 5-7 (optional): sample *active* clearing in electrophoresis chamber. Days 7-9: incubation in PBS. Days 9-10: Incubation in Focus Clear for imaging. Day 10: Imaging.

Prior to imaging, the brain is submerged in FocusClear (CelExplorer Labs), a solution that aims to match the refractive indices of objective, immersion medium and tissue. Despite its advantageous refractive index (n~1.45), FocusClear is prohibitively expensive; hence 85% (vol/vol) glycerol has been used as imaging agent, showing a degree of clearing close to the one of FocusClear (68).

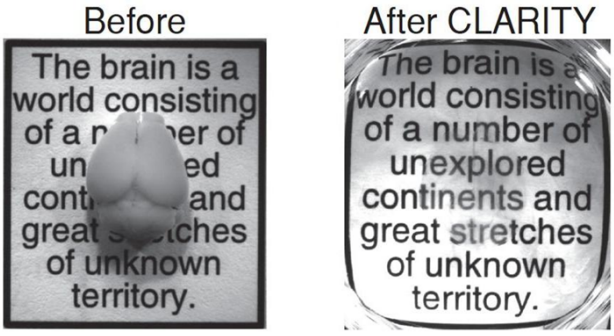

Figure 1.21: CLARITY technique for optical clearing. In the image, an adult mouse brain is shown before (left hand side) and after (right) optical clearing. The image has been adapted from ref. (69).

Yang et al. have developed RIMS (Refractive Index Matching Solution), an imaging medium which achieves good optical clearing and preserves fluorescence of eYFP, with the advantage of being considerably cheaper than FocusClear (71). They also established a new clearing technique named PARS (Perfusion-assisted Agent Release in Situ) to clear a whole mouse and to overcome the main limitations of CLARITY: tissue expansion and need of ETC or slowness of the passive clearing process. Like CLARITY, in PARS the lipid component of the organism is replaced with a hydrogel that is injected through whole animal perfusion. Both clearing and labelling happen in situ. This helps to minimize tissue swelling since the organs are constricted by the surrounding musculoskeletal structures.

Inspired by Sca*l*e and CLARITY, CUBIC (clear, unobstructed brain imaging cocktails and computational analysis) achieves sample clearing through passive lipids diffusion, hence the process is slow and not suitable for big specimens (72). However, it shows good fluorescence preservation. Indeed, the high percentage of triton used for lipid removal results in a high degree of protein loss (54). Having found with optical clearing a way to minimize light scattering, which has been so far the main limiting factor of microscopy, the aspect of fluorescence imaging that now needs to be investigated is that of imaging techniques and microscopy components. Moreover, now that big samples (~1 cm^3) can be cleared hence imaged to analyse the internal structure, the data sets have incredibly multiplied in size. This represents a further challenge, since not only these data have to be acquired, but also stored and analysed.

1.9.2 Sample preservation in tissue optical clearing

While each of the examined techniques for optical clearing has strengths in a very specific application, none of them is able to fully surmount the most common obstacles: unconfirmed generalizability across organs other than brain or embryo, difficulties in execution, and most of all sample preservation. Some important features of sample preservation are summarized in this paragraph.

- **Structure preservation (shrinking due to removal of water/ swelling due to removal of lipids)**

  Clearing approaches that include a dehydration step often cause tissue shrinkage (up to 50%) (59). On the contrary, clearing methods based on hyperhydration are able to achieve better clearing but also cause the tissue to expand. This expansion can be minimized with addition of glycerol in the clearing solution, which lowers the concentration of water that has access to protein moieties (54).

  Also, methods which include the use of an hydrogel to maintain the structure of the sample after lipid removal, such as CLARITY, tend to expand the tissue by a factor of up to 4.5 times (73).

- **Protein loss and retention of fluorescence**

  One main limitation of those clearing methods based on dehydration is that they remove water molecules from the sample that are necessary to maintain emission from most fluorescent protein chromophores. Moreover, instability of native fluorescence in organic solvents such as BABB constrains imaging of modest signals that can be easily quenched (68).

  Furthermore, some of the clearing methods that aim at lipid removal, such as CUBIC, use very high triton levels (up to 50%). This can result in a high degree of protein loss (24%-41%), which might weaken immunostaining (68).

- **Effects of temperature and incubation times**

  In those procedures that include immunolabelling, very long incubation times (even weeks) increase penetration of antibodies through large tissues. It has been demonstrated that those approaches that embed the tissue in large pore hydrogels are more likely to show rapid and complete immunolabelling (71).

High temperatures generally improve optical clearing. Indeed, temperature can change the refractive index of some solutions. For instance, the refractive index of a saturated fructose solution reaches 1.49 at 25 °C and 1.502 at 37 °C (65). However, long incubation periods (> 7 days) in solutions like fructose can cause browning and autofluorescence accumulation, especially at high temperatures (e.g. 37 °C) (65). This is due to the Maillard reaction, which is the chemical reaction between amino acids and reducing sugars.

1.10 *Ex vivo* imaging of large tissue samples

Optical imaging has recently moved towards imaging of large samples (0.5 mm to 10 mm) with systems like OPT and SPIM. These are described in the next paragraphs.

1.10.1 Optical projection tomography

OPT can be considered the optical analogue of X-ray CT. Depending on various parameters such as numerical aperture and focal length of the objective lenses, it can provide high isotropic resolution (~3 μm) 3-D images of both fluorescent and nonfluorescent, non-scattering (optically cleared) biological samples of up several mm^3 in size.

OPT was developed by Sharpe in 2002. A few years later, the first commercial OPT system was brought to market by Bioptonics (MRC Technologies). This commercial OPT system was used to image specimens for the experiments described in this thesis and is shown in the following figure (Figure 1.22). The filters provided with the machine were integrated with other filter sets to match the requirements of the experiments for this thesis.

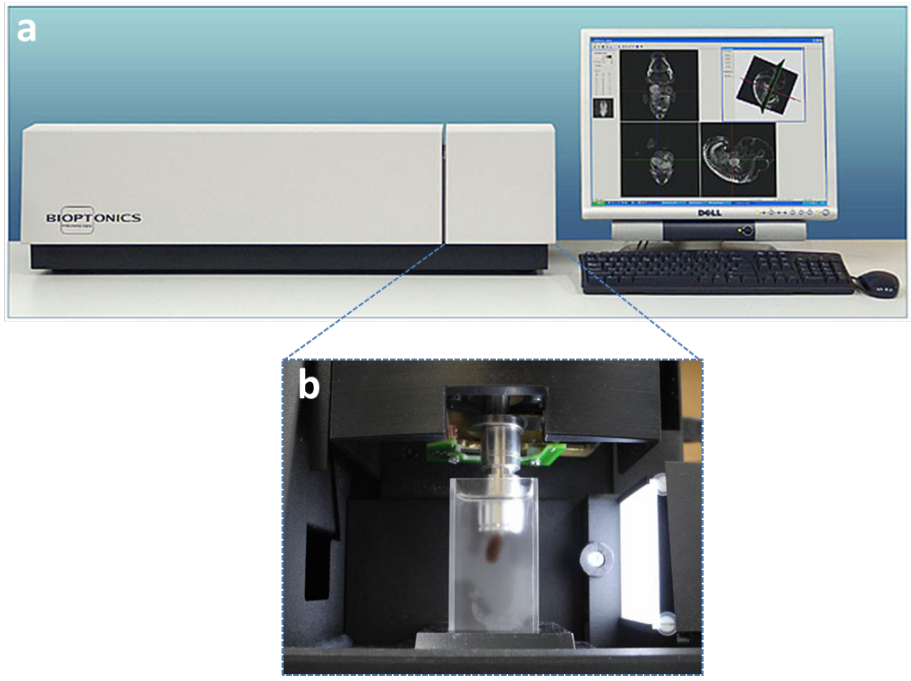

Figure 1.22: Photo of the standard commercial optical projection tomograph used for the experiments of this thesis. a) The commercial OPT manufactured by Bioptonics, Edinburgh. b) Blow-up image of the sample holding part of the OPT system. The specimen is attached to a magnetic mount, which is connected to the motor and rotated over 360 degrees. During image acquisition, the sample is fully immersed in the same solution used for optical clearing with the aim of reducing light scattering.

1.10.1.1 Data capture in OPT

The principle of functioning of OPT is depicted in figure 1.23.

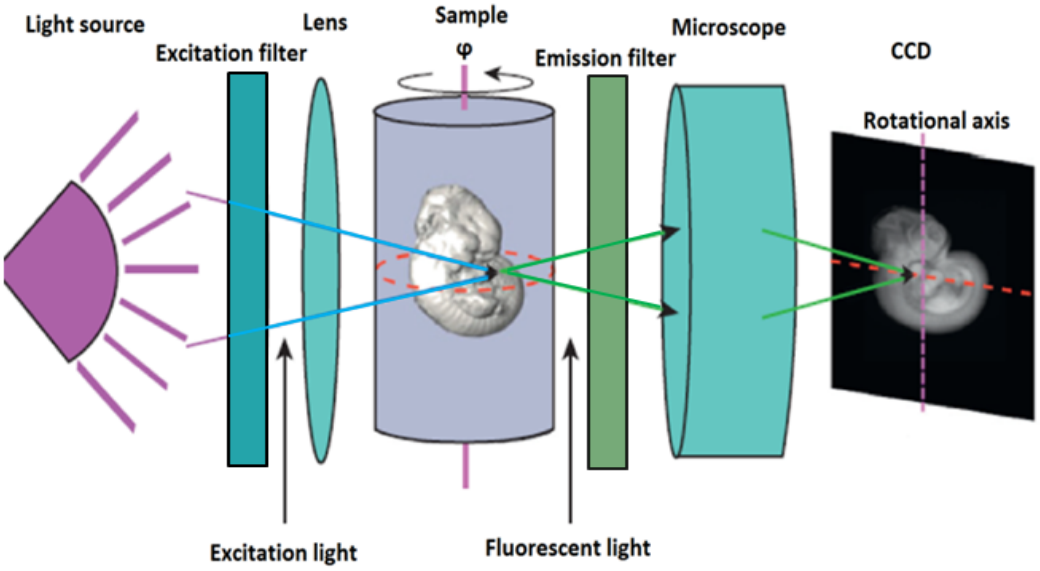

Figure 1.23: Principle of functioning of OPT. The sample is rotated about its vertical axis while under illumination in the IR-UV wavelengths. A series of optics focus the illumination onto the sample and then the fluorescent light to a CCD camera. An image is acquired at a series of angles and tomographic reconstruction is performed using a back-projection algorithm.

As discussed in section 1.9, light scattering and absorption within the sample is overcome by optical clearing, which aims to render the sample optically transparent to both excitation light and fluorescent light emitted by the specimen.

In OPT, optically cleared samples embedded in a block of agar are attached to a motorized stage and rotated through 360 degrees within the scanner to allow acquisition of projections from the sample at each orientation (with a step size of 0.9 degrees in the Bioptonics system). The sample is suspended in a square quartz cuvette filled with the same solution used for optical clearing (Figure 1.22 b), in order to reduce light scattering and reduce heterogeneities of refractive index throughout the specimen. Cuvettes are often made from quartz, whose refractive index (n=1.5) is close to that of the imaging solution that they contain (n~1.55) to reduce light scattering at the interface between the cuvette and the imaging solution.

Light emitted by a dedicated source traverses through an optical diffuser to achieve a homogeneous illumination of the specimen. Inside the specimen, light is a) absorbed and scattered due to the specimen's optical properties, or b) absorbed by contrast

agents such as coloured dyes or fluorescent probes. Light that is influenced by the specimen's optical properties results in an absorption tomogram which can be assumed of as a topographic map of the absorption coefficients of the specimen.

To detect light emitted from within the sample, a fluorescent filter is placed in front of the charge-coupled device (CCD) camera, so that the excitation light is filtered and only fluorescence signal is detected. A series of projections of the sample is recorded during its rotation, and reconstructed with a standard back-projection algorithm (discussed in section 3.2) (2). This setup allows projection data covering the entire sample to be acquired at medium resolution (516x516) within about 10 minutes or at high resolution (1024x1024) in approximately 20 minutes with the Bioptonics OPT.

OPT data can be acquired in two modes: optical absorption (transmission mode) or fluorescence (emission mode). In transmission mode, differences in the optical absorption of the sample are used to acquire images of the specimen. The light emitted from the sample is focused onto a single row of pixels on the camera-imaging chip (Figure 1.23, red line). In emission mode, a filter placed between the sample and the optics blocks the excitation light and allows registration of only the light emitted from within the specimen. Transmission mode is useful for acquiring images of tissue structure and morphology through tissue autofluorescence.

1.10.1.2 Advantages and limitations of OPT

On a microscopic scale, conventional confocal and multiphoton microscopy do not have high penetration depth (typically <1 mm), hence they can only resolve structures at the surface of an organ (32). Conversely, standard microscopic techniques, in which tissue samples are sliced into 2-D sections, allow for microscopic resolution. However 3-D reconstructions of multiple sections are challenging due to mechanical distortions that occur during sample slicing (74). Due to these limitations, new optical imaging techniques such as OPT have recently been developed. These allow 3-D imaging of whole specimens without the need for

physical slicing. These exciting new approaches can yield single cell, isotropic resolution (75).

OPT, ideally suited for specimens between 0.5 mm and 10 mm (76), fills an imaging gap between confocal microscopy and MRI (75, 77). The main revolution of OPT, compared to conventional microscopes, is the principle of functioning, based on tomographic projections reconstructed mathematically to obtain a 3-D representation of the object. OPT can be applied to image fluorescence, using tissues expressing fluorescent proteins of stained with dyes, or to image optical absorption of the tissue. Compared to MRI and μCT, OPT can generate morphometric information at even finer resolution but over a smaller field of view (FOV).

Many versions of OPT devices have been developed in the past few years, according to the specific needs of individual researchers. In addition, novel fluorophores and markers are constantly being developed for specific physiology and pathology through exogenous contrast agents or exploitation of endogenous disease characteristics. It is this diversity that makes not only OPT but also the whole field of optical imaging a vibrant research area.

Despite the numerous advantages, OPT presents a few limitations. The principal disadvantage relies in the sample processing required: as the tissue has to be transparent, OPT can so far only be used to image excised samples, as the process of chemical clearing is highly toxic. Consequently, the penetration of OPT is mostly dependent on the penetration and efficacy of the clearing process, rather than the optical components of the system.

A further limitation of OPT is photobleaching, as samples are continuously illuminated during image acquisition. This can cause a decrease fluorescence and autofluorescence signal.

1.10.1.3 Applications of OPT

OPT was first designed for use in mouse embryo phenotyping (77), with mouse vasculogenesis (78) and perturbations in vascular patterning due to genetic manipulations providing some of the first applications (79, 80). Subsequently, in

2008, a high-resolution, 3-D atlas of mouse vascular development was created by Walls et al to image embryos, which were immunostained with the endothelial marker PECAM-1 to describe mouse normal vasculogenesis (15). In 2011, Jeansson et al investigated the role of the vascular growth factor angiopoietin as a regulator on blood vessels development in embryos (80). Cardiac development was imaged in three-dimensions through OPT by Takeuchi (81), and kidney development has been studied with OPT by Short and Smyth (82).

OPT has been used not only to study developing organisms, but it is also a fundamental tool to analyse structural changes in adult tissues caused by diseases such as diabetes (83). Equally OPT has been used to study immunology: Kumar et al examined the remodelling of peripheral lymph nodes after infection (84), and demonstrated that acute autoinflammatory lymphadenopathy can be associated with high endothelial venule expansion.

Researchers are currently investigating the potential of OPT in living organisms to study organogenesis. A life-support chamber used to analyse the developing limb bud of a mouse embryo was recently described by Sharpe et al (85). Modifications in hardware and the development of sophisticated software algorithms (86, 87) have made possible the real-time visualization of internal structures, such as the skeletal and nervous systems of a zebrafish (88). The main application and advantage of OPT still remains the possibility to combine the overall morphology of the organ or embryo with the 3-D visualization of gene expression through the use of fluorescent antibodies (89).

It is therefore clear that the combination of advanced microscopy techniques such as OPT and tissue optical clearing techniques allow 3-D analysis of microstructures of whole tissues with unprecedented detail.

1.10.2 Single plane illumination microscopy

SPIM, also known as light sheet fluorescence microscopy (LSFM) is a fluorescent microscopy technique generally used to image small organisms (such as embryos and zebrafish), with subcellular resolution (90). In SPIM, volumetric images of a specimen are acquired by using a thin plane of light (light sheet) to illuminate the

sample. The first prototype of SPIM was developed by Siedentopf and Zsigmondy in 1902 and was named an *ultramicroscope* (91). This microscope was further improved and developed by Huisken in 2004 (90).

As with OPT, samples are prepared for SPIM by embedding in a block of agar and are placed in a chamber filled with clearing solution (or water, for live organism imaging). The specimen is connected with a rotational and translational stage and rotated along a vertical axis within the chamber. Raw images are then reconstructed using a joint deconvolution of data acquired along multiple directions, allowing the formation of a single 3-D image. This procedure is known as multi-view reconstruction (92).

In SPIM, the excitation light sheet is generally formed using a cylindrical lens. In an ideal setup the light sheet would be uniform across the FOV. In the real case, the excitation light converges towards the samples and diverges away from it (Figure 1.24 b), and the waist of the light-sheet is placed in the middle of the FOV. To remain uniform throughout the entire sample, the light sheet thickness (usually 1-10 μm) can be adjusted with zoom optics and irises according to the sample size: ~1 μm for small samples (20-100 μm), or thicker (~5-10 μm) for bigger samples (1-5 mm) (93). The thickness of the light sheet corresponds to the volume that is illuminated, and therefore defines the axial resolution of the microscope, which is the resolution along the optical axis of the detection lens.

When compared to wide-field microscopy, confocal microscopy and OPT, SPIM can reduce photobleaching and phototoxicity. Indeed, in a common wide-field or epifluorescent microscope, the light emitted by the specimen is collected through the same objective used for illumination (Figure 1.25 a), hence the whole sample and all the fluorophores within the specimen are constantly illuminated when recording a single plane. On the contrary, in SPIM only a narrow volume of the sample around the focal plane is illuminated by the excitation light, causing reduction of photobleaching.

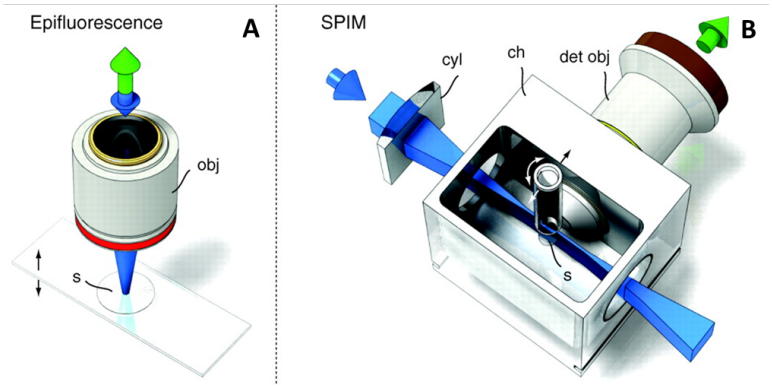

Figure 1.24: Comparison of the light path in different microscopy techniques. In epifluorescence microscopy (A) illumination and detection axes coincide. The sample is placed on a coverslip. SPIM (B) uses at least two independently operated lenses. The sample, rotated within a chamber during imaging, is illuminated through an objective lens (blue arrow) and the signal emitted is collected by the detection objective, which is placed at 90 degrees (green arrow). The light sheet is formed by a cylindrical lens. The image is adapted from ref. (94).

In figure 1.25 the lateral illumination of SPIM is shown to illustrate its advantages over LSCM. SPIM allows not only reduced photobleaching (Figure 1.25 A-B), but also reduced scanning times (Figure 1.25 C-D). Indeed, in SPIM the fluorescent light emitted by the sample is collected by a CCD camera, which records multiple pixels at the same time without the need to raster scan.

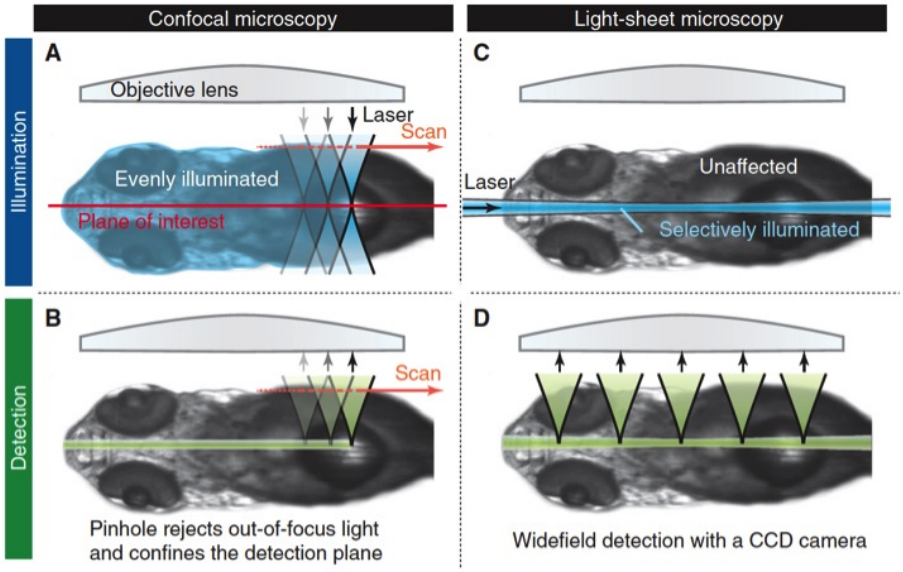

Figure 1.25: Advantages of Light sheet fluorescence microscopy (C, D) over confocal microscopy (LSCM, A, B). In LSCM, the illumination light is focussed and scanned across the sample, which is evenly illuminated at all times. In Light Sheet Microscopy, only a thin

slice of the sample is illuminated. As result, in Light sheet microscopy, image acquisition is faster and sample photobleaching is reduced compared to confocal microscopy. The image was adapted from ref. (94).

To summarise, the main advantages of SPIM are ability to image whole biological samples, high penetration, fast image acquisition and low bleaching. A major drawback of light sheet illumination techniques is that they are limited to fluorescence imaging; hence they cannot be used in transmission mode to deliver anatomical information, as it can be done with OPT.

1.10.3 Optical sectioning

The need for volumetric imaging is related to the inherent complex, heterogeneous, 3-D structure of organs and organisms. 2-D analysis of tissue sections cannot provide a complete, representative overview of a whole organ or tumour. Whilst 3-D information can be reconstructed by combining together a series of images of serial thin sections acquired, this is time-consuming and imprecise due to loss or distortion of individual sections that cause a rough and potentially imprecise final volumetric reconstruction. In fact, the distance between the slices is usually too coarse to avoid loss of 3-D information (45).

Due to light scattering, wide-field microscopy is generally unable to image thick samples, where volume datasets or selection of data from within a specific focal plane is desired. In contrast to wide-field microscopy, confocal and 2P microscopy allow the visualization of thin planes from within a thick bulk sample, which is known as *optical sectioning*. An optical section refers to a slice through a sample. Optical sectioning, in which 2-D single slices of an intact sample are acquired by either selective excitation with a cone beam of light or by minimizing the contribution from other parts of the volume, allows precise and reliable imaging of biological structures in 3-D. Furthermore, optical sectioning is critical for elimination of out-of-focus light when imaging fluorescently labelled samples with confocal microscopy.

Compared to wide-field microscopy, confocal microscopy not only improves the depth of field, but also dramatically improves contrast. In laser scanning microscopy

techniques such as confocal and 2P microscopy, optical sectioning involves focusing the laser within the sample and scanning the beam across the horizontal plane at that specific depth with the aim of filtering out and removing the contribution of out-of-focus light in each image plane and recreating 3-D representations of thick specimens (Figure 1.26). While in confocal microscopy optical sectioning is obtained by focusing the light with a pinhole, as seen in section 1.6.2, in multiphoton microscopy, the elimination of out-of-focus signal given by the very low probability of a multiphoton absorption event occurring provides inherent optical sectioning capabilities without the need for a confocal pinhole.

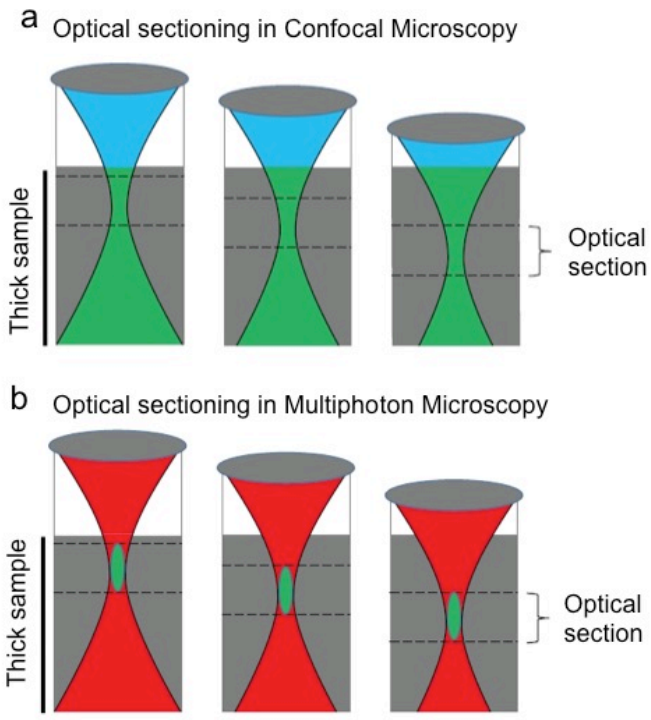

Figure 1.26: Optical sectioning in confocal and multiphoton microscopy. The signal generated by the sample is shown in green. Optical sections are formed by discretely measuring the signal generated within a specific focal plane. A) In confocal microscopy, out-of-focus light is rejected through the use of a pinhole aperture, thereby leading to higher resolution. B) In multiphoton LSM, signal is only generated in the focal volume. Signal collected at each optical section can be reconstructed to create a 3-D image.

Another method for 3-D imaging of biological structures is to image only the surface of a sample and then sequentially physically section slices in order to expose deeper structures. This sample-destructive technique is used in HREM (95), and eliminates the loss and distortion associated with the realignment of serial sections.

Other approaches include SPIM, where optical sectioning is achieved by illuminating the sample with a laser light sheet along an optical path orthogonal to the detection axis, as described in section 1.10.2. It has been demonstrated that this design improves axial resolution when compared to epifluorescence approaches (93) In a SPIM axial resolution is determined by the thickness of the illuminating light sheet and the NA of the detection lens. Here, optical sectioning is greatly enhanced through the use of optical clearing agents, which render specimens transparent (optical clearing). The net effect of the optical sectioning approach of SPIM is similar to that achieved by multiphoton microscopy, in which only fluorophores in the location of interest is excited, but is achieved in different ways. As discussed earlier, in multiphoton microscopy this is undertaken through the use of a focused, high-power NIR laser beam, which excites only a small area within the sample. However, the long wavelength used limits the image resolution (see Eq. 1.2) and the high power of the laser can overheat the sample, potentially damaging the tissue as well as reducing its fluorescence.

An alternative to optical slicing is OPT, described in section 1.10.1. Rather than reducing depth of focus in order to detect signal coming only from a precise depth within the sample, the aim of OPT is to maximize the depth of focus in order to cover the entire sample (75). The data acquired in this way do not directly contain information about depth, which is instead obtained with tomographic reconstruction software.

1.10.4 Deconvolution

An alternative to confocal scanning and 2P fluorescence excitation microscopy is deconvolution, also known as computational optical sectioning microscopy (COSM). In COSM, as with a confocal microscope, a 3-D image is collected as a series of 2-D images (or optical slices), each with the microscope focused at a different plane through the specimen. If a wide-field microscope is used, each of the 2-D images has the in-focus information plus substantial contributions from out-of-focus material. In COSM, a computational method derived from information about the process of image formation and recording is used to remove the out-of-focus light from each optical slice. Several methods have been derived for COSM whose differences stem

from the different mathematical models used for the process of image formation and recording.

1.11 Comparison of imaging techniques

CT, MRI and US are label-free methods, which makes them especially useful for imaging in humans and living organisms. Fluorescence methods instead all require the use of a label, which can be a strength, in terms of specificity, but also a weakness, in terms of sample manipulation.

The main limitation of US is the low signal-to-noise ratio when compared to CT. Some other limitations include the presence of air and bone artefacts (which do not transmit sound waves) and limited depth penetration at the higher frequencies required to resolve small structures (96).

The use of CT in cancer studies can be problematic as X-rays can also have a therapeutic effect, which can complicate the analysis of disease progression and therapeutic response. Radiation therapy is in fact a powerful therapeutic approach.

The chief advantage of MRI is its excellent tissue contrast (97). Furthermore, the advantage that both MRI and CT have over OPT and LSFM is that they can acquire information of internal structures of specimens that are too opaque for OPT and LSFM, which instead require tissue optical clearing and therefore are only appropriate for post-mortem imaging. However, the limitation of CT, MRI and US is their spatial resolution: 12-50 μm for CT/μCT (96, 98) and 4-100 μm for MRI/μMRI (96, 99), 50 μm for US (96). Such low spatial resolution is not sufficient for visualization of cellular and sub-cellular events; hence these techniques are not ideal to study tumour angiogenesis, vascular function and microenvironment (96).

Electron microscopy has offered a resolution of ~5 nm for imaging biological tissue (100). However, to prepare a sample to be imaged by an electron microscope is a rigorous process that does not allow for imaging of live samples (101). One common sample preparation technique is cryofixation, which is a high pressure and deep freezing technique that results in contrast in electron microscopy (102). Even though

the samples are no longer viable, electron microscopy has provided invaluable insights on the structural details of organelles and membranes (103).

Likewise, while quantitative analysis at tissue, cellular, sub-cellular and molecular levels is provided by histological and molecular methods, these techniques are highly invasive as they rely on physical slicing, as discussed in section 1.6.3. This makes these techniques not suitable for the analysis of relevant tumour parameters, such as vascular networks.

Although confocal and 2P microscopy are very efficient at generating 3-D images of fluorescently labelled specimens, they are limited to analysis of specimens up to only a few hundred micrometres in thickness (42). Indeed, limited penetration due to light scattering in tissue is a limitation of optical techniques in general. This can be partially ameliorated by using more powerful lasers, but this in turn can lead to increased photobleaching effects, which can limit the amount of time that an experiment can run. Another way to increase light penetration is optical clearing, discussed in section 1.9.

By the use of optical clearing, techniques such as OPT and LSFM can achieve 3-D images of whole fixed organisms with resolution of ~1-10 μm and 0.5-10 μm, respectively (48). These methods can be applied to image fluorescence, and they also have the big advantage that they are non-destructive and do not alter morphological characteristics of the organism as may be the case when physical tissue sectioning is used, as discussed in section 1.10.3.

1.12 OPT and SPIM- Filling in the imaging gap

As discussed in the previous section, two fundamental imaging parameters are penetration depth and resolution. Other parameters that need to be considered in the choice of the imaging techniques are the degree of photobleaching they cause, the time allowed for image acquisition, the implementation complexity and the cost.

Imaging beyond TMFP = 1 has not yet been achieved with optical imaging due to light penetration limitations. Indeed, despite confocal and 2P microscopy are very

efficient at generating 3-D images of specimens which have been fluorescently labelled, these techniques are mainly used to image specimens up to only a few hundred micrometres in thickness. Between the two, 2P can achieve higher penetration compared to confocal microscopy (32). However, the lateral resolution of 2P microscopy is worse than that of any conventional fluorescence microscopy and it requires significantly higher light intensities than any other technique (104).

Whilst information deep in tissue in specimens that are too opaque for optical imaging can be obtained with techniques such as X-ray CT and MRI, these approaches have limited spatial resolution. Techniques such as OPT and SPIM, which fill the resolution/penetration size gap (between 0.5 mm and 10 mm, Figure 1.27) between CT/MRI and confocal microscopy (105), have been investigated and applied to the study of biological tissue in this thesis.

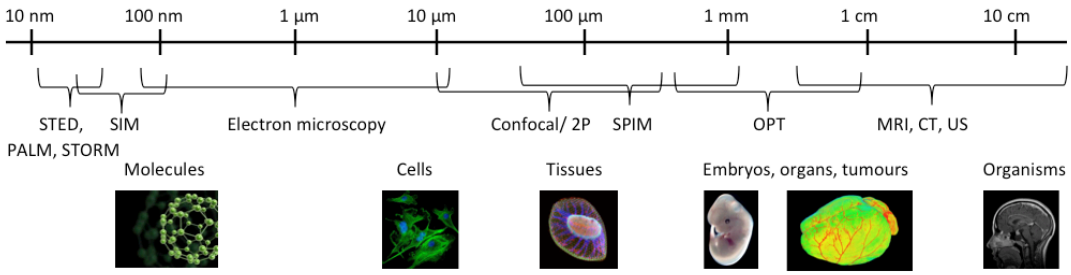

Figure 1.27: Sample size range for several imaging techniques. OPT and SPIM fill an imaging gap between super-resolution (alongside electron/confocal/2-photon microscopy) and techniques used for large samples (such as MRI, CT and US). Super resolution techniques considered here include structured illumination microscopy (SIM), stimulated emission depletion microscopy (STED), photoactivation localization microscopy (PALM) and stochastic optical reconstruction microscopy (STORM).

Performance characteristics of the imaging techniques described in this chapter are summarized in Table 1.3.

Table 1.3: Comparison of imaging systems

Name	Wavelength	Resolution	Contrast	Size	Imaging time	Cost (£)	Photobleaching
MRI	Radio	mm	Magnetic dipole	M	hr	Millions	NA
CT	Gamma	<mm	Absorption	cm	min	Millions	NA
CLSM	Visible	<µm	Fluorescence	µm	sec-min	150,000	Yes
2P	IR	<µm	Fluorescence	mm	sec-min	400,000	Yes
OPT	Visible	<µm	Fluorescence, Absorption	>cm	sec	30,000	Yes
LSFM	Visible + IR	µm	Fluorescence	>cm	sec-min	30,000	Less

Table 1.3: A comparison of imaging systems. In this table, some of the imaging techniques analysed in this thesis are compared. Resolution is approximate and refers to the average resolution provided by different systems. Size refers to the samples that can be imaged. Time refers to the average time it takes to acquire a stack of the sample. The cost (£) is approximate. The table was adapted from Santi (105).

Even though they require optical clearing, OPT and SPIM are nondestructive methods that produce well-registered optical sections suitable for 3-D reconstruction and can also be processed by other histological methods (e.g., mechanical sectioning) after imaging. SPIM and OPT offer higher resolution (subcellular) and faster imaging speed compared with other nondestructive tomographic devices such as MRI and CT. Compared with confocal and 2-P microscopy, SPIM and OPT are able to image thicker tissues (>1 cm). Finally, the cost of construction of OPT and SPIM systems is much less than other microscopes (105). Because of these advantageous features, OPT is the imaging technique most used in this thesis, which focuses on imaging structures deep within whole organs and tumours.

1.13 Investigation of tumour models and OPT for *ex vivo* imaging

The quantitative analysis of tumour growth and angiogenesis as well as the effects of new treatments on tumour models are essential to evaluate the potential of anticancer compounds. Imaging has a large role in detection and treatment of cancer. Different macroscopic and microscopic techniques discussed in this chapter are used to study the heterogeneous structure of tumours and its interaction with therapeutic drugs (106).

Alongside laparoscopy and biopsies, CT and MRI are commonplace in tumour diagnosis. They can monitor various tumour parameters with a spatial resolution down to 50 μm (96) (107). Furthermore, they allow measurements of tumour perfusion, which have the potential to inform on tumour malignancy and therapy efficacy (108, 109). However, cellular resolution is necessary to get more comprehensive information regarding the effects of antitumour substances. Although techniques like US, CT, and MRI allow for whole body imaging, even the highest attainable resolution cannot resolve microscopic details such as the structure of individual cells (110, 111).

Intravital confocal and 2P microscopy can study in 3-D multiple biologic in vivo events down to cellular resolution. However, because of the slight penetration depth of 500 μm and the small field of view these techniques cannot image an entire tumour sample (112, 113).

Conventional histology is still the gold standard in tumour analysis. However, 2-D examination of a few slices cannot provide a comprehensive description of a whole tumour, characterized by a complex and heterogeneous structure. Histological slices can be reconstructed in 3-D, but this is a laborious and time consuming process which also encounters the difficulties of mechanical distortion of the tissue slices.

Ex vivo approaches such as optical projection tomography allow microscopic resolution and hence can be a valuable validation method for *in vivo* imaging techniques. In the present thesis, OPT was applied to the field of tumour analysis to overcome the limitations of conventional imaging techniques. OPT in combination with optical clearing techniques enabled the 3-D measurements of large tumour samples up to 1 cm in diameter with a spatial resolution of about 5 μm.

1.14 Structure and overview of the thesis

This thesis is structured into six chapters.

Following the theoretical background and description of thesis structure in the current chapter, Chapters 2-4 describe experimental results. Each chapter contains a brief introduction to outline the aim of the chapter and any specific background that was not presented in Chapters 1 and 2. Each chapter also contains a description of the methods used for the research, a description of all the results obtained and a general discussion of these results.

Chapter 2 presents the development of a spectroscopic method for light attenuation quantitation that was developed in order to compare different optical clearing techniques. The method is tested in the three clearing approaches. Most of the work in this chapter has been published in the *Journal of Biomedical Optics* (d'Esposito A., Nikitichev D., Desjardins A., Walker-Samuel S., Lythgoe M. F., "Quantification of light attenuation in optically cleared mouse brains").

Chapters 3 and 4 apply the optical clearing approach discussed in Chapters 1 and 2 to the study of vasculature structuring in both normal and diseased tissues.

In Chapter 3, two different approaches for vasculature labelling are analysed and compared: perfusion with radiopaque polymer injection media and vasculature labelling with fluorescently labelled proteins. Furthermore, two *ex vivo* imaging techniques for imaging of blood vessels are compared (μCT and OPT).

In Chapter 4 a subcutaneous model of colorectal carcinoma is investigated by OPT. First of all, the fluorescence labelling approach for blood vessels described in Chapter 3 is applied to the study of colorectal carcinoma and its treatment. The vasculature of xenograft subcutaneous tumours is analysed with optical projection tomography in control samples and in tumour treated with a vascular disrupting agent. The same approach for vasculature labelling is also applied to the investigation, by OPT and HREM, of vascular networks in a model of colorectal carcinoma that metastasizes in the liver. Furthermore, the ability of a fluorescently

labelled carbonic anhydrase ligand to bind to the specific carbonic anhydrase IX in colorectal xenograft tumour is investigated. Finally, *in situ* whole organ optical clearing is shown as a potential validation method for *in vivo* liver perfusion analysis. Part of the work in this chapter has been submitted for publication in *Cancer Research* (d'Esposito A, Sweeney P, Desjardins A, Lythgoe M, Pedley B, Shipley R, Walker-Samuel S, "Numerical simulation and experimental validation of vascular-targeting therapy using whole-tumour optical imaging data").

The final chapter (Chapter 5) summarises the developments and results of this thesis and discusses the results relative to the broader context of the field of preclinical optical imaging. Conclusions about the techniques developments and applicability are also made.

In the appendix, methods for assembly and calibration of a SPIM according to the OpenSpim platform are described. Some preliminary applications of the microscope are also shown.

Chapter 2: Light attenuation quantitation and characterization in optically cleared tissue samples

This chapter covers the process of tissue optical clearing and illustrates a method, developed in this thesis, to estimate the transparency obtained by different clearing approaches. This method is based on spectroscopy and allows quantification of the quality of the clearing process, therefore it can be used to compare optical clearing approaches. This is particularly relevant when using imaging techniques such as optical projection tomography (OPT) and light sheet fluorescence microscopy (LSFM) to examine the structure of whole organs and tumours with cellular resolution, as shown in the following Chapters 3 and 4. Furthermore, a new clearing technique for morphological analysis of samples (named pBABB) was developed in this thesis by modification of an established clearing technique (BABB).

To summarise, the main aim of the research presented in this chapter was to establish a method to quantify light attenuation in optically cleared tissues in order to quantitatively compare different optical clearing approaches.

The present study also aimed at developing a technique for optical clearing (named pBABB) not only as simple as the BABB technique but which also achieves a higher degree of tissue transparency compared to established techniques such as BABB and CLARITY.

Finally, the degree of clearing obtained with pBABB was quantitatively compared to existing techniques by spectroscopic analysis.

2.1 Development of a spectroscopic method for quantifying clearing efficacy

Light can be scattered or absorbed within biological tissue. New techniques have recently been developed to render biological samples transparent in order to allow near-collimated light to travel deeper into tissues (54, 68, 72) by reduction of light scattering. This enables 3-D morphological information to be obtained deep within tissue samples using techniques such as optical projection tomography and light sheet fluorescent microscopy. Visualization of deep structures with high resolution is of significant interest for gaining greater understanding of biological processes in healthy and diseased tissues, and will potentially improve the capabilities of diagnostic and therapeutic techniques.

However, as covered in Chapter 1, the extent of the optical clearing is dependent on the technique that is used to process the sample. There is therefore a need for methods to quantify the quality of the clearing process in order to ease the choice of the clearing technique for the specific exigencies. Indeed, comparisons between clearing techniques have been made (53, 114), but no method for exact quantitation is available so far. This is not a straightforward process since the mechanisms of tissue optical clearing (TOC) are due to multiple factors: optical clearing agents (OCAs) increase the refractive index of interstitial fluid and lead to a refractive indices match among of various substances in tissue; hyperosmotic agents induce dehydration of tissue and consequently decrease its thickness and make it denser. All these effects raise the optical transmittance of the tissue. Since the structure and molecular composition of each tissue is different, each type of tissue interacts in a distinct way with the OCA used in the specific TOC process (115).

Choi et al evaluated the tissue optical-clearing efficacy of different chemical agents measuring the optical clearing potential (OCP), the ratio of reduced scattering coefficient of tissue measured before and after the application of OCAs (116). They measured the refractive indices and osmolality (concentration in units of osmole per kilogram of water) of each agent and demonstrated that the OCP does not correlate with refractive index of OCAs nor with their osmolality of OCAs, but only with their molecular structure.

Rylander et al have assessed optical clearing of rat skin immersed in DMSO, glycerol and air through photographic imaging (56). They have calculated tissue transmittance by placing half of the samples on a glass and the other half over a black background and measuring the reflectance. Tissue transmittance was measured by subtracting the reflectance intensity (upper part of figure 2.1) from the total intensity (lower part of figure 2.1). They assumed light absorption was negligible, hence calculated light scattering by dividing transmittance over reflectance. A high ratio indicated low scattering, while a low ratio indicated a high degree of scattering.

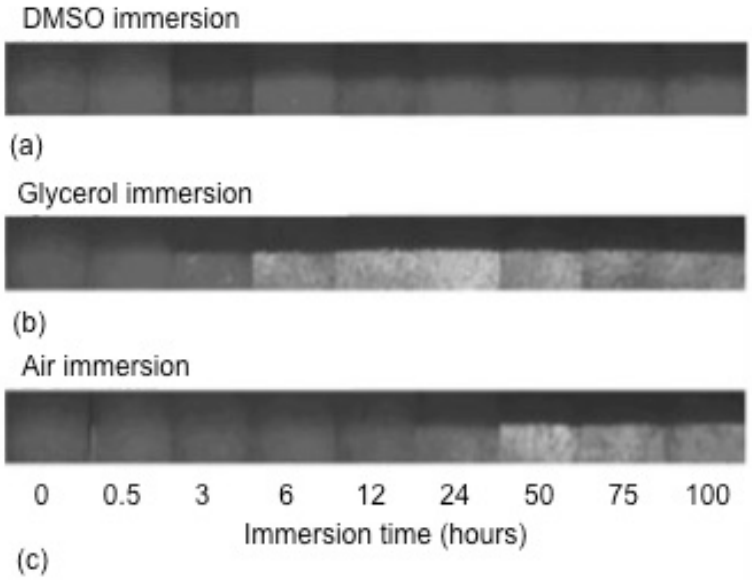

Figure 2.1: Photographic images of rat skin immersed in DMSO (a), glycerol (b), and air (c). Corresponding immersion times are listed for each image. Image adapted from ref. (56).

In the present study, a tissue transparency quantitation method using a custom spectroscopy system was developed and applied to compare the three most commonly used techniques for optical clearing in this research: BABB (Murray's clear) (117), pBABB (a modification of BABB, developed in this thesis, which includes the use of hydrogen peroxide), and passive CLARITY (69, 70). Three regions of the mouse brain were studied: olfactory bulb, cerebellum and pons. The attenuation spectra for each of the mouse brain regions and for each clearing technique were compared. The change in tissue size was evaluated by image analysis of cleared tissue slices.

Optical spectroscopy, used to quantitatively analyse the light transmission within the cleared samples, was retained to be the most straightforward approach since spectroscopy is generally used to measure light intensity at different wavelengths in order to study the interactions between light and materials. Optical spectra arising from either emission or absorption of radiant energy by various substances can be measured and interpreted with a spectrometer.

2.2 Methods

2.2.1 Animal treatment

All experimental study protocols were performed in accordance with the local ethical review panel, the UK Home Office Animals Scientific Procedures Act 1986, and United Kingdom Coordinating Committee on Cancer Research guidelines (118). All experiments were conducted under PIL 70/24922 and PPL PPL 70/7309 'Targeted Cancer Therapies' and PPL 70/7474 "Phenotyping transgenic mice". Animals' strains used were immune-deficient *nu/nu* mice lacking T-cells due to developmental absence of a thyroid gland. The background species of the mice were either MF1, procured from an in house breeding colony, or CD1 mice, procured from Charles River Laboratories, both species being ultimately outbred colonies of Swiss Webster stock (119). Animals were housed in barrier conditions within UCL BSU facilities in individual ventilated cages (IVC). Daytime conditions were simulated by a 12 hours light/dark cycle. Animals for experimentation were females between the ages of 8-10 weeks, with a seven-day acclimatisation period allowed between arrival at biological services facilities and experimental use.

2.2.2 Animal handling

All *in vivo* technical skills were acquired through previous training at the royal veterinary college London and tuition in UCL Centre for Advanced Biomedical Imaging (Dr. Peter Johnson), resulting in a home office licence for modules 1-4. Typical procedures performed included restraint via scruffing, injection of substances (cell suspensions, drug solutions, contrast agents, etc.) via subcutaneous (s.c.), intraperitoneal (i.p.) and intravenous (i.v.) routes of administration, and

induction of anaesthesia for routine imaging procedures. Animals were checked daily when under procedure and at no point showed signs of suffering or lasting harm due to experimental procedures. Termination was carried out via cervical dislocation (schedule 1 method).

2.2.3 Perfusion fixation

To prevent blood clots formation within the vasculature after the animal's death, MF1 *nu/nu* mice were individually heparinized (Wockhardt, Heparin Sodium) by intraperitoneal (IP) injection (0.2 ml/specimen, 1000 IU/ml). Mice were then terminally anaesthetized via intraperitoneal injection of 100 mg/kg sodium pentobarbital (Animalcare, Pentoject) diluted in 0.1 ml phosphate buffered saline (PBS) via a 1 ml syringe with a 25-gauge x 16 mm needle. Once anaesthesia was confirmed, surgical procedures for intracardial perfusion were performed for systemic clearance of blood. This step is particularly relevant since visible light is highly absorbed by blood, mainly due to the presence of haemoglobin in the red blood cells. Therefore, blood removal allows deeper penetration of light into tissue. The anesthetized mouse was pinned onto the dissecting tray, ventral side up within a down-flow cabinet. An incision was made below the xyphoid process, and the thoracic cavity was exposed by cutting through the diaphragm. The beating heart was exposed by folding up the sternum; a blunt butterfly needle inserted from the left ventricle was used to cannulate the aorta. It is important to keep the needle straight and not to cut through into the right ventricle. The right atrium was severed to provide blood outflow. PBS (30 ml; 37 °C) was administered with a perfusion pump (Watson Marlow, 5058) at a flow rate of 3 ml/min to simulate the natural blood flow. PBS was heated up to 37 °C to match the mice body temperature with the aim of enhancing blood removal hence improving the quality of perfusion. After the complete drainage of blood, 40 ml of 4% formaldehyde solution were administrated. Individually harvested brains were placed in sterile containers (ThermoFisher Scientific, Cambridge, UK) and stored for 12 hours in 4% paraformaldehyde (10 ml; 4 °C) (PFA, VWR chemicals) for post fixation.

2.2.4 Tissue optical clearing

After perfusion-fixation and post fixation by immersion in formaldehyde, the 12 mouse brains were rinsed three times in PBS (10 minutes each) prior to clearing to avoid residual formaldehyde which would cause over-fixation (120).

After PBS rinsing, harvested brains were sliced to obtain sagittal slices that were 2 mm in thickness. In a preliminary study the slicing was done manually with a conventional razor blade. However, this approach was not precise and could not allow acquisition of reliable light transmittance measurements. Therefore, the samples were sectioned with a brain slicer matrix (Zivic Instruments, BSMAS002-2); the two central slices close to the midline were used. The brains were cut along the sagittal rather than coronal or transversal plane to allow measurements within the three chosen area to be acquired in the same slice.
Tissue clearing was performed with new as well as established procedures: BABB, pBABB, which is a modified version of BABB, and passive CLARITY. A schematic of the experiments performed in this study is shown in figure 2.2.

For each clearing method, between 6 and 12 MF1 *nu/nu* mice were used (Figure 2.2). Precisely, 12 sagittal brain slices were cleared with BABB: 6 from the right and 6 from the left hemisphere, to compare the effect of clearing on the two hemispheres. 6 brain slices were cleared with pBABB and 6 with CLARITY.

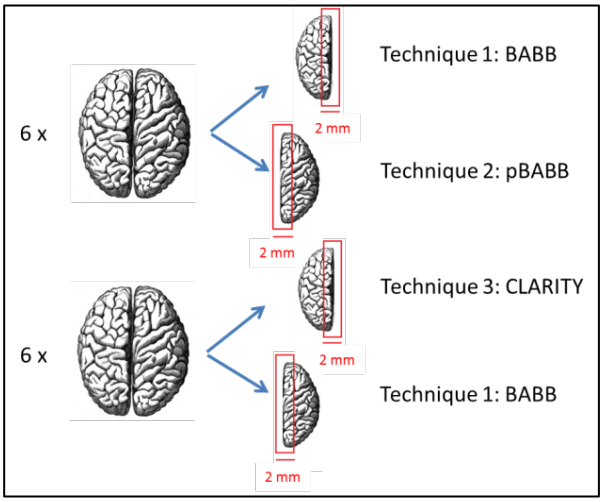

Figure 2.2: Schematic diagram of the experimental protocol. The two 2 mm thick sagittal central slices taken from each hemisphere (red rectangles) were cleared with BABB, pBABB and CLARITY for spectroscopic measurements of light attenuation. A total of 12 samples were used for this study

2.2.4.1 BABB optical clearing

BABB clearing preparation consisted of dehydration in methanol (MeOH, Sigma-Aldrich, 99.8% purity) for 48 hours at room temperature and clearing in BABB for 48 hours. BABB is a 1:2 mixture of benzyl alcohol (Fisher Scientific, 99% purity) and benzyl benzoate (Fisher Scientific, 99+% purity). For immersion in BABB, glass containers were used. Indeed, BABB is highly corrosive.

During clearing, samples were kept on a rotator (Bibby Scientific, Stuart SB3) to facilitate the clearing process. This detail is not part of the original BABB protocol, but it was added in the present work as it was notices that shaking the samples reduces the optical clearing times.

2.2.4.2 pBABB optical clearing- Development of the clearing method

pBABB clearing is a new technique developed in this thesis by modification of BABB clearing technique. As BABB, it aims at dehydration of the tissue and replacement of water with a solution of higher refractive index, to match that of the cell membrane. However, in the pBABB techniques pigments are removed from the tissue to reduce light scattering and absorption. This is achieved through a bleaching step: before the dehydration step, samples are submerged for 1 hour at room temperature in a mixture known as Dent's bleach (121) and composed by 4:1:1 methanol: dimethyl sulfoxide (DMSO, Sigma-Aldrich, 99.8% purity): 35% hydrogen peroxide. Since DMSO is a solvent, it is used here as penetration enhancer to increase absorption of the clearing agent by the tissue (60). While Dent's bleach is widely used for antibody staining (122), it has never been used before as an optical clearing technique. After the bleaching step, samples underwent three 2-minutes degassing cycles with a vacuum pump (KNF Neuberger, Laboport) to allow the oxygen gas introduced by the hydrogen peroxide out of the tissue and avoid formation of bubbles, which would cause not only tissue disruption but also light diffraction during imaging. This step is very important and was added to the protocol after imaging the first samples cleared with pBABB. Indeed, despite the transparency degree was higher than that of samples cleared with conventional BABB, the samples cleared with pBABB and not degassed presented bubbles, which are a remarkable cause of imaging artefacts. Figure 2.3 shows an example of a brain

sample cleared with pBABB and not degassed. The red arrows indicate the presence of a bubble in the raw projection (Figure 2.3 a) and in the reconstructed slice (Figure 2.3 b).

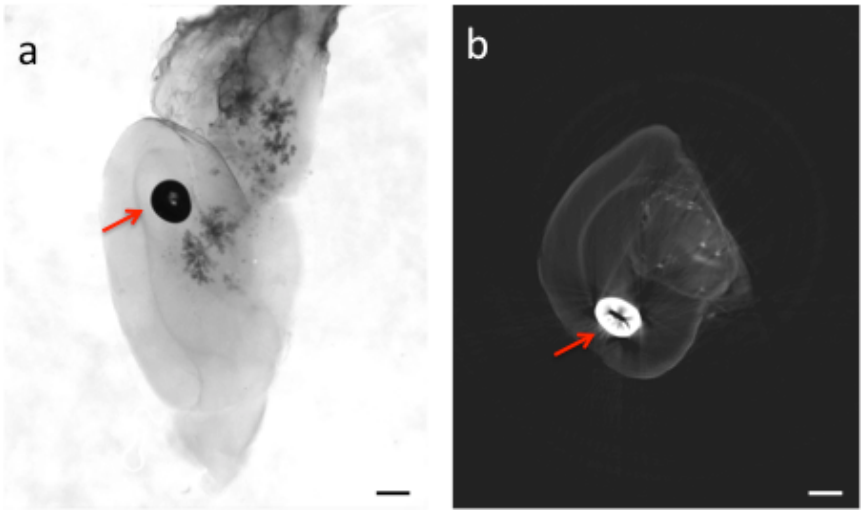

Figure 2.3: Half mouse brain cleared with pBABB and not degassed. The red arrows point at bubbles in the raw projection (a) and in the reconstructed slice (b).

After degassing, samples were rinsed twice with 100% MeOH to wash the hydrogen peroxide away and then they were dehydrated in MeOH. After 48 hours samples were transferred for clearing to BABB solution, where they were kept for 48 hours at ambient temperature.

2.2.4.3 CLARITY optical clearing

The CLARITY clearing technique (68) aims at creating a physical framework to support the tissue after removing the lipid bilayers that form the cell membrane. This is obtained by infusion of a hydrogel monomer and consequent hydrogel and tissue hybridization, as it was described in section 1.9.1.

For the present study, the CLARITY protocol (68) was modified for passive clearing, as described by Tomer (70). This passive CLARITY protocol included preservation of tissue structure with hydrogel embedding: after perfusion-fixation and rinsing in PBS, samples were immerged in hydrogel solution (Acrylamide, Bis-acrylamide, VA-044 initiator, 16% paraformaldehyde, 10x PBS, dH_2O) at 4 °C for 48 hours.

Brains were then degassed to remove oxygen from inhibiting polymerization and then incubated at 37 °C for 4 hours to allow hydrogel polymerization. Once the gel had polymerized, the excess gel was removed from the samples. To allow thermal clearing of lipids, samples were placed in 50 ml clearing solution (clearing solution: boric acid, sodium dodecyl sulphate (SDS), dH_2O, NaOH) at room temperature. The clearing solution was replaced after 24 hours and the samples continued incubation for 30 days. The clearing solution was then diffused out by immersing the samples in PBST (PBS with Tween20) for 48 hours. 48 hours prior to imaging the PBST was replaced by the immersion medium (80% glycerol).

2.2.5 Light attenuation quantitation

The measurements of light attenuation were undertaken in collaboration with Dr Daniil Nikitichev and Dr Adrien Desjardins.

For this study, spectroscopic light attenuation measurements were performed with a custom system (Figures 2.5 and 2.6) in three areas within the brain: the olfactory bulb, the cerebellum and the pons, shown in figure 2.2 (a).

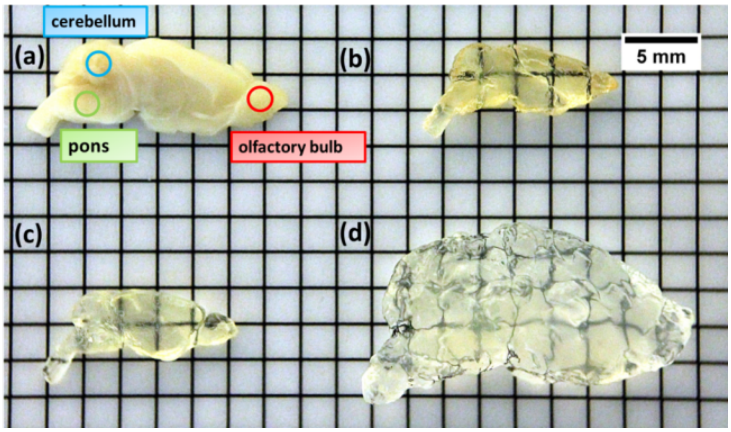

Figure 2.4: Images of cleared and uncleared mouse brain slices acquired with white light. These are representative slices and were used for the light attenuation quantitation measurements taken in the present research. Prior to optical clearing, the tissue was opaque (a). Optical clearing with (b) BABB, (c) pBABB, and (d) CLARITY significantly increased tissue transparency. The areas where spectroscopic light attenuation measurements were performed were the same in all slices; they are shown in (a). The images have the same spatial scale.

The system used for the measurements (Figures 2.5 and 2.6) consisted of a halogen lamp (HL-2000, Ocean Optics), coupled to a 200 μm optical fibre. Using a collimator, the light was collimated to a diameter of 3 mm. The cleared mouse brain

slices were sandwiched between cover slips so that their thickness was 2 mm, and were positioned vertically in a 3-D printed holder. The holder was designed with Inventor (Autodesk, San Rafael, California) and printed in acrylic. In the case of the CLARITY technique, the slices needed to be compressed due to the tissue expansion that resulted from clearing. To allow for different regions within the sample to be selectively illuminated by the beam, two x-y translation stages were attached to the holder.

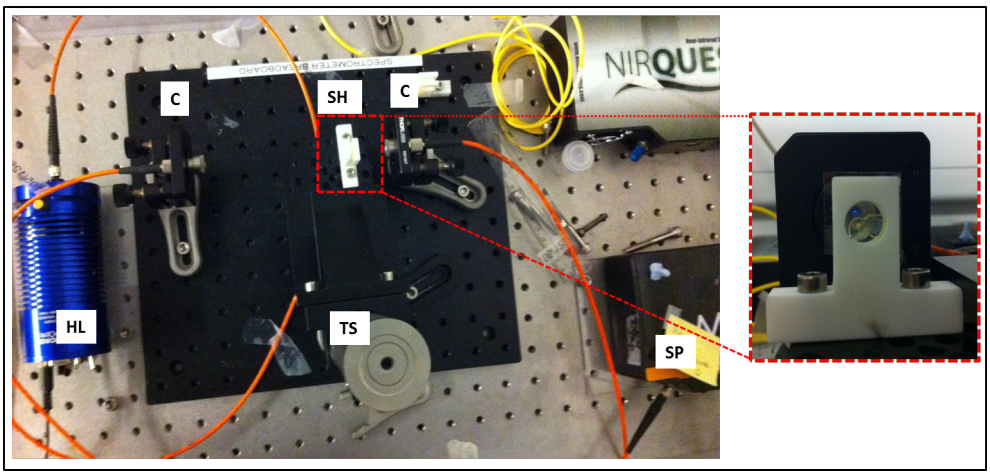

Figure 2.5: Photo of the custom spectroscopic system used for light attenuation measurements. The system and its components are explained in details in the next figure. On the right hand side, zoom in of a brain slice inserted in the 3-D printed sample holder for measurements.

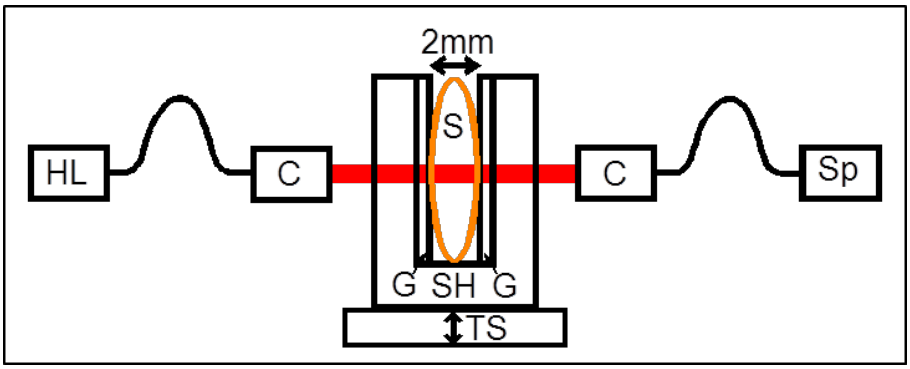

Figure 2.6: Simplified schematic diagram of the experimental setup used for spectroscopic light attenuation measurements. The light emitted by a halogen lamp (HL) was coupled to a 200 µm fibre and collimated with a collimator (C) to form a 3 mm-diameter beam that illuminated the sample. The cleared sample was sandwiched between two 200 µm glass cover slips (G) and placed in a custom-designed, 3-D printed sample holder (SH) with 2 mm spacing. To ensure that the light was aligned with a particular region of interest, two linear translation stages (TS) were attached to the holder. Transmittance spectra were collimated and acquired with a spectrometer (Sp).

Transmittance spectra in the range of 400 to 1100 nm were collimated and acquired with a spectrometer (Maya Pro; Ocean Optics, Dunedin, FL) using a program written in Labview (National Instruments, Austin, Texas) (Daniil Nikitichev, UCL Department of Medical Physics and Biomedical Engineering). The specific range from 400 to 1100 nm was chosen because of the interesting absorption and scattering bands of tissue components in this range, as seen in Chapter 1, and because it is within these wavelengths that most optical imaging techniques operate. Background spectra with no sample in the holder and reference spectra using only BABB were acquired separately. Transmittance spectra were acquired in three spatial locations within each region of interest to assess repeatability of the measurements. For each brain region, 100 spectra were acquired with the same exposure time (6 ms) and averaged.

Post-processing of the data, which included background subtraction and subsequent division by reference spectra, was performed with Matlab (Mathworks, Natick, MA). The attenuation of unscattered light was modelled using the Beer-Lambert Law. The attenuation coefficient μ_T (mm^{-1}) of each brain tissue slice with thickness *x* (mm) was estimated using the following equation:

$$\mu_T(\lambda) = -\frac{1}{x}\ln\left(\frac{I-I_b}{I_0-I_b}\right) \qquad \text{Eq. 2.1}$$

where I, I_0, and I_b are the spectra acquired with light transmission through the sample, through the reference solution (BABB), and through air in the absence of light, respectively.

2.2.6 Tissue volume changes

The clearing process often causes changes in tissue volume (56). In some cases, e.g. CLARITY, the tissue tends to expand. Other techniques, like clearing with BABB or Methyl Salicylate, induce shrinkage, most probably due to the dehydration step. Changes in tissue volume that resulted from clearing can be noticed in figure 2.4 and 2.7 and were here assessed by measuring variations in the cross-sectional areas of tissue slices before and after clearing, and extrapolating to three dimensions. Areas were measured by analysing tissue images with Image J (National Institutes of Health, Bethesda, Maryland).

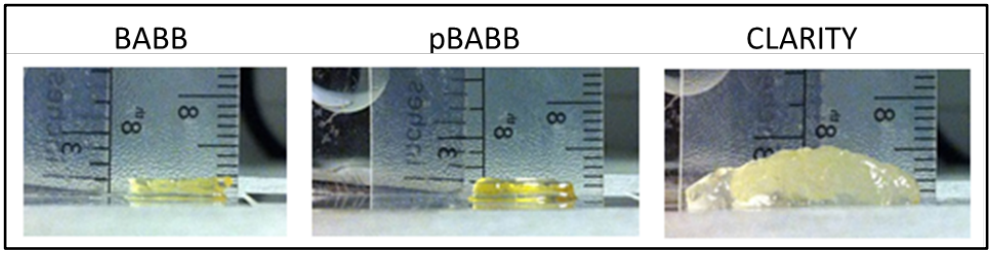

Figure 2.7: Photos of representative 2 mm brain slices (side view) cleared with the three examined techniques. The photos were acquired with white light. While BABB and pBABB cause tissue shrinkage, the slices cleared with CLARITY undergo swelling during clearing. Photos are on scale.

2.3 Results

2.3.1 Spectroscopic measurement of light attenuation μ_T (λ_{MAX})

Transmission spectra acquired in 12 brain samples showed that the efficacy of optical clearing varied depending on clearing technique and tissue region.

The spectrometer was first tested by measurement of light attenuation of deionized water. The values obtained were compared with the literature (123). In their study, Querry et al measured the spectrum of attenuation of light passing through deionized filtered water by the use of a split-pulse laser method. The range of μ_T relative to the attenuation of light in deionised water, illustrated in figure 2.8, is different from the range of relative to the attenuation of light in the brain samples: 0 to 0.05 for the former, 0 to 2 for the latter. Nevertheless, the spectrometer test is still reliable, as the cause of the attenuation range difference is the attenuation of water being considerably lower compared to the attenuation of biological tissue. Against this background, the values of light attenuation of water obtained in the present study were found to be consistent with the literature and sufficient to test the spectroscopic setup used for the measurements of light attenuation in tissue.

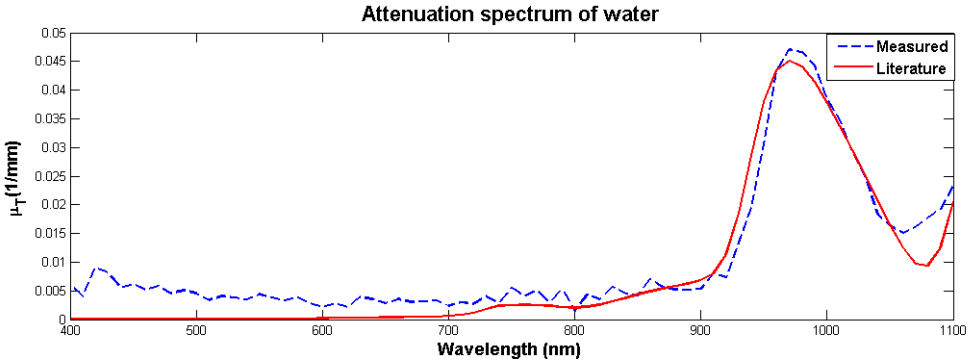

Figure 2.8: Light attenuation spectrum for deionized water. The blue curve represents the values obtained in the present study to test the spectrometer, which were compared with values from the literature (red curve).

The light attenuation spectra acquired in each brain area of the slices cleared with the three techniques are shown in figure 2.9.

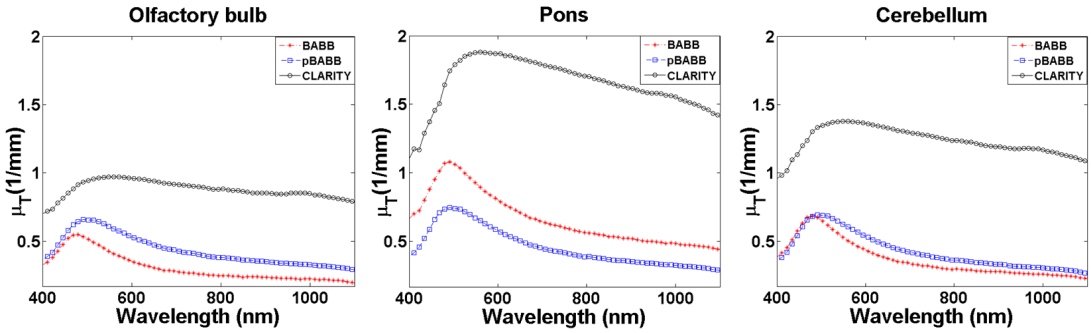

Figure 2.9: Light attenuation spectra obtained with the three clearing techniques in three brain regions, as calculated with Eq. 2.1 and averaged over all measured brains.

For all brain regions, samples that were cleared with pBABB and BABB resulted in lower attenuation coefficients than samples that were cleared with CLARITY. For example, for the cerebellum the mean attenuation coefficients, as calculated across the entire measured wavelength range, were 0.68 ± 0.29 mm^{-1} and 0.70 ± 0.09 mm^{-1} for BABB and pBABB, respectively, and they were 1.38 ± 0.22 mm^{-1} for CLARITY. Moreover, the maximum attenuation occurred at a higher wavelength for CLARITY than for BABB- and pBABB-cleared samples (Table 2.1). This might be related to different properties of the immersion media used for the last step of clearing (BABB and glycerol); for example, the refractive indices are dependent on the wavelength of light, and every solutions absorbs light at a certain wavelength and is permissive to light in a different part of the spectrum.

Region	Technique	λ_{MAX} (nm)	$\mu_T(\lambda_{MAX})$ (mm^{-1})
Olfactory bulb	BABB	476	0.55 ± 0.23
	pBABB	497	0.66 ± 0.12
	CLARITY	558	0.97 ± 0.11
Pons	BABB	487	1.09 ± 0.28
	pBABB	497	0.75 ± 0.10
	CLARITY	553	1.89 ± 0.19
Cerebellum	BABB	482	0.68 ± 0.29
	pBABB	497	0.70 ± 0.09
	CLARITY	549	1.38 ± 0.22

Table 2.1: Light attenuation in mouse brains cleared with three different techniques. The wavelength for which the attenuation coefficient was a maximum, λ_{MAX}, varied with brain region and clearing technique, as did the corresponding attenuation coefficients, $\mu_T(\lambda_{MAX})$ (mean ± standard deviation).

Figure 2.10 shows the light attenuation spectra of the clearing solutions. These are BABB, used for BABB and pBABB clearing, and glycerol, used for the samples cleared with CLARITY. Compared to the values of light attenuation relative to the brain tissue, the light attenuation spectra of BABB and glycerol are noticeably lower, hence can be considered negligible in the overall light attenuation measured in the brain samples and showed in Figure 2.9.

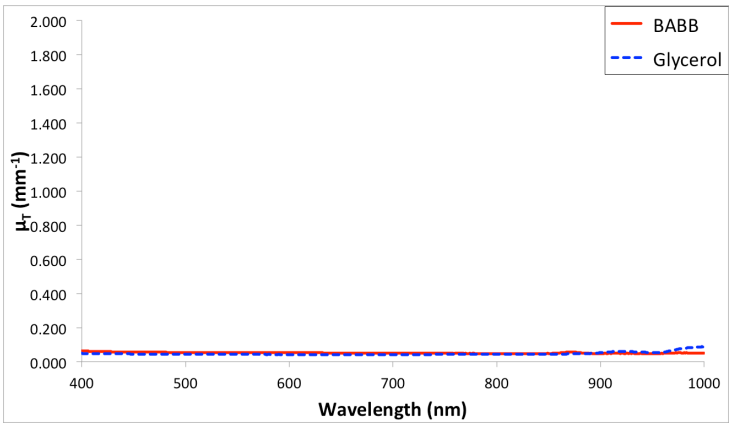

Figure 2.10: Light attenuation spectra for the clearing solutions. The spectra were measured with the spectrometer used in the study. The red curve represents the values obtained for BABB, while the blue dashed curve represents the attenuation of light in glycerol.

2.3.2 Brain volume changes

Each of the clearing techniques under investigation induced tissue volume changes (Table 2.2). Both BABB and pBABB resulted in reductions in tissue volume (52% and 50%) due to water loss, which is common for solvent-based clearing techniques (59). In contrast, the CLARITY resulted in volume increases (252%), caused by hydrogel infusion during embedding.

Condition	**Technique**	**Volume (mm^3)**	**Volume change (%)**
Before clearing		156	--
After clearing	BABB	81	52
	pBABB	79	50
	CLARITY	394	252

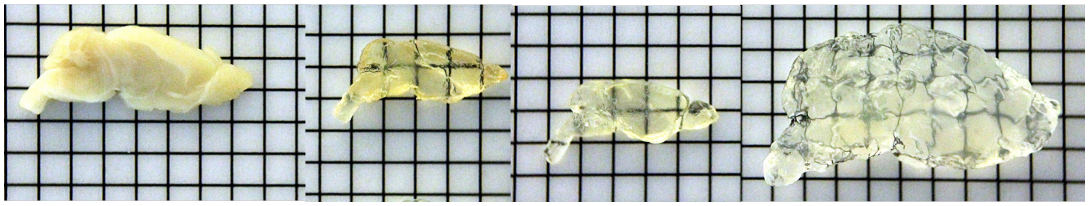

Table 2.2: Volume of the brain slices before and after optical clearing, which was performed with the three compared techniques: BABB, pBABB and CLARITY. The data refer to one slice per each technique but are representative of all the cleared samples. The measured slices are showed below the table. These represent, from left to right: uncleared slice, slices cleared with BABB, pBABB and CLARITY.

2.4 Discussion

The data presented in this study show that light attenuation in cleared brain tissue was greatest in samples cleared with passive CLARITY, and lowest in those cleared with pBABB or BABB. The shape of the attenuation spectra was different for pBABB/BABB and CLARITY-cleared samples, with the latter producing a wider spectrum with a peak and extended tail at higher wavelengths as compared with those produced with pBABB/BABB. The origin of these spectral differences is still unclear. The significantly lower absorption by BABB samples at higher wavelengths (>600 nm) could perhaps be exploited for the optimization of imaging of fluorophores with emission at such wavelengths.

Structural tissue modifications such as dehydration or lipid extraction lead to tissue swelling or shrinkage. Evaluation of the change in size of brain samples was assessed from tissue cross-sectional volumes before and after clearing. Measurements showed a decrease in size with BABB and pBABB clearing (52% and 50%, respectively), most likely caused by the dehydration step, and a large increase in size was found with passive CLARITY (252%). Regarding the swelling cause by the CLARITY protocol, care is needed in the hydrogel preparation step and in the incubation temperature of the sample for hydrogel polymerization (37 °C). Both of the size changes caused by the examined techniques could be confounding factors in morphological studies, and should be taken into account when choosing a clearing approach for a particular application.

The regions where light attenuation was measured were chosen because they are known to have different tissue morphologies and lipid content. As different organs reach a different degree of clearing when treated with the same OCAs, this is also useful for comparing different areas within an organ. For example, the Sca*l*e technique (66) cannot fully clear the white matter of the brain because the lipid-rich myelin structures of the white matter have a considerably higher refractive index (n=1.4102) than the solution used for clearing (n~1.382), which is instead close to the refractive index of the grey matter (n=1.395) (124). Methods that use clearing solution with refractive indices close to the one of lipids, such as SeeDB (65), where

the clearing solution contains a high percentage of fructose (n~1.49), are more effective at clearing both grey and white matter. These are the main components of the central nervous system and differ in the amount of myelin they consist of. Myelin is a lipid-based substance that contributes significantly to optical scattering (125, 126). While grey matter, mainly present in brainstem and cerebellum, as well as throughout the spinal cord, contains numerous cell bodies and few myelinated axons, white matter is manly composed of highly myelinated axon tracts. The high concentration of myelin gives the white matter a white colour, hence its name, while the grey matter appears more light grey (127).

Of the three brain regions investigated, the pons showed the lowest clearing efficacy, most likely due to its greater white matter density. White matter contains large quantities of myelin, which contributes significantly to optical scattering due to its high concentration of lipids. In this study, a new clearing technique called pBABB was also investigated, in which hydrogen peroxide is added to the dehydration medium. This step is beneficial as it enables the bleaching of endogenous tissue pigments, thereby reducing autofluorescence. Moreover, DMSO acts as a solvent increasing the clearing solution penetration without damaging the tissue (60). Due to its low toxicity, it has been used not only as a penetration enhancer but also as a simple clearing agent without the addition of any other OPC, and it has been used for *ex vivo* as well as *in vitro* and *in vivo* optical clearing (128). The clearing methodology we have developed is also particularly advantageous as it is straightforward and inexpensive, and clearing times are considerably shorter when compared to techniques such as CLARITY. However, BABB, as with most of the techniques that make use of organic solvents for refractive index matching, has the main disadvantage of decreasing the half-life of the fluorescent signal (126), most probably due to peroxide contamination (47). Despite the highest degree of tissue clearing which can be obtained with pBABB, this approach is only applicable to autofluorescence studies to look at tissue morphology, due to the bleaching step with hydrogen peroxide. Conversely, the CLARITY protocol produces minimal protein loss and preserves native fluorescence (69).

2.5 Conclusion

This study demonstrated a novel method to quantify the efficacy of optical clearing protocols, which aim at deeper tissue imaging and were widely investigated and used in the experiments of this thesis. Furthermore, a new method for tissue optical clearing was developed in this thesis and named pBABB. This is a modification of the established BABB approach and can be used for morphological analysis of tissue samples.

Assessing the degree of transparency achieved with different optical clearing approaches is an essential step in the process of choosing a clearing approach for a specific application and in the stage of imaging data evaluation. The results of this study showed that the degree of clearing obtained with pBABB and BABB methodology is greater than that given by CLARITY, and that differences exist in the shape of absorption spectra, particularly at wavelengths greater than 600 nm. It has also been shown that the level of optical clearing varies within the brain, most likely due to the structure and composition of each particular area.

The study focussed on three optical clearing techniques and on optical clearing of brain but could easily be applied to any other method or tissue, such as different organs or tumours. This work could help guide the choice of the most suitable optical clearing method for a specific application. It could be useful to optimize the choice of wavelengths for optical imaging techniques. For instance, the lower attenuation by pBABB/BABB-cleared samples at higher wavelengths (>600 nm) could be beneficial for imaging of fluorophores with emission in the far visible range, such as AlexaFluor 647. Furthermore, assessing the transparency of a tissue is particularly important when imaging cleared samples with systems widely used in this thesis such as optical projection tomography and light sheet fluorescence microscopy, as reduced light scattering can lead to higher spatial resolution and greater contrast (129).

In this study, the degree of optical clearing measured by spectroscopy could also be assessed visually (Figure 2.4), with differences in colour evident between clearing

techniques. A clear difference in size after clearing can also be observed. Indeed, as mentioned in Chapter 1, most optical clearing techniques cause swelling or shrinkage of the sample.

The present study is very relevant in the field of optical clearing. In fact, to date there is no method to quantify and objectively compare the degree of transparency achieved with different optical clearing approaches. Indeed, in the original papers which describe optical clearing techniques, such as 3Disco (57) and CLARITY (69), the protocols are described and images of cleared samples are shown, but no reference to quantitative comparison with previous approaches is mentioned.

The light attenuation quantitation is also particularly important for the present work since optical clearing constitutes the basis of this PhD work, as it is a process that was used to prepare samples for different investigations, such as analysis of perfusion in liver metastases, investigation of vascular networks in colorectal carcinomas and effect of vascular disrupting agents on the vascular architecture.

Chapter 3: Development of methods for three-dimensional visualization of tumour vascular networks

In contrast to normal tissues, tumours are characterized by a highly irregular vascular network (130), which leads to heterogeneous distribution of blood, oxygen and other nutrients, resulting in the creation of hypoxic or necrotic regions within the tumour (113, 131). This, coupled with associated changes in interstitial fluid pressure can negatively affect the delivery of drugs, radiation therapy and targeted chemotherapy (132). However, these phenomena can vary significantly both within and between tumours. Mathematical simulations of blood flow and drug delivery at the whole-tumour level could provide significant benefit in the development and optimization of new therapies.

Conventional microscopy and histology are the most commonly employed techniques to analyse the vasculature of healthy organs and tumours. However, processes like tumour angiogenesis and drug delivery are complex and three-dimensional, and much could be lost with approaches that are intrinsically two-dimensional, or that have limited spatial coverage (113). In this chapter, existing approaches for studying healthy and diseased vascular networks are compared with novel optical methods, including optical clearing and optical projection tomography.

Two different approaches for vasculature network labelling were examined: perfusion with radiopaque polymer injection media (vascular casting) and vasculature labelling with fluorescently labelled antibodies. These two methods are compared in this chapter, where advantages as well as limitations of both are highlighted. This was in order to choose the most appropriate imaging technique for the applications described in Chapter 4.

3.1 Introduction: imaging techniques for vasculature analysis

Vascular networks within living organisms are complex and challenging to analyse. The network structure of the vasculature has a significant bearing on its ability to deliver blood to a tissue, and so imaging vascular network structure allows information to be inferred about its development, connectivity and perfusion distribution (133). Over the past 30 years there has been a remarkable rise in medical imaging, computational and numerical techniques that allow the physiology of normal and diseased tissue to be extrapolated. Improving the understanding of normal physiological function (134) and studying vasculature also helps understand pathological conditions such as atherosclerosis (135), tumour perfusion (136) and cardiac disease (137). These types of studies have also enabled advances in the fields of experimental physiology and imaging (133).

A range of *in vivo* imaging techniques has been developed for imaging vascular structure in three-dimensions, including magnetic resonance angiography, X-ray CT and fluorescence molecular tomography. These techniques have the advantages of being non-invasive and allowing high depth penetration, which makes it possible to study the progression of diseases such as cancer. However, they are limited by low spatial resolution, hence cannot resolve vessels at the capillary level but only assess major vessels such as arteries and veins (> 50 μm (138)). Indeed, to directly resolve the entire blood vessel network, image resolution must be less than the diameter of a capillary (~5-10 μm (139, 140)). This limitation can be overcome by intravital microscopy in living animals. Intravital confocal and 2P microscopy allow spatial resolution of 500 nm, hence are suitable for real-time observation of *in vivo* events down to subcellular resolution (113). Despite the high resolution these methods are limited by their small field of view and reduced tissue imaging depth (generally no higher than 1 mm), hence are not suitable for imaging vasculature in entire organs or tumours (112).

X-ray CT (from hereon referred to simply as CT) is also used to image the vascular network. CT has the main advantaged of being able to acquire *in vivo* images, hence it makes it possible to study the progression of diseases such as cancer. μCT is a

variant of CT, optimised for imaging small samples at high resolution, is generally used for *ex vivo* imaging, in which case there is no radiation exposure limit.

As with μCT, scanning electron microscopy (SEM), pioneered in the early 70s by Murakami (141), has been used for analysis of vascular casts from different tumour models (142) and organs (143). Both μCT and SEM entail the formation of a vascular cast through perfusion of radiopaque polymerizing resins. SEM produces high resolution images (on the scale of 1 nm) of a sample by scanning through it with a high-energy focussed electron beam. Whilst the scanning resolution of SEM is higher than μCT (144), the sample preparation for SEM imaging requires filling the vessels first and then maceration of the soft tissue around them with a concentrated base or acid in a process called vascular corrosion casting (145). This procedure therefore requires strong and non-brittle casting agents, able to maintain the vascular structure after removal of surrounding supporting tissue (146). So despite allowing analysis of the vascular bed down to the capillary level, the information on the spatial relation between the casting agent filled vessels and the morphology of the tissue surrounding them is lost in this kind of technique.

Whilst SEM has been used to study tumour vasculature through the analysis of vascular corrosion casts, it is ideal for evaluating vessel surface detail but not to analyse the topology of vascular networks (142). For a more detailed structural analysis a 3-D method such as μCT is needed. Indeed, μCT is an inherently 3-D technique, in which multiple raw projections of the sample acquired during a whole rotation are reconstructed to form a 3-D image, which makes it ideal to study the vascular network. μCT can be used in combination with corrosion casting or also with compounds that contain a radiopaque polymer, which allows surrounding tissue to remain intact, such as Microfil.

Silicone polymer injection media have been used for over 40 years to visualize vasculature by tissue clearance and light microscopy. For example, in their study of atherosclerosis Barger et al used cinematographic recording of polymer medium injections into cleared human hearts to demonstrate neovascularization in and around plaques in the coronary artery (147). Only recently, radiopaque perfusion compounds have been used in conjugation with μCT. Microfil contrast agent (Flow Tech, Inc.

Carver, MA) is a low viscous silicon rubber injection compound containing lead pigments, and has been used together with μCT to image and quantify systemic mouse vasculature (148). Microfil perfuses the lumen of the vessels, and its lead pigments due to their high X-ray absorption properties, compared to the background tissue, provide the contrast needed to acquire 3-D images of the vascular network, at high resolution.

Post-mortem perfusion protocols for *ex vivo* imaging techniques such as vascular casting, in combination with μCT, allow the injection of a polymer into the specimen, which is not possible in live animals. These approaches also overcome the main disadvantages of live-animal specimen imaging, such as excessive radiation exposure, motion artefacts due to movements of live animals and long image acquisition times. However, *ex vivo* imaging offers only a single timepoint to be investigated.

Other approaches to analyse the mouse vasculature are optical imaging techniques that can make use of fluorescent compounds, which include OPT and ultramicroscopy, discussed in Chapter 1. There are a vast number of fluorescent compounds useful for imaging vessel structure and function. For example, nuclear dyes that intercalate with DNA, such as DAPI (4',6-diamidino-2-phenylindole), propidium iodide or Hoescht 33342, are useful for studying the organization and relationship between the different types of cells in the vascular wall (149). An antigen widely used as a molecular marker for mature endothelial cells is platelet-endothelial cell adhesion molecule (PECAM1, or CD31) (150). PECAM1 has the distinctive feature of being expressed on several of the major cell types associated with the vascular compartment (151), and it proved to be a very reliable marker for angiogenesis (152). Although several other vessel wall antigens have been used as vessel markers, many of these mark vessels in physiological conditions but are not necessarily expressed in cancerous tissue (153).

Visualization of blood vessels can also be done with fluorescently labelled lectins, specific carbohydrate-binding proteins which can label both normal and tumoural blood microvessels. In this thesis three different fluorescent compounds for vasculature labelling were tested. These are discussed and compared in section 3.6,

thereafter the most suitable compound is highlighted and the methods for *in vivo* labelling are illustrated.

3.2 Comparison of μCT and OPT for imaging complete blood vessel networks

The physical processes underpinning μCT and OPT is essentially the same, with the main difference being the wavelength of electromagnetic radiation used to probe the sample: μCT uses X-rays while OPT works with visible light. When compared to μCT, OPT suffers one technical drawback, typical of optical imaging systems: with only a limited depth of focus, which cannot incorporate the whole sample. Hence, while in μCT the shape of the projections can be approximated as long cylinders / beams which have cross-sections that are constant throughout their entire path, in OPT these cross-sections vary: they are thin near the focal plane and larger towards the ends (Figure 3.1).

To reduce this drawback, the focal plane in OPT is positioned halfway between the axis of rotation and the edge of the specimen that is close to the objective lens. However, this results in focussed data from the front half of the sample as well as out of focus data from the back part to be contained in every image. The back-projection algorithm is slightly modified to take this into account, and the modification relates on the depth of field (Figure 3.2).

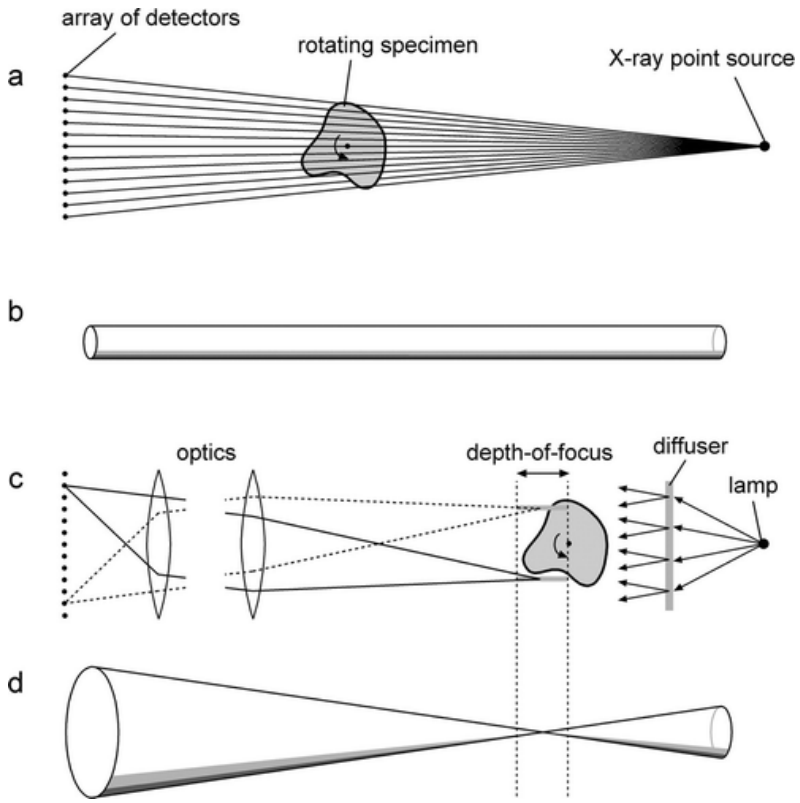

Figure 3.1: Comparison between standard X-ray computed tomography and optical projection tomography. a) In a typical tomograph each projection is a straight line between the point source and the detectors. b) In OPT the focal plane is positioned such that the depth of focus covers the half of the sample which is closer to the optics (dashed vertical lines). The image was adapted from ref. (76).

In μCT, and generally in standard tomography, the algorithm back-projects the measurements acquired across the whole image (Figure 3.2 b). A different approach, that limits the back-projection to the area which corresponds to the focussed part of the sample, helps improving the quality of the image (76). The data is registered for the various angles through a complete rotation of the sample and a semidisk mask, part of the algorithm, is rotated to back-project only focussed data (Figure 3.2 d).

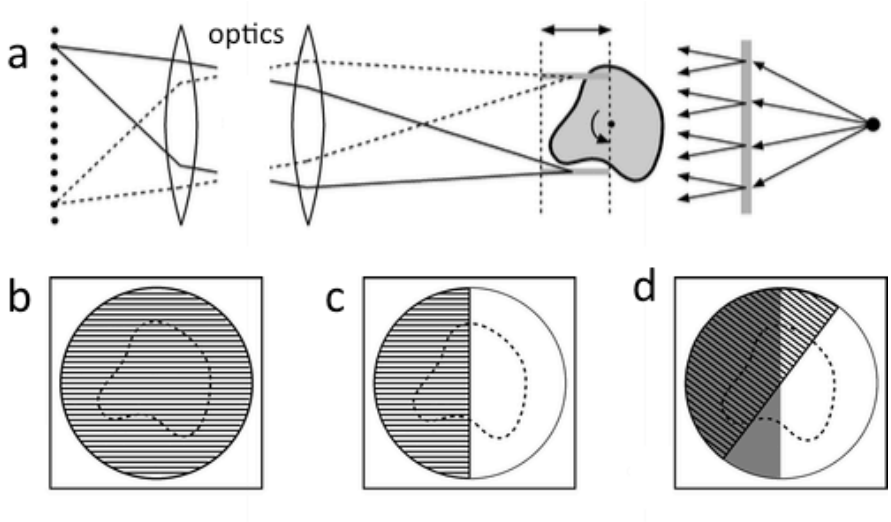

Figure 3.2: Standard and modified back-projection algorithms. a) In OPT, only the part of the specimen that is closer to the optics is in focus. b) Standard back-projection algorithm. The data is back-projected across the whole image. c) Modified back-projection algorithm, where the back-projection is limited to the region corresponding to the focussed half of the specimen. d) Modified back-projection algorithm. The data for successive orientations is collected and the semidisc mask is rotated to maintain the back-projection in the correct region of the image. The image was adapted from ref. (76).

Despite the biggest drawback of OPT being the necessity to optically clear the sample, OPT was more suitable for the applications presented in this research, as it discussed in the next few sections. Indeed, the main limitation of μCT relates to its contrast: X-rays are hardly absorbed by soft tissue and optical coloured stains (154). This makes it difficult to image both tissue morphology and fluorophores used to stain specific proteins or labelled structures within the tissue. Contrast for μCT can be enhanced through the use of highly absorbing polymers. However, these resins present various limitations (section 3.4). Furthermore, the spatial resolution of conventional μCT, around 12-50 μm (96), is not sufficient to visualize small structures such as the vascular network within a tumour.

3.2.1 Study design

This study aimed to compare different vasculature labelling methods (fluorescence and radiopaque resins) and different *ex vivo* imaging techniques (μCT and OPT) to analyse vascular networks in mouse organs and tumours. The final purpose was to identify the most suited approach for studying the irregular vasculature of colorectal

tumours and to compare treated and untreated tumour tissues, as shown in the next chapter (Chapter 4).

The first approach used for labelling blood vessels was vascular casting with radiopaque silicone polymer medium (Microfil). The vasculature of Microfil-perfused whole mouse brains was imaged with μCT, then optically cleared and analysed with OPT. The comparison of these two imaging techniques is novel, especially for the study of vascular networks.

The second tested approach for looking at vascular structures made use of fluorescently labelled lectins. Three compounds with different fluorescence properties were used for investigation: lectin-FITC, lectin-TRITC, lectin-AlexaFluor 647. This thesis shows the results of fluorescent vasculature labelling in brain, heart and colorectal tumour tissues, optically cleared and imaged with OPT.

3.2.2 Microfil perfusion: introduction and background

Savai *et al*. used Microfil in combination with μCT to image and quantitatively evaluate lung tumour angiogenesis and reduction after bevacizumab treatment in mice (155). The same technique has been used by Chugh et al (156) to generate cerebral blood volume maps of the mouse, an application that is of particular interest for characterizing cerebral vascular disease phenotypes. Daneyemez investigated the acute changes due to cerebral contusion in the large vessels and microvasculature in the rat, and used Microfil perfusion to study the damage of the superficial arteries and their arterial branches (157). Microfil has also been used to assess placental vascular growth in late gestation, at different time points. The authors were able to create 3-D data set of the feto-placental vascular bed, which was useful for analysing the feto-placental circulation of the mouse during normal development but also to evaluate defects in genetically altered mice (158). However, they report that a great number of procedures failed. Indeed, 87 of 176 placentas were rejected prior to imaging due to inadequate or inappropriate filling. The main issues were related to unperfused segments of placenta and vessel ruptures, which caused Microfil leakage.

Other potential sources of error which cause discontinuities in the Microfil filling comprise a) nonphysiological filling pressure, b) choice of polymer dilution to arrive at the desired viscosity for adequate filling of small vessels and c) the possible inclusion of air bubbles in the casting resin. Bubbles can be reduced by fully immersing the angiocatheter used to cannulate the aorta in water when switching from saline to Microfil. Discontinuities in Microfil (asterisks in figure 3.3, B) are mainly induced by the hydrophobic nature of Microfil: discontinuities caused by water can occur and produce casting breaks within the vessels. These breaks can be reduced by adjusting the pressure of the infusion (159). The correct combination of perfusion pressure and Microfil dilution is challenging to achieve, and it can vary between organs (160, 161). Indeed, too low perfusion pressure can cause incomplete filling, as the Microfil will not be pushed into all the vascular bed and capillary networks (Figure 3.3 C). Conversely, too high pressure can cause vessels and especially capillaries to burst, causing discontinuities and Microfil leakage in the surrounding tissue (Figure 3.3 D). Additional concerns are possible effects of energy dissipation during the exothermic polymerization reaction and cast shrinkage.

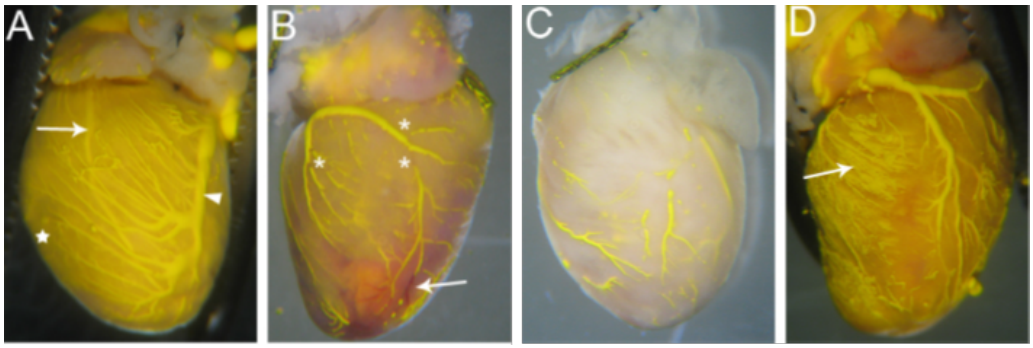

Figure 3.3: Adult mouse heart perfused with Microfil casting agent, adapted from ref. (159). A) A well-perfused heart. The arrow and the arrowhead show visible arteries and veins, respectively. B) Example of discontinuities in Microfil (stars) and blockage due to incomplete heparin perfusion. C) Too low perfusion pressure can cause incomplete filling of vessels. D) Too high pressure results in vascular disrupture and Microfil leakage in the surrounding tissue (arrow).

3.2.3 Methods

Microfil perfusion

After confirmation of anaesthesia, mice were perfused-fixed as illustrated in section 2.2.3. For this procedure, perfusion was performed with saline followed directly by perfusion with Microfil casting solution instead of PFA. Microfil (Flow Tech, Inc. Carver, MA) was prepared according to the manufacturer's protocol: 2 ml of pigmented (yellow) compound was mixed with 5 ml diluent and 225 µl curing agent. Due to the viscosity of the casting solution, which is greater than that of blood (162), the perfusion flow rate was adjusted from 3 ml/min used for saline perfusion to 2 ml/min when administering Microfil to minimize vessel rupture. The polymerization of Microfil was initiated at 20 minutes after the addition of the curing agent. To avoid incomplete vessel filling (in order to minimize discontinuities and air bubbles in the casting solution), the angiocatheter was fully submerged in water when switching from saline to Microfil. Since catalysed mixtures form an elastomeric gel after 90 minutes at room temperature, after perfusion the sample was covered with wet gauze and left for 1.5 hour. It was then placed in a bath of 4% formaldehyde solution and left overnight. Individually harvested brains were post-fixed in 4% formaldehyde for 12 hours. After fixation, the specimens were rinsed three times with PBS (10 minutes each time) to allow removal of formaldehyde residues.

3.2.4 3-D imaging of vascular networks

In the present study, two *ex vivo* imaging techniques for vasculature analysis of whole organs labelled with radiopaque vascular casting resins were compared: µCT and OPT. Some acquisition parameters relative to the µCT and OPT systems used in this research are specified in Table 3.1.

Acquisition parameter	µCT	OPT
Rotation step	0.9 degree full step	0.9 degree full step
Camera pixel size	1 µm	6.45 µm x 6.45 µm
Camera resolution	1000 × 575 to 8000 × 2300 pixels	1024x1024 or 512x512 square pixels
Magnification of tomograph on the camera	FOV 35x35 mm	FOV 4x4 mm- 20x20 mm

Table 3.1: Acquisition parameters of the µCT and OPT systems used in this research.

3.2.4.1 Micro-CT imaging

Brains perfused with Microfil casting solutions were first imaged with a high resolution µCT scanner (Skyscan1172, Bruker, Massachusetts, USA), courtesy of Prof. Tim Arnett (UCL, Department of Cell and Developmental Biology). Images were acquired over 360° at rotation steps of 0.2 degrees. Exposure was set to 590 ms per frame for all the brains scanned. Source voltage and current values were 49 kV and 200 µA. A complete dataset was acquired in 40 minutes.

The 1021 TIFF files obtained were reconstructed with Nrecon software 1.6.6.0 (SkyScan, Belgium). The reconstruction duration was 1.48 s per slice, ring artefact correction was set to the value of 6 and image pixel size was 8.265 µm.

3.2.4.2 OPT imaging

After µ-CT imaging, brains perfused with Microfil casting solution were optically cleared for imaging with transmission optical projection tomography: the first step was embedding in 1% low melting point (LMP) ultrapure agarose (Invitrogen). The agarose solution (gelling point 24-28 °C) was made with deionized water. It was warmed to 60 °C then filtered through filter paper (Whatman 113V). The agar was then placed in an incubator at 32 °C to avoid tissue damage during the embedding procedure. When cooled to 32 °C, the samples were embedded using a syringe with adequate diameter and stored overnight at 4% for the agar to set. It is important that the samples are in a vertical position and at the centre of the syringe to maximize the quality of imaging by reducing light diffraction and refraction at the interface between the agarose block and the sample. After optical clearing, achieved as

described in section 2.2.4.1, the samples were ready to be imaged with OPT. Eight hundred projections were recorded in high resolution (1024x1024 square pixels) over 360° on a cooled CCD camera. Images were acquired with white light with transmission OPT in absence of fluorescence, using the optical contrast coming from the yellow pigment in the Microfil. Scan times were 30-40 minutes. File sizes ranged from 1.5 GB to 2 GB. Image reconstruction was performed with standard back-projection (Nrecon software, SkyScan, Belgium). File sizes ranged from 2 GB to 2.5 GB.

3.2.5 Results and discussion

The vasculature of a whole unsectioned brain labelled with Microfil and imaged with OPT and μCT is shown in figure 3.4. Both imaging techniques permit high-resolution, 3-D *ex vivo* imaging of the vascular network of entire organs at resolutions up to ~3 μm (142) as opposed to imaging the vasculature of excised tissue samples from limited regions of interest. The vascular casting technique presents several sources of error, such as non-physiological filling pressure, choice of polymer dilution to arrive at the optimal viscosity for adequate filling of the vasculature including small vessels, and possible inclusion of air bubbles in the casting resin. These drawbacks result in incomplete filling of the vascular bed and vessel rupture with resulting Microfil leakage, which can be appreciated mainly in the μCT images (Figure 3.4, red arrows). The level of optical clearing achieved in the brains imaged with OPT was high enough to acquire high resolution images of the vascular brain, except for the pons, where poor optical clearing interferes with the detection of blood vessels (Figure 3.4 b, yellow arrow). This is in accordance with previous studies on light attenuation quantitation in the mouse brain after optical clearing (Chapter 2), which show that the area of the brain where light is mostly absorbed is the pons (163).

As it can be seen from figure 3.4, OPT proved to be superior for imaging vascular architecture. The density of blood vessels looks much lower in the μCT images compared to the ones acquired with OPT: some major vessels that can be identified in the OPT images, such as arteries perfusing the region close to the olfactory bulb are completely or partially missing in the images acquired with μCT (Figure 3.4 c,

d). This difference in the images of the two samples is not likely to be caused by underlying physiological differences, as the images show the same sample. Also, missing are some major arteries in the brain, which if real would have led the animal to premature death. Furthermore, the preparation was consistent among all samples, hence the variations between the samples are very unlikely to be caused by the perfusion protocol.

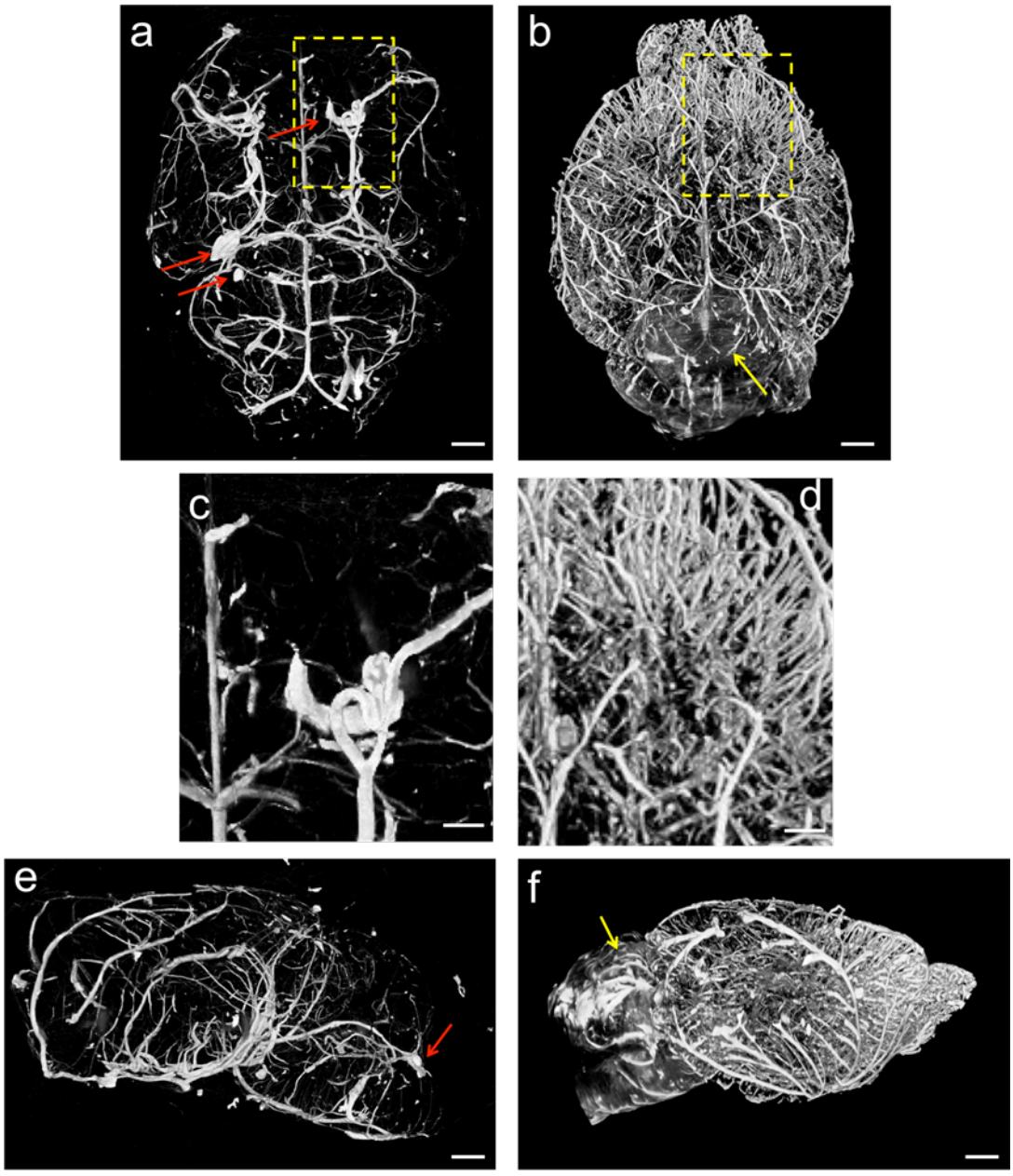

Figure 3.4: Vascular network of whole mouse brain. Prior to imaging, the vasculature was perfused with radiopaque polymer injection medium and the excised sample was optically cleared with BABB for OPT imaging. a, c, e) μCT images. a) Brain front view. The red

arrows point at Microfil leakage and accumulation in the tissue surrounding the blood vessels. c) Blow up image. e) Brain lateral view. b, d, f) OPT images. b) Brain frontal view. The yellow arrow point at the cerebellum, characterized by lower degree of optical clearing compared to the rest of the brain. d) Blow up image. Compared to image c, acquired with μCT, in this image high density of blood vessels can be appreciated. f) Brain lateral view. 10 μm isotropic resolution. Scale bar, 500 μm, blow up, 150 μm.

Limitations of the vascular casting technique, discussed in section 3.4, can be appreciated in Figure 3.5. The figure shows OPT images, acquired for this thesis, of vascular casting performed with Microfil in mouse heart (a,b), liver (c,d), and xenograft subcutaneous colorectal tumour (e,f). Blue circles indicate air bubbles within the heart. Microfil leakage after disrupture of vessels due to high perfusion pressure is indicated by yellow arrows. Red arrows point at discontinuities in Microfil due to low perfusion pressure.

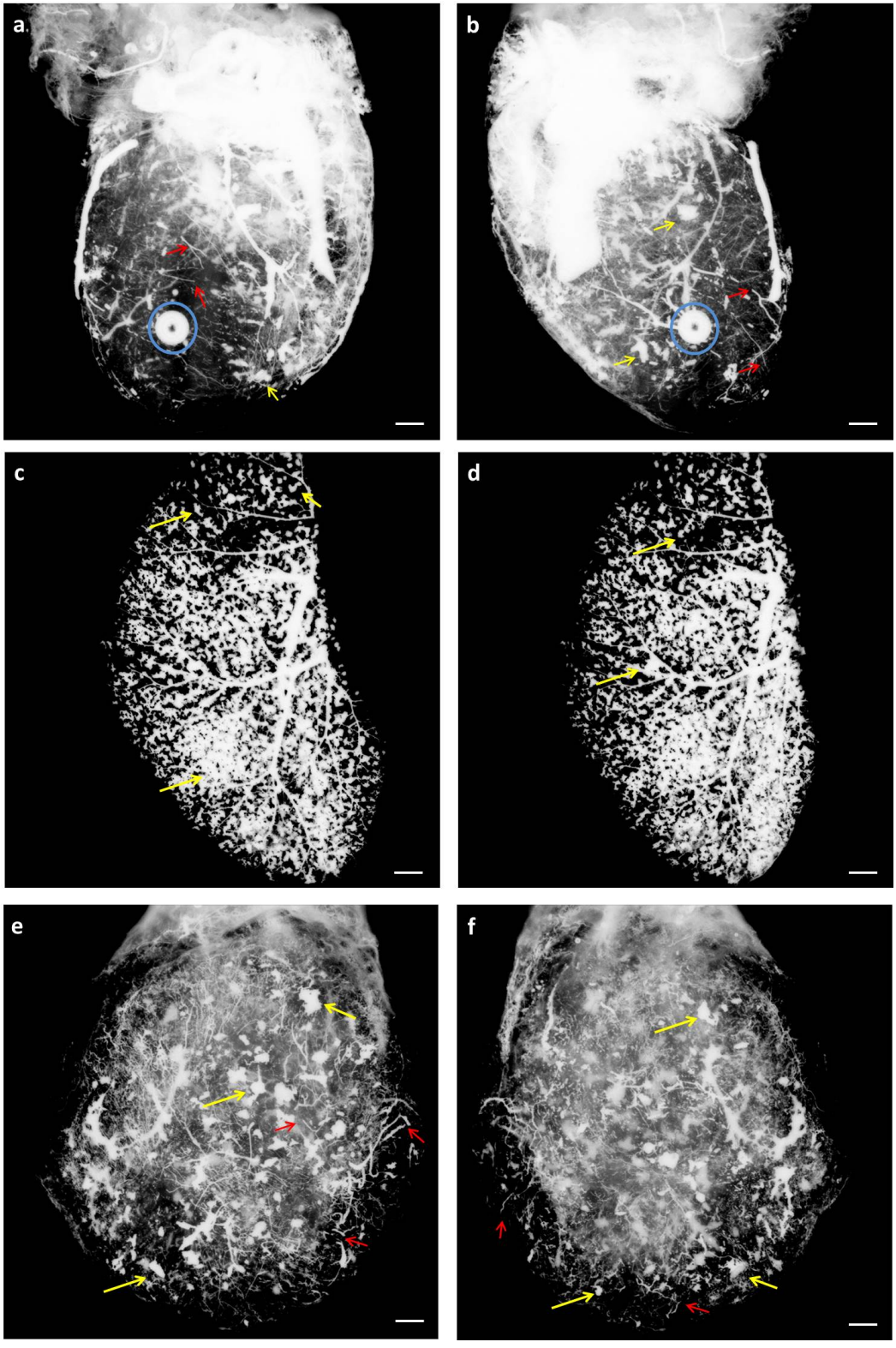

Figure 3.5: OPT projections images of various mice organs where vessels were labelled with the vascular casting technique. Yellow arrows point at vascular disrupture and Microfil leakage in the surrounding tissue. Red arrows indicate discontinuities in Microfil due to incomplete perfusion. a,b) Heart. Blue circles indicate air bubbles within the heart. c,d) Liver. e,f) Xenograft subcutaneous colorectal tumour. The pair of images indicates projections of the same sample at two different angles. Scale bars, 500 µm.

With the aid of computerized image analysis, multiple single-segment parameters and aggregate vessel statistics were calculated for the brains, and the dataset acquired with OPT and μCT were compared. The resulting measurements are shown in the following table (Table 3.2).

	Brain 1 μCT	**Brain 1 OPT**	**Brain 2 μCT**	**Brain 2 OPT**
Mean branch radius (μm)	36.09 ± 0.22	44.81 ± 0.15	38.57 ± 0.50	49.67 ± 0.12
Mean branch length (μm)	394.27 ± 2.62	535.27 ± 2.36	448.36 ± 7.313	581.29 ± 1.88
Mean branch angle (degrees)	77.63 ± 0.43	84.01 ± 0.35	77.03 ± 0.98	78.74 ± 0.24
Mean branch radius ratio (arbitrary unit)	0.62 ± 0.004	0.63 ± 0.003	0.62 ± 0.008	0.69 ± 0.002
Mean branch length ratio (arbitrary unit)	1.85 ± 0.05	1.59 ± 0.02	1.82 ± 0.26	1.742 ± 0.02

Table 3.2: Vessel parameters relative to dataset acquired with μCT and OPT in two different brain samples, labelled with the vascular casting technique.

The values of mean branch radius ratio and length describe the relationship between the sizes of a vessel at a branching point. For instance, the value of mean branch radius ratio for brain 1 measured with μCT was 0.62 ± 0.004, meaning that in this brain on average the branches were 0.62 ± 0.004 times smaller than the main vessel from which they separated. The mean branch length relative to the dataset acquired with OPT resulted to be slightly higher than those of vessels measured with μCT. This could be due to quality of the OPT images, thought to represent the real brain anatomy with higher detail.

3.3 Lectin perfusion: introduction and background

Lectins are proteins that specifically bind to sugar complexes in either glycolipids or glycoproteins (sugars attached to proteins or lipids), especially on the luminal and/or

abluminal surface of vessels (164, 165). Although lectins usually contain two or more binding sites for carbohydrate units, some lectins form oligomeric structures with multiple binding sites. The binding sites of lectins on the surface of one cell interact with arrays of carbohydrates located on the surface of another cell.

Lectins are generally bound to tissues of interest via intravascular perfusion rather than *ex vivo* on tissue sections. Indeed, post-fixation of slices can alter the morphology and conformation of binding sites. Also, when applied on sections lectin can interact with components of the basement membrane, as sectioning exposes both surfaces of the endothelium (166). These proteins are proven tools for extensive visualization of the vascular bed in several animal species and in different organs, and in the past decade they have become especially important as markers for microvascular labelling.

3.4 Lectin perfusion: methods

The second part of the present study aimed at testing different lectin compounds for vasculature labelling. The first tested ligand was lectin *lycopersicon esculentum* (LE) from tomato conjugated with fluorescein isothiocyanate (FITC). This lectin binds primarily to the luminal plasmalemma in the microvascular beds (167). The fluorescent reagent FITC is a derivative of fluorescein widely used in biological research. It is characterized by a relatively broad fluorescence emission spectrum, with excitation peak at 494 nm and emission peak at 518 nm (green light).

For this study, female nude CD1 mice were placed in a recovery box, heated at 37 °C, to allow tail vein dilation. After 10 minutes they were injected intravenously (IV) by tail vein, via a 1 ml syringe with a 25-gauge x 16 mm needle with 100 µg of lectin-FITC (L0401, Sigma Aldrich) diluted in 200 µl sterile saline at neutral pH. As suggested by the supplier, saline contained 1 mM $CaCl_2$, which improves lectin binding. Before injection, the lectin conjugate solution was centrifuged for 30 seconds at 2000 rounds per minute (Eppendorf centrifuge, 5424R) and only the supernatant was then administered. This step is useful to eliminate any protein aggregates that may have formed in solution, thereby reducing nonspecific

background staining. After 5 minutes' incubation of lectin-FITC (which is required to allow natural circulation of the compound around the body and binding to the blood vessels), mice were anaesthetized and sacrificed by pentobarbital overdose (i.p. administration). Surgical procedures for perfusion fixation were carried out as described in section 2.2.3. Samples were optically cleared with BABB as described in section 2.2.4.1 and imaged with OPT.

The second tested compound was lectin from *triticum vulgaris* (wheat) conjugated with tetramethylrhodamine isothiocyanate (TRITC). This lectin binds almost exclusively to the apical cell surface, with minor decoration of the endothelial basal cell membrane (168). TRITC is a bright orange-fluorescent dye, derivative of rhodamine, with excitation peak at 557 nm and emission peak at 576 nm. The TRITC-lectin (L5266, Sigma Aldrich) was administered following the procedure described for the first tested ligand, lectin-FITC. Although it would have been ideal to choose the same lectin used in the first part of the study, conjugated with a different fluorophore, this was not possible as the specific compound was not available. However, this is not thought to be a major issue as all the lectins used bind to the endothelium of the vessels and the focus of this study was on the fluorophores and not on the lectins. This was also confirmed by an experiment described in section 4.1.6.3, where a combination of two different lectins was used to label the vasculature of xenograft tumours. The vascular network of the control samples, which did not receive any treatment, was the same for both channels (Figure 4.11), showing that there was no detectable difference in the lectins binding.

The third tested compound was lectin GS-II conjugated with AlexaFluor 647 (L-32451 Life technologies). Lectin GS-II is a 113,000-dalton protein isolated from the seeds of the tropical African legume *griffonia simplicifolia*. It is composed of identical subunits, each of which contains a single binding site specific for terminal non-reducing a- or ß-linked N-acetyl-D-glucosamine (169). This lectin preferentially binds to endothelial cells, and to a small degree to some epithelial cells in mouse tissues (170). AlexaFluor 647 is a fluorescent dye, with excitation and emission peaks at 650 nm and 665 nm respectively. Since the OPT manufactured by Bioptonics used in this thesis did not include filters in the range of wavelengths of

interest, a new combination of filters was purchased (Chroma, excitation filter: ET620/60x, emission filter: ET700/75m). The characteristics and the spectra of the three fluorophores tested in this thesis are summarised and shown in figure 3.9.

3.5 Results

The fluorescent conjugate lectin-AlexaFluor 647 was shown to be the most suitable compound to analyse tissue vascular architecture with OPT. Indeed, the other two compounds tested in this thesis had negative outcomes, in which the vascular network could not be detected when imaging with OPT, despite being visualized with confocal microscopy (Figure 3.6). This was noticed not only in brains but also in tumours and other organs imaged, such as heart, kidney, liver, and lung. Failed binding of the lectin to the endothelium of the vasculature could be one reason. Thus the same labelled samples were imaged with a confocal microscope (Zeiss LSM710) to check fluorescence and lectin binding. Figure 3.6 C-D, G-H, M-N shows confocal microscopy images of tissues successfully labelled with lectin-FITC. Despite the background autofluorescence, the blood vessels are clearly identifiable in these images.

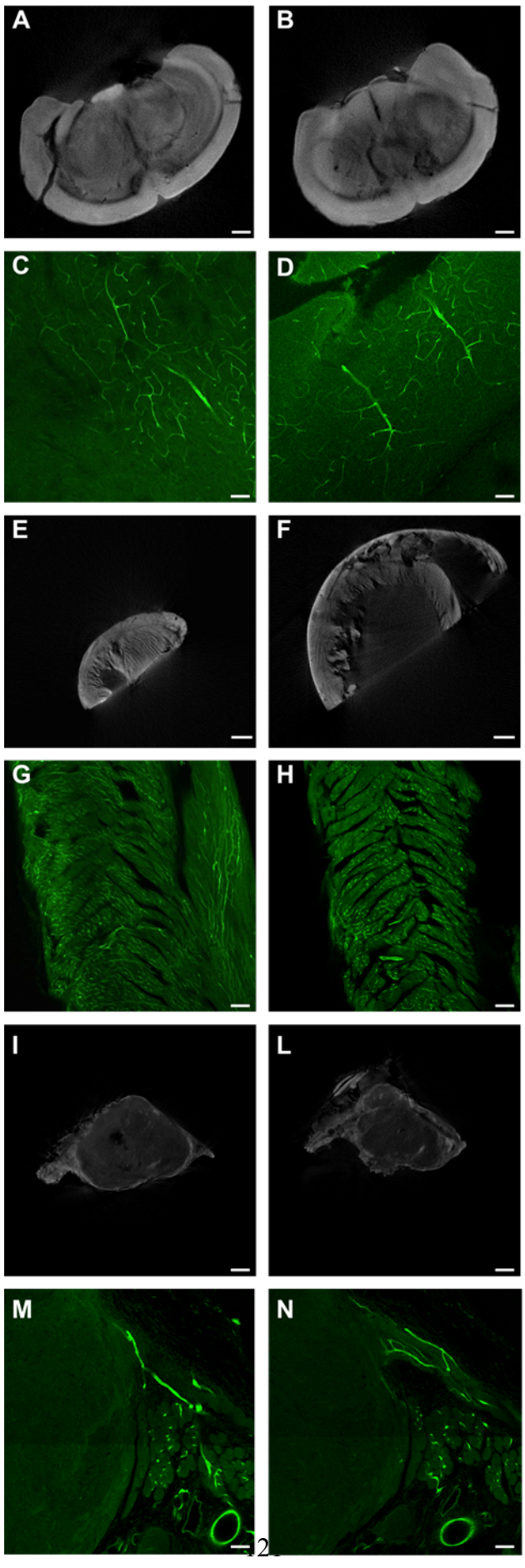
A
B
C
D
E
F
G
H
I
L
M
N

Figure 3.6: Multimodal imaging of lectin-FITC labelled vascular tissues. A-B, E-F, I-L) OPT images. The images are reconstructions from OPT projections. No vasculature can be observed in the OPT images. All the pairs of images were acquired within the same organ section at two different depths. C-D, G-H, M-N) Confocal microscopy images of 2 mm thick tissues. The stained vessels were clearly visible at different imaging penetrations. A-D) Images of mouse brain. E-H) Images of mouse heart. I-N) Images of subcutaneous tumour. Scale bars, A, B, I, L) 100 μm, E, F) 120 μm, C,D, G, H, M, N) 10 μm.

After confirming that the lectin had bound efficaciously to the vascular bed of the organs, it was hypothesized that the FITC was not detectable by OPT due to its emission wavelength (518 nm), which was too close to the range of the tissues endogenous autofluorescence (19). Hence the experiment was repeated using lectin conjugated with TRITC, whose wavelength was found to be still too close to the autofluorescence spectrum to be detected by OPT. On the contrary, the labelled vessels could be visualized with confocal microscopy, as it is shown in Figure 3.7.

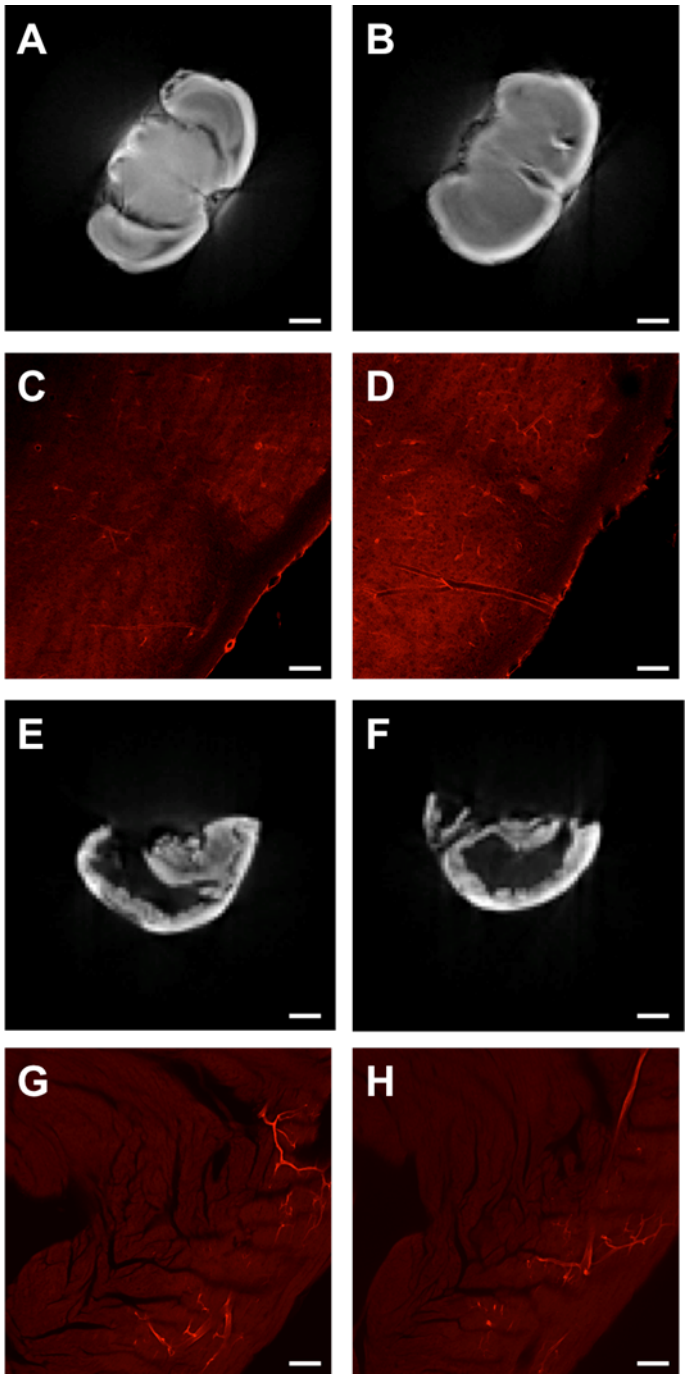

Figure 3.7: Multimodal imaging of lectin-TRITC labelled vascular tissues. A-B, E-F) OPT images. The images are reconstructions from OPT projections. No vasculature can be observed in the OPT images. All the pairs of images were acquired within the same organ section at two different depths. C-D, G-H) Confocal microscopy images of 2 mm thick tissues. The stained vessels were clearly visible at different imaging penetrations. A-D) Images of mouse brain. E-H) Images of mouse heart. Scale bars, A, B,) 100 µm, E, F) 120 µm, C,D, G, H) 10 µm.

Only the third tested compound, lectin-AlexaFluor 647, proved successful for imaging the labelled vascular bed with OPT. Figure 3.8, which shows the vascular network of a colorectal subcutaneous tumour, proves the approach for vasculature labelling with lectin-AlexaFluor 647 to be successful. It can be compared to figure 3.6 I-L, where the vasculature of the tumour was labelled with lectin conjugated with FITC but could not be detected with OPT. The study of tumour vascular networks, together with further applications of the illustrated method, will be presented and discussed in the next chapter (Chapter 4).

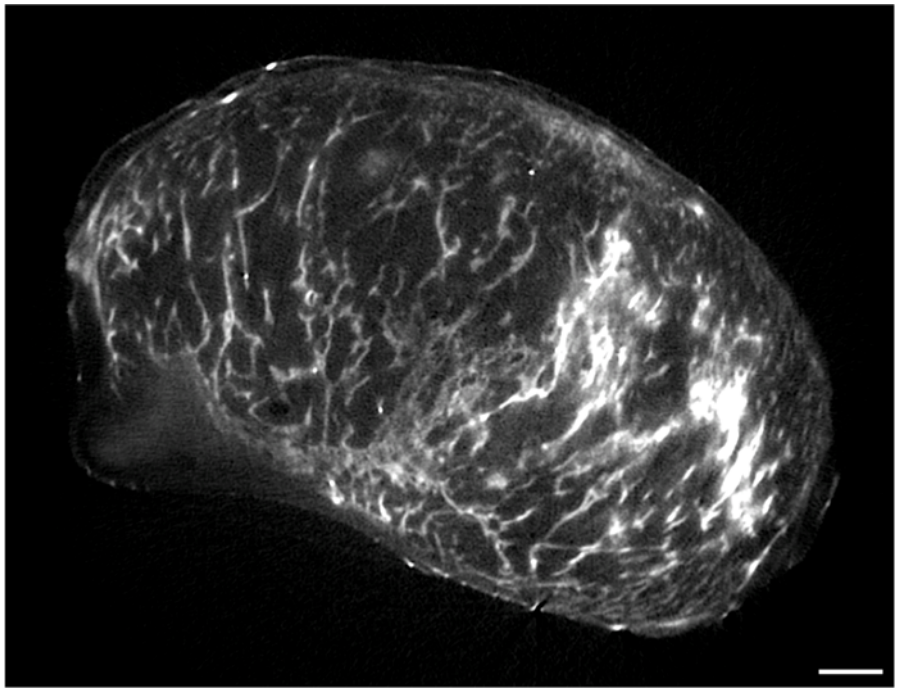

Figure 3.8: OPT reconstructed slices of a colorectal carcinoma, LS147T cell line. The vasculature of the tumour was labelled *in vivo* with 100 µl lectin-AlexaFluor 647 and is clearly visible in the image acquired with OPT. Scale bar, 100 µm.

3.6 Discussion

Two approaches for vasculature labelling were tested in this study: vascular casting with radiopaque polymers and fluorescently conjugated lectins. As shown by figure 3.4, fluorescently-labelled lectin proved to be a more suitable method when compared to radiopaque polymer injection medium to stain the vascular network. Indeed, limitations of the Microfil resin method include its discontinuity within the

vasculature and the rupturing of some vessels. Also, the casting agent fills large vessels easily but does not always fill sufficiently smaller vessels and capillaries.

The methods described in paragraph 3.3 include some protocol adjustments made in this study to improve the radiopaque polymer injection medium method. Despite these adjustments, this method still presents several limitations. Furthermore, the vasculature stain with lectin was more straightforward and slightly cheaper. Certainly, vasculature labelling with fluorescent compounds such as lectin-AlexaFluor 647 costs about £18, against the £32 for vascular casting with Microfil.

Three fluorescently labelled lectins were tested in this study. The first two tested fluorophores resulted to be not suitable for imaging vasculature with OPT, their main issues being their emission wavelength: both FITC and TRITC emit in the far green area of the visible spectrum, which overlaps with the wide tissue autofluorescence emission spectrum (Figure 3.8). Autofluorescence spectra are generally broad (from 500 to 540 nm), extending over several hundred nanometres. Hence, its interference is often significant at the same emission wavelengths as FITC and TRITC. Autofluorescence gets particularly strong after fixing and dehydrating the samples for OPT imaging. Indeed, formaldehyde forms covalent bonds between adjacent amine-containing groups through Schiff acid-base reactions. As a consequence, fluorescent products are formed, resulting in an intense fluorescent background (171). Also, autofluorescence tends to increase when fixation is longer or warmer (over 59 °C).

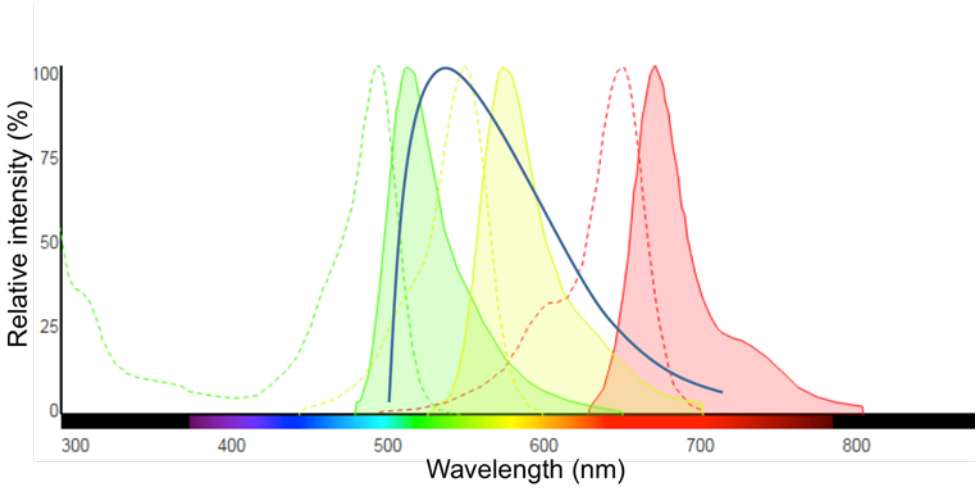

Fluorophore	Excitation peak (nm)	Emission peak (nm)
FITC	494	518
TRITC	557	576
AlexaFluor 647	650	665

Figure 3.9: Normalized fluorescence spectra of different fluorophores and tissue autofluorescence and summarizing table. Excitation (dashed lines) and emission (continuous lines) spectra are depicted for FITC (green), TRITC (yellow) and AlexaFluor 647 (red). The blue continuous line represents tissue autofluorescence. From the images it is clear that the autofluorescence spectrum overlaps with both FITC and TRITC, with the effect of masking this fluorophores in OPT imaging. Instead, AlexaFluor 647, which is more shifted towards the NIR part of the spectrum, successfully be visualized by OPT despite tissue autofluorescence.

Most probably, the signal from FITC and TRITC was visible with confocal microscopy due to the high power laser of the microscope (Argon: 25 mW, 561 nm: 15 mW), but not visible when imaging with OPT due to its wide-field light source (X-cite 120Q, Excelitas technologies, USA) and the different operational principles: in the OPT system the signal from the sample is integrated through the whole sample volume, hence if the background is stronger than the signal emitted from the fluorophores, the signal to noise ratio (SNR) is too low and the fluorophore conjugated to the lectin cannot be visualized. Furthermore, shifting up towards the infrared end of the spectrum has proven to considerably improve the image quality, as the level of light penetration is higher in this region of the spectrum.

For the first time, in this study vascular networks in colorectal carcinoma were labelled with fluorescently conjugated lectins and imaged in 3-D with OPT. The same samples were also imaged with μCT with the aim of investigating the ability of

the two *ex vivo* techniques to acquire fine details of mouse vasculature, as there are no previous studies which show such a comparison.

Chapter 4: Three-dimensional visualization and analysis of tumour vasculature after vascular disrupting treatment

In this chapter, the techniques for vasculature labelling developed in Chapter 3 and the optical clearing approaches developed in Chapter 2 are applied to both healthy and diseased vascular networks. OPT was used to produce high-resolution three-dimensional images of vascular networks obtained by labelling vasculature with fluorescent lectin. This technique was applied to tumours, towards t he ultimate aim of analysing drug delivery and the effects of treatments on vasculature parameters such as vascular density and vessel diameter.

The ability of OPT to produce high-resolution 3-D images of both fluorescent and nonfluorescent biological specimens allows the visualization of a wide range of internal structures other than blood vessels. With OPT, multiple independent signals within the same specimen can be imaged. For instance, in a single tumour scan multiple fluorophores could be used to stain several aspects of tumour pathophysiology such as angiogenesis, changes in tumour vasculature after administration of therapeutic agents, hypoxia and necrosis.

The aim of this research was to analyse the response of xenograft subcutaneous colorectal tumours to the vascular disrupting agent Oxi4503 at different time points in 3-D with high resolution. This was achieved using the combination of fluorescent compounds and OPT. The final objective of the study presented in this chapter was to analyse and compare the ability of OPT and HREM to investigate vascular networks within metastatic mouse livers.

4.1 Lectin-mediated vasculature labelling in subcutaneous tumours

4.1.1 Tumour

4.1.1.1 Angiogenesis

Angiogenesis, the growth of new blood vessels, has a crucial role in development and repair of organisms. For instance, with angiogenesis the embryo goes from receiving its nutrition by diffusion to being a highly vascular organisms, able to develop and grow though its vascular supply (172). During the first step of vessel formation, called vasculogenesis, angioblasts (endothelial cell precursors) migrate to specific areas, differentiate and assemble in solid endothelial cords which become vessels.

Angiogenesis occurs through the sprouting of new vessels from pre-existing ones or by longitudinal separation of existing vessels with periendothelial cells (Figure 4.1). These cells then form a different structure depending on their function and the type of vessels they will form (i.e. artery, vein or capillary) (173). The migration of endothelial cells is enabled by dilation of supplying vessels, increased vessel permeability and degradation of the surrounding matrix. Vasodilation results from the production of nitric oxide (NO), which upregulates angiogenic signals such as *vascular endothelial growth factor* (VEGF), the signal protein that mediates vascular permeability stimulating vessel sprouting and splitting (174). Tumour cells themselves have shown to line the tumour vessels together with endothelial cells, forming a mosaic structure (175).

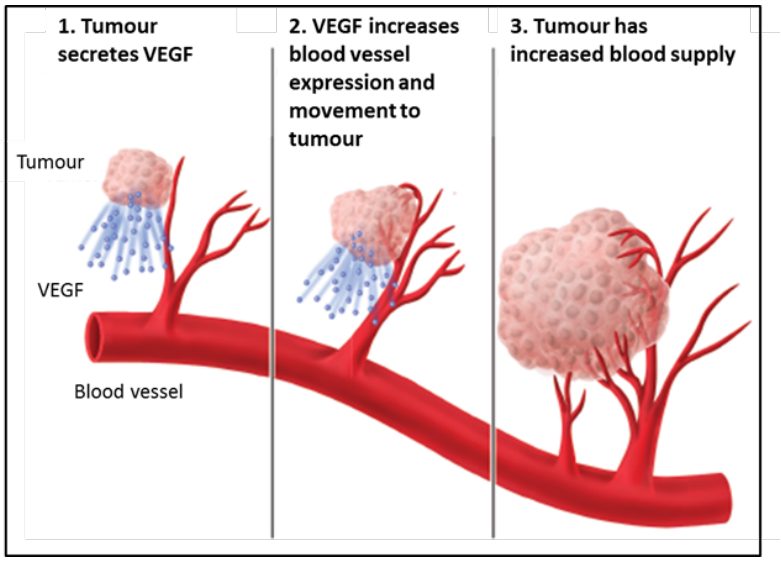

Figure 4.1: Key steps in tumour angiogenesis. Vascular endothelial growth factor (VEGF) is secreted by tumour cells. Endothelial cells proliferate, migrate and assemble to form new blood vessels which increase tumour blood supply. The image was adapted from ref. (176).

The hypothesis that tumour growth is angiogenesis-dependent was first proposed in 1971 by Folkman (177). He also demonstrated that, generally, tumours cannot grow beyond 2 mm in diameter without developing a vascular supply because of the tumour requirement for oxygen and nutrients, and that through angiogenesis the primary tumour not only grows but also disseminates metastases. The tumour vasculature is structurally and functionally abnormal compared to normal healthy vessels (Figure 4.2) (178, 179): the size of the lumen is irregular, the endothelium is multi-layered and the vessels can have several deviations and branches,. This complex structuring can cause inefficient blood flow, which is typical of tumours (180).

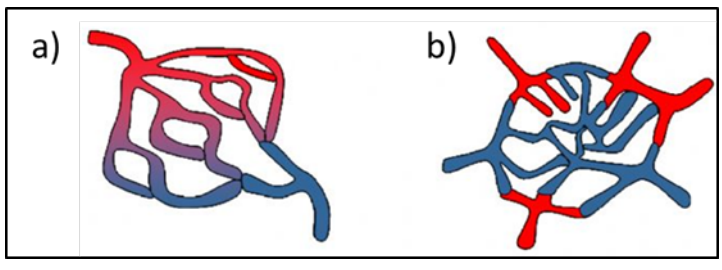

Figure 4.2: Comparison of normal (a) and tumour (b) vasculature. (a) Normal blood vessels are organized in a hierarchy of evenly distributed arteries, capillaries, and veins. (b) Tumour blood vessels are highly heterogeneous and consist of irregular branches with arteriovenous shunts. Image adapted from ref. (181).

These differences between newly formed and pre-existing blood vessels has lead to therapeutic strategies based on identification of drugs able to selectively target newly formed tumour vessels selectively (182, 183) and on antiangiogenic drugs (such as bevacizumab (Avastin), an anti-VEGF antibody (184, 185), which inhibit the formation of new vessels).

4.1.1.2 Vascular-targeting therapies

Anti-angiogenic and antivascular therapies have been studied extensively over the past two decades. While the first group of drugs aim to arrest the formation of new vasculature in tumours, the second group targets existing vessels (Figure 4.3).

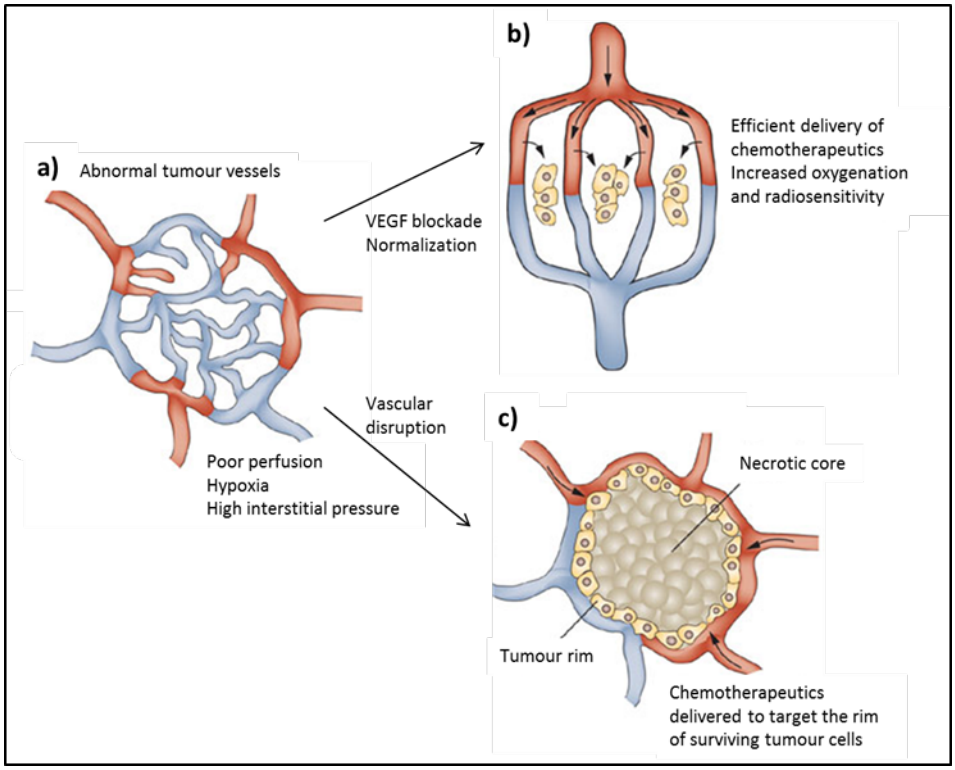

Figure 4.3: Diagram illustrating the different preclinical strategies of angiogenesis-inhibiting agents (AIAs, b) and tumour-vascular disrupting agents (tumour-VDAs, c) on abnormal tumour blood vessels (a). a) The tumour vasculature is highly abnormal and does not exhibit the normal architecture of arterioles, capillaries and venules. b) Treatment with AIAs causes vessel normalization, which results in improved perfusion and allows delivery of chemotherapeutic agents and/or increased oxygenation to aid radiotherapy. c) Treatment with VDAs leads to collapse of tumour vessels and central necrosis. The surviving rim of tumour cells can potentially be targeted with standard therapies. Image adapted from ref. (186).

Low molecular weight vascular disrupting agents (VDA), and more specifically tubulin-binding combretastatins, cause rapid and selective blockage of the established tumour vasculature, leading to cell death (187). Combretastatins, originally isolated from the South African willow tree *combretum caffrum* (188), are strong inhibitors of tubulin polymerization and competitively inhibit colchicine binding to tubulin (189, 190). The water-soluble combretastatin prodrug CA4P, has been investigated in several preclinical studies, and has the effect of shutting down tumour blood flow, which inhibits tumour growth and formation of metastasis in animal models (191-193).

The effects of combretastatins have been documented with techniques such as histology (194, 195), MRI (196) and *in vivo* confocal microscopy (197). These studies have shown that the response of tumour vasculature to the VDA can be divided into two main phases: a destruction phase (6-8 hours after VDA administration) and a following recovery phase (197). The rapid vascular shutdown and extensive vessel fragmentation observed in the first phase cause decreased perfusion, especially in the central part of the tumour (196, 198), and an increase in hypoxia and cell death (198). The surviving vessels in the rim of the tumour remain intact, allowing the recovery phase to start, and resulting in increased perfusion and reduction of hypoxia (197). At 24 hours after the administration of treatment, the tumour core has become necrotic due to the lack of nutrients and oxygen, while neovascularization can be observed in the tumour rim (197).

4.1.1.3 Tumour vasculature imaging and modelling

In parallel with the progress made in the past few years in the study of antiangiogenic and vascular disrupting drugs for tumour treatment, a need has arisen for the development of high resolution imaging techniques to examine tumours and quantify angiogenesis. Indeed, tumour vascularization is usually measured by calculating microvessel density immunohistochemically by staining for endothelial antigens such as CD34 and VEGF (199).

The main drawback of this method is its intrinsic 2-D nature, which does not allow representation of vascularity throughout the entire sample. Indeed, recent studies

have demonstrated that the attempt of reconstructing the whole tumour vasculature from histologic serial sections presented issues such as slice misalignment and missing sections (114, 200).

The recent development of new imaging techniques (201) and computational models (202) has contributed to improve our understanding of tumour angiogenesis and microenvironmental changes such as tumour blood flow (203), oxygen transport (204) and VEGF distribution (205). Numerous studies rely on modelling to provide quantitative insights into the interacting biophysical mechanisms that govern microcirculatory flow (206, 207). Along these lines, in this research a combination of optical clearing methods and *ex vivo* imaging techniques such OPT were used to investigate the morphological structure of treated and untreated tumour vascular networks in 3-D.

4.1.2 Aim of the study

The aim of this study was to determine the therapeutic effect of OXi4503 (Oxigene, supplied by Prof. Barbara Pedley, UCL Cancer Institute) on the vessel architecture of subcutaneous xenograft tumours by *ex vivo* imaging with OPT. OXi4503 is the diphosphate prodrug of combretastatin A1 (CA1), which is also isolated from *combretum caffrum* (188). It is a vascular disrupting agent which has been observed to block and destroy tumour vasculature, resulting in extensive tumour cell death and necrosis from 6 hours after administration (197, 208). The effects of the VDA were analysed at two different time points: 2 and 48 hours. These time points were chosen as previous experiments in subcutaneous tumours showed the first minor changes in the tumour vasculature 2-6 hours after administration of combretastatin (197) and critical changes and remodelling of the vascular networks 24 to 48 hours after OXi4503 dosing (40). The study was divided into two main parts: in the first batch of animals the effects of OXi4503 were analysed 48 hours after administration through single vasculature labelling with lectin-AlexaFluor 647. In the second batch of animals, the response of the tumours to the VDA were analysed with dual lectin labelling (lectin-AlexaFluor 568 and lectin-AlexaFluor 647) at 2 hours after OXi4503 dosing, as it is shown in section 4.1.3.6.

4.1.3 Methods

4.1.3.1 Tissue culture

All cell tissue culture work was performed under sterile conditions (Dr Sean Peter Johnson, UCL Cancer Institute). Cell lines grown *in vitro* were reanimated from a stock of frozen aliquots stored in liquid nitrogen. Cells were grown in ventilated flasks (Corning, Sigma-Aldrich, Gillingham, UK) under simulated physiological conditions of 37 °C and 5% CO_2.

4.1.3.2 Cell lines

The human colorectal adenocarcinoma cell lines SW1222 and LS174T were acquired from UCL Cancer Institute stocks at passages p2 and p5 respectively. These two cell lines exhibit different vascular structures. While SW1222 tumours are highly perfused with a complex vascular network, LS174T tumours are not as well vascularised and are more likely to feature hypoxic and necrotic regions (198, 209).

All cell lines were shown to be negative for mycoplasma infection by an in house polymerase chain reaction (PCR) test before collection, and at subsequent checks. Growth conditions were checked with the American Type Cell Culture website (210). Cells were routinely cultured in D-Modified Eagles Media (DMEM, Sigma-Aldrich, Gillingham, UK) with the addition of 10% foetal bovine serum (FBS), 1% L-glutamine (100x) and 1% non-essential amino acids (100x, all from Invitrogen, Paisley, UK).

4.1.3.3 Cell culture

Cells were passaged under sterile conditions. At each passage cell flasks were checked under a brightfield microscope for signs of infection. At any indication of possible infection cells were discarded immediately. Cell medium was changed every 2 to 3 days to maintain nutrient levels. To prevent contact-growth inhibition and ensure exponential growth, cells at ~80% confluency were split as follows: medium was removed via aspiration and adherent cells rinsed with phosphate buffered saline (PBS, Lonza, UK) to remove dead cell debris, growth factors and any remaining media. This PBS was then removed and 1 ml of trypsin-EDTA (Source Bioscience UK ltd) added per ~30 cm^2 surface area of flask. Flasks were placed in

the incubator for 5-10 minutes until the cells had detached from the monolayer of the flask and were in suspension. The action of trypsin was then inhibited by the addition of an equal amount of FBS containing media as trypsin used, a single cell suspension was achieved by pipetting. Between 1:2 and 1:8 dilution, based on apparent confluency of the flask monolayer, was then passaged into a new flask, topped up with media and returned to the incubator. A complete record of passage number, date and dilution factor was kept every time cells were split.

4.1.3.4 Preparation for i*n vivo* work

For *in vivo* experimentation, the number of required cells was calculated as follows. Cells were detached, pelleted, washed in PBS, re-pelleted and counted with a Countess automated cell counter (Invitrogen, Limited, Paisley, UK). A cell suspension/trypan blue (Sigma-Aldrich, Gillingham, UK) 1:1 mixture was loaded into a Countess slide and inserted into the machine for automated cell count. Results were checked to ensure correct identification of viable and non-viable cells via trypan blue exclusion.

The cell suspension was then pelleted by centrifugation at 455 g for 5 minutes and resuspended in the desired volume of serum free media, depending upon the *in vivo* experimental procedure. The final cell suspension was used *in vivo* immediately to preserve cell viability and limit any potential cell aggregations.

4.1.3.5 Pre-clinical subcutaneous tumour model

Adenocarcinoma cell lines SW1222 and LS147T were prepared through tissue culture techniques to a concentration of $5x10^6$ per 100 µl of serum free media (Dr Sean Peter Johnson, UCL Cancer Institute). A 100 µl bolus of cells was injected subcutaneously into the right flank above the hind leg of healthy female MF1 *nu/nu* mice aged 6-8 weeks, weight ~25 g. A total of 20 female *nu/nu* mice were injected with $5x10^6$ tumour cells each: for the first part of the study (single vasculature labelling) 6 mice were injected with SW1222 cells and 6 mice with LS147T cells. For the second part of the study (dual vasculature labelling) 8 mice were injected with SW1222 cells. Injections were made via a 1 ml syringe with a 25 gauge x 16

mm needle, within a sterile down-flow cabinet. Animals were returned to the individually ventilated cages (IVCs) and checked daily for tumour growth.

A set of digital callipers were used to measure tumour volume; animals were restrained and tumour length, breadth and height measured. To calculate volume (V) the ellipsoid formula from three distinct measurements, as seen below (Eq. 4.1), was used as this has been shown to provide the most accurate estimate of relative and actual tumour mass (211).

$$V = L \times W \times H \times \left(\frac{\pi}{6}\right) \qquad \text{Eq. 4.1}$$

where L is the length of the subcutaneous tumour, W is the width and H is the height. The maximum volume permissible was 1.5 cm^3, after which the mice were sacrificed.

4.1.3.6 Tumour treatment

After a period of 10 days the major part of the xenograft tumours was 60-80 mm^3. The volume of the tumours at this time point was measured with a digital calliper and is shown in Table 4.1.

Tumour Number	Tumour Length (mm)	Tumour Width (mm)	Tumour Height (mm)	Volume (mm^3)
SW1222, # 1	6.5	5.1	4.3	74.5
SW1222, # 2	5.8	4.8	4.1	59.5
SW1222, # 3	6.0	4.9	4.2	64.2
SW1222, # 4	6.7	5.2	4.3	77.9
SW1222, # 5	5.7	5.2	4.0	61.6
SW1222, # 6	6.1	4.6	3.9	56.9
LS147T, # 1	5.8	5.3	4.2	67.1
LS147T, # 2	6.2	5.1	3.9	64.1
LS147T, # 3	5.7	4.8	4.0	56.9
LS147T, # 4	5.9	5.2	4.3	68.6
LS147T, # 5	6.4	5.2	4.4	76.1
LS147T, # 6	6.5	5.4	4.3	78.5

Table 4.1: Size of xenograft subcutaneous SW1222 and LS147T tumours for single labelling study. The measurements were taken with a digital calliper 10 days after tumour cells injection.

Tumour Number	Tumour Length (mm)	Tumour Width (mm)	Tumour Height (mm)	Volume (mm^3)
SW1222, # 1	6.0	4.7	4.2	62
SW1222, # 2	5.3	5.3	4.4	65
SW1222, # 3	5.7	5.1	4.0	61
SW1222, # 4	6.2	5.0	3.9	63
SW1222, # 5	6.4	4.9	4.2	69
SW1222, # 6	6.3	4.9	3.9	63
SW1222, # 7	6.5	5.1	4.2	73
SW1222, # 8	5.9	5.3	4.2	69

Table 4.2: Size of xenograft subcutaneous SW1222 and LS147T tumours for dual labelling study. The measurements were taken with a digital calliper 10 days after tumour cells injection.

For the first part of the study (single lectin labelling) 3 mice bearing SW1222 tumours and 3 mice bearing LS147T tumours were injected i.v. with the vascular disrupting agent OXi4503 combretastatin (40 mg/kg, 4 mg/ml concentration) while the control 6 mice (3 SW1222 and 3 LS147T tumours) were injected with sterile saline (250 µl). The dose of combretastatin was chosen according to previous studies done by other researchers in the lab, which showed that the dose of 40 mg/kg was sufficient to achieve vessel destruction (40). Oxi4503 was developed by Oxigene, and procured by Professor Barbara Pedley (UCL Cancer Institute). 48 hours after injection, the mice were injected intravenously (through the tail vein) with 100 µl lectin-AlexaFluor 647 fluorophore diluted in 100 µl sterile saline at neutral pH containing 1 mM $CaCl_2$. The mice were then sacrificed and perfuse-fixed as described in section 2.2.3.

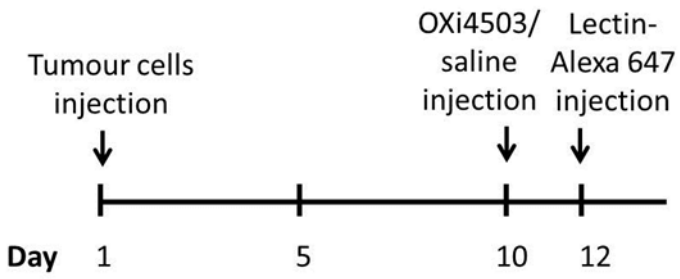

Figure 4.4: Timeline for the tumour single fluorophore labelling experiment

For the second part of the study (dual lectin labelling), 8 mice bearing SW1222 tumours were injected i.v. (through the tail vein) with 100 µg lectin-AlexaFluor 647 diluted in sterile saline at neutral pH (100 µl) containing 1 mM $CaCl_2$. This was followed by administration of OXi4503 (40 mg/kg, 4 mg/ml concentration) in 5 mice, while the 3 mice which acted as control were injected with 100 µl saline. After 2 hours, mice were injected i.v. (tail vein) with 100 µg lectin-AlexaFluor 568 diluted in sterile saline at neutral pH (100 µl) containing 1 mM $CaCl_2$, sacrificed and perfuse-fixed.

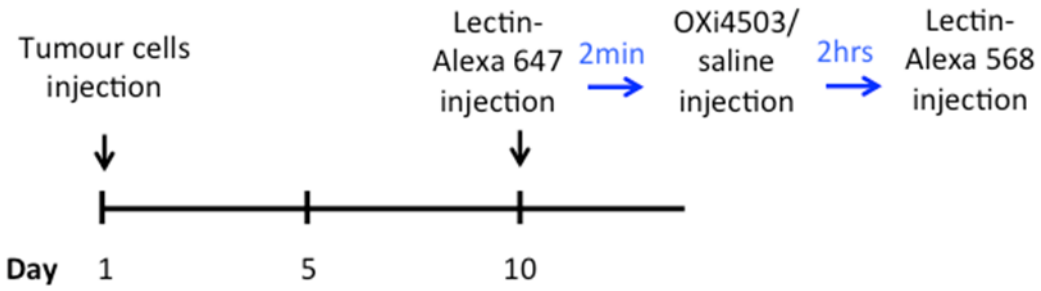

Figure 4.5: Timeline for the tumour dual labelling experiment

4.1.4 Tumour imaging

After fixation, the tumours were optically cleared with BABB. Details of the clearing procedure can be found in section 3.2.4.1. The effects of OXi4503 on the spatial distribution of tumour vasculature were visualized by optical projection tomography. The system used was a commercial OPT (Bioptonics, MRC Technologies, Edinburgh), which is the same system as described in section 1.10.1.

The integrated excitation white light (X-Cite 120Q, Excelitas Technologies, USA) combined with an appropriate selection of filter sets allows the use of several commonly used fluorophores. The strong autofluorescence emission of the tumour tissue was used to form a detailed image of tumour morphology (filter set: excitation range 425/40 nm, emission range LP475 nm). Lectin-AlexaFluor 647 (excitation range 655/40 nm; emission range 716/40 nm) bound strongly to the vascular endothelium and provided medium signal intensities (filter set: excitation range 620/60 nm, emission range 700/75 nm). Lectin-AlexaFluor 568 was imaged with the filter set: excitation range 560/40 nm, emission LP610 nm. The measurements were performed with exposure times of ~1600-2000 ms for lectin-AlexaFluor 647 channel and of ~270-600 ms for lectin-AlexaFluor 568 channel per projection, depending on the tumour size. The rotation step was 0.45 degrees. The final xy resolution ranged from 4.3 μm to 8 μm, depending on the sample size hence on the field of view (212).

4.1.5 Image processing

A total of 1000 16-bit TIFF images per sample were generated. Thereafter, the tomography projection images were reconstructed with the Nrecon Software to generate cross-section images. Misalignment compensation was used to compensate possible misalignment during projection image acquisition, in order to reduce tails, doubling or blurring in the reconstructed image. The depth of correction for ring artefact reduction was set to 4 and the defect pixel masking was 50% for all the scans.

Reconstructed TIFF images were visualized and analysed using several software platforms: Amira (Visage Imaging, USA), Fiji (open source, NIH, USA), Matlab (Mathworks, Natick, MA) and IDL (Exelis Visual Information Solutions, CO, USA) by Dr. Simon Walker-Samuel (UCL Centre for Advanced Biomedical Imaging).

First, a 3-D Gaussian filter (3×3×3 kernel) with width of 50 pixels was applied. The smoothed data was subtracted from the original data in order to remove background variations in autofluorescence. A 3-D Hessian-based Frangi vesselness filter was then applied in Matlab to enhance and detect vessel- or tube-like structures. This enabled the determination of a threshold to segment blood vessels from background. A 3-D thinning algorithm was then applied to the vessel-enhanced data in ImageJ to skeletonize the vessels. Routines written in IDL were then used to determine vessel radii by growing from each point on the vessel skeleton, to its closest edge. The skeleton data was then converted to a graph format (nodes and segments) in Amira.

4.1.6 Results

4.1.6.1 Tumour optical clearing

Good transparency was obtained with tissue optical clearing with BABB in both models of subcutaneous colorectal carcinoma (LS147T and SW1222 cell lines). A representative sample is displayed in figure 4.6.

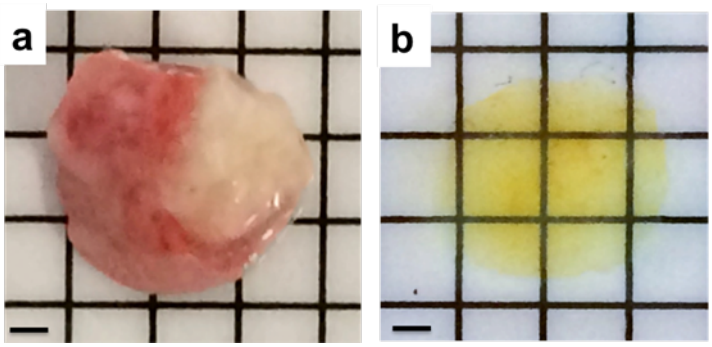

Figure 4.6: Representative xenograft subcutaneous tumour model (SW1222 cell line) before (a) and after (b) optical clearing with BABB. To overcome the problem of light attenuation in tissue, tumours were chemically treated to change their optical properties and to render them transparent. Scale bars, 1 mm.

4.1.6.2 Visualization of tumour morphology

Tissue autofluorescence images were used to create images of the xenograft tumour morphology. The variation of light attenuation caused by differences in the structural composition of the tissue resulted in autofluorescence-rich contrast, which allowed tissue components to be approximately differentiated (Figure 4.7 a, e).

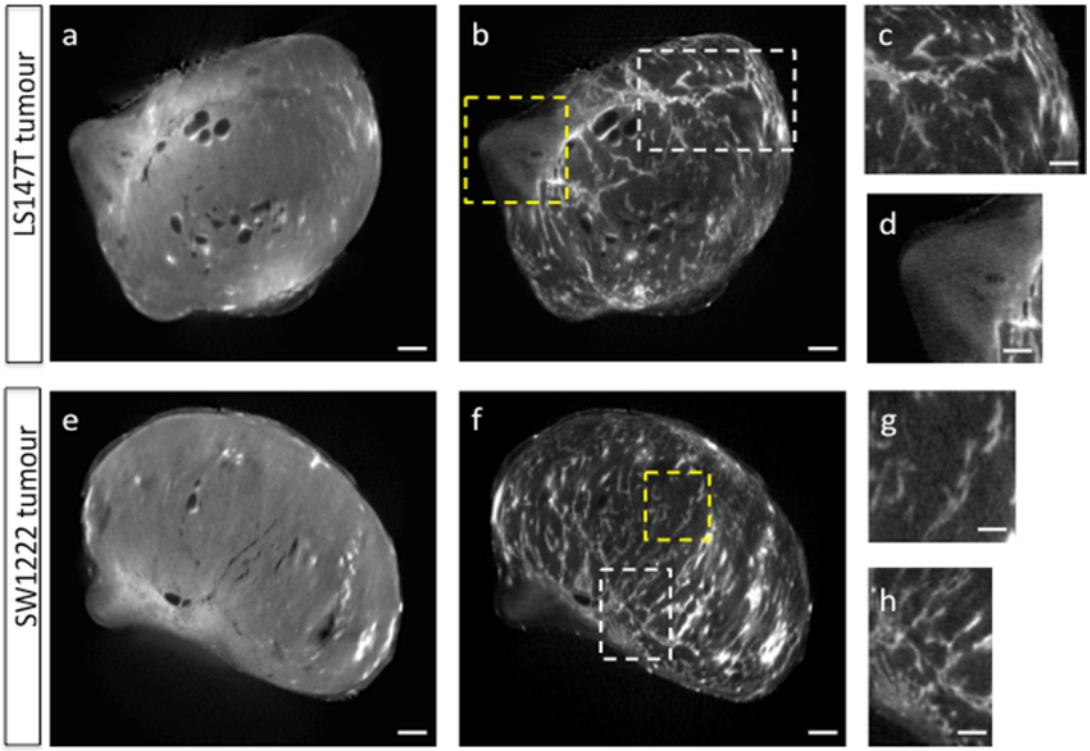

Figure 4.7: Visualization of tumour morphology and vessel architecture in untreated LS147T and SW1222 tumours. a-d) LS147T colorectal carcinoma. e-h) SW1222 colorectal carcinoma. a, e) Tissue autofluorescence allows acquisition of information about tumour morphology in LS147T (a) and SW1222 (e) colorectal carcinoma. b, f) The chaotic structure of the vessels (typical of tumours) stained with lectin-AlexaFluor 647 was clearly visible in the OPT reconstructed images. SW1222 tumours (f) appeared more vascularized than LS147T tumours (b), in accordance with previous studies (142). c-h) The blow-up images from b) and f) showed the heterogeneity of the tumour vessel networks. Some regions within the tumours are highly vascularized (c,h) whereas others provide a sparse or absent vasculature (d, g). Scale bars, 1 mm and 1.5 mm (blow-up images).

Tumour vasculature appeared chaotic and irregular, which is typical of tumours (113), and heterogeneous: some areas displayed high vascular density (Figure 4.7 c, h), whilst some showed more sparse or absent vascularization (Figure 4.7 d, g). The OPT images were broadly consistent with previous μCT studies of vascular corrosion casts (142, 213) and photoacustics findings (40), which showed that SW1222 tumours exhibit a more regular and densely packed blood vessel network compared to the LS174T tumours, which are characterized by a heterogeneous vascular distribution.

4.1.6.3 Effect of OXi4503 on tumour vasculature

The effects of OXi4503 on tumour vasculature after 2 and 48 hours were analysed by fluorescent examination with OPT after the injection of fluorescent compounds. Figure 4.8 shows a volume-rendered 3-D image, where control tumours are compared to treated tumours treated that were imaged at 48 hours post-dosing. The image shows the cross-sections of the tumour samples, and vessels are colour coded according to their size, from blue (~5 μm radius) to red (~30 μm radius). A reduction in tumour blood volume at all time points was caused by the administration of OXi4503 at a dose of 40 mg/kg in both LS147T and SW1222 models of colorectal carcinoma (Figure 4.9).

The vasculature disrupting effect of OXi4503 was mainly apparent in the tumour core in all treated SW1222 tumours (Figure 4.8 c), where an external rim of viable vessels, was apparent. The effect of OXi4503 in LS147T tumours was localized to several areas, and not concentrated in the core as in the SW1222 cell line (Figure 4.8 d): all the treated LS147T tumours show very few and diffuse vessels. These findings are in accordance with previous photoacustics studies (40).

Quantification of the different effect of the VDA in the tumour rim and core was not straightforward, are most of the tumours are not spherical, which made defining a central point non-trivial. However, some regions could be identified and the vessel density could be measured in these regions.

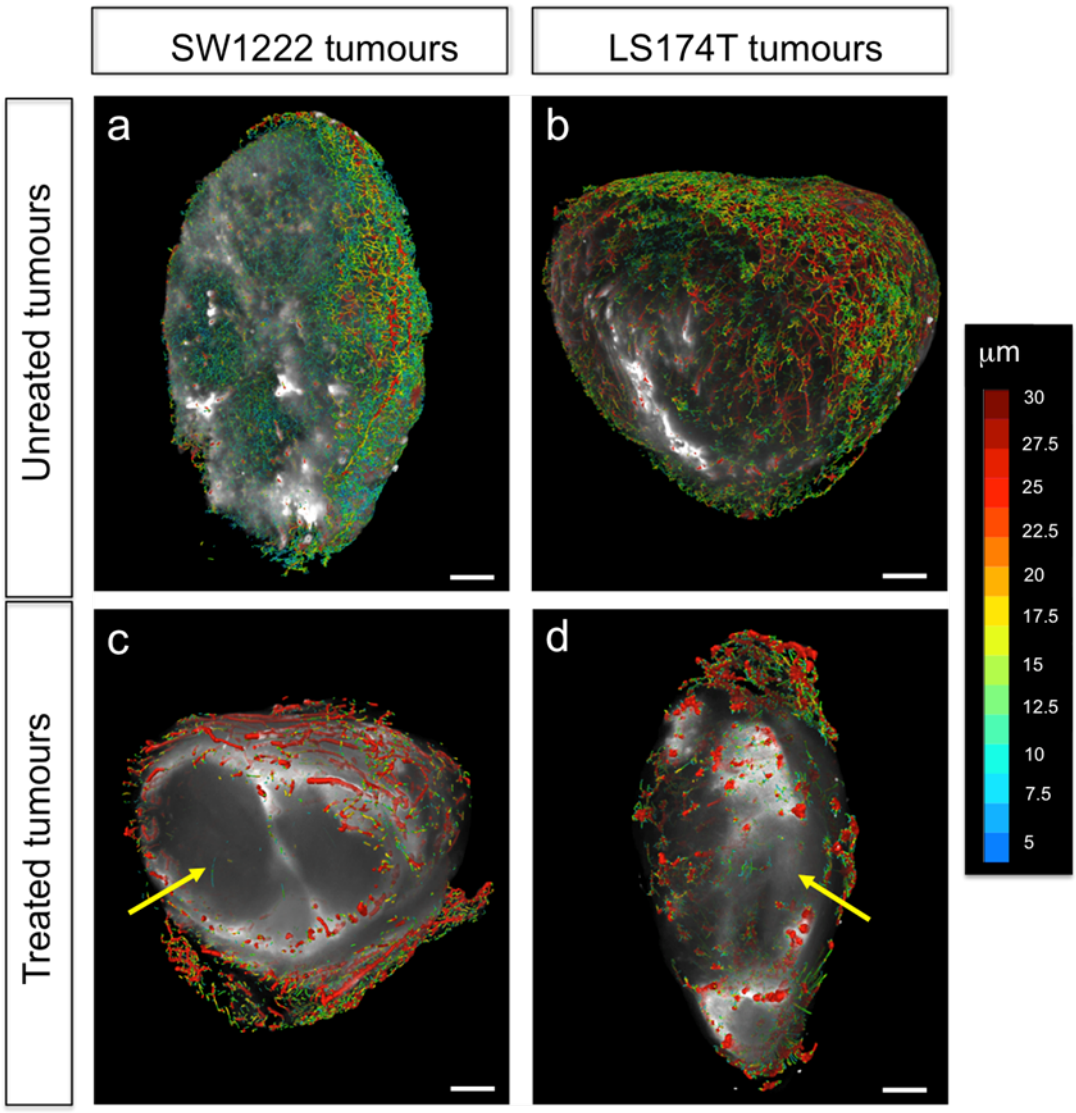

Figure 4.8: 3-D Volume renderings of tumour morphology and vessel network and effect of Oxi4503 48 hours after administration. The images represent cross-sections of whole tumours. Vessel networks were segmented from OPT data and were colour-coded for vessel size: red for bigger vessels and blue for smaller ones. Example control and treated SW1222 tumours are shown in (a) and (c), respectively; example control and treated LS174T tumours are shown in (b) and (d). The yellow arrows indicate the loss of central blood vessels 48 hours after administration of Oxi4503. Scale bars, 1 mm.

With the aid of computerized image analysis, total blood volume (measured in mm^3, where 1 mm^3= 1 µl) and mean vessel size were measured to compare treated and control groups in SW1222 and LS174T tumours. Figure 4.9 shows the results of quantification of the OPT data sets.

Differences between treated and control tumours were evaluated statistically with the Wilcoxon rank sum. This is a non-parametric statistical test, generally used for

quantitative non-normally distributed variables (or where normalcy cannot be determined) and for small samples. Compared to controls, the vasculature of the OXi4503-treated samples shows a different vascular architecture and density after drug administration. As expected, the total number of blood vessels decreased significantly as a consequence of the blood flow shutdown induced by the VDA. In both the tumour models the total blood volume began to decrease 2 hours after administration of antivascular treatment and decreased significantly by 48 hours ($P<0.05$). Figure 4.9 shows the results in tumours analysed 48 hours after OXi4503 dosing. For SW1222 treated tumours, the mean blood volume was 0.14 mm^3, whereas it ranged from 0.2 mm^3 to 0.3 mm^3 in the controls, with a mean of 0.25 mm^3. For LS147T treated tumours, the mean blood volume ranged from 0.03 mm^3 to 0.18 mm^3, with a mean of 0.11 mm^3, while it ranged between 0.2 mm^3 and 0.4 mm^3 in the controls, with a mean of 0.3 mm^3.

Furthermore, it was noticed that the radius of the remaining vessels had increased in treated tumours (Figure 4.9). This vessel dilation indicates increased vascular permeability, which is a direct effect of the treatment on endothelial cells. For SW1222 treated tumours, the mean vessel radius, expressed in pixels in the graphs (where 1 pixel = 3 μm) ranged between 3 and 3.5, with a mean of 3.25, while it ranged between 2.4 and 2.9 in the controls, with a mean of 2.64. For LS147T treated tumours, the mean vessel radius ranged between 2.8 and 5.2, with a mean of 4, while it ranged between 2.3 and 2.9 in the controls, with a mean of 2.6.

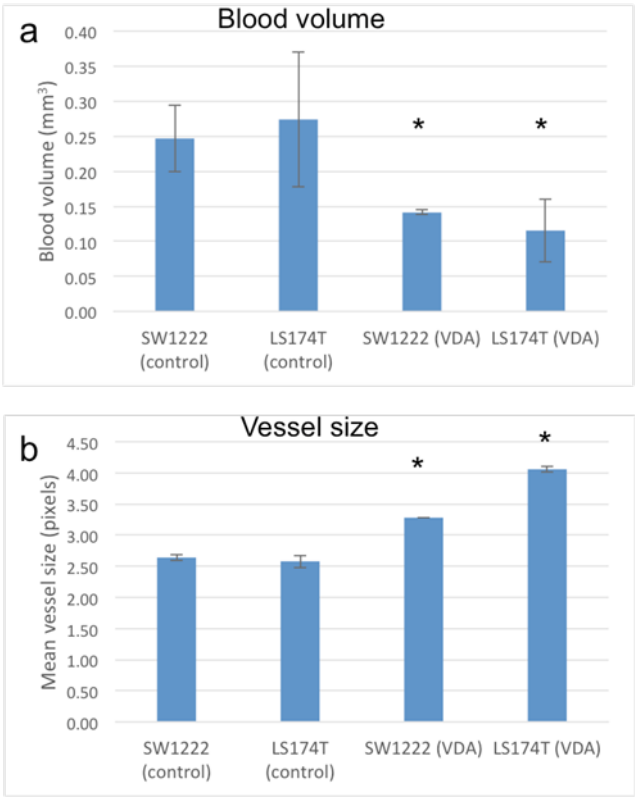

Figure 4.9: Quantification of antivascular treatment response at 48 hours post OXi4503 dosing. a) Quantification results of blood volume (mm^3) for treated and control groups of SW1222 and LS174T tumours. b) Measurements of mean vessel size (pixels) in treated and control groups of SW1222 and LS174T tumours. All values are given as means ± SD. *P<0.05.

In the second part of the study, the 8 xenograft colorectal subcutaneous tumours were stained *in vivo* with two fluorophores (AlexaFluor 568 and AlexaFluor 647) and imaged at 2 hours after VDA dosing to study the acute response of the tumours to OXi4503. The results obtained are displayed in figures 4.8 and 4.9, where OPT reconstructions and 3-D renderings are shown, respectively. It can be noticed that tumour blood vessels were affected as early as 2 hours after OXi4503 injection, in accordance with previous studies (214). However, this could be an effect of reduced lectin binding. Though, if this was the case, it would still only be in regions where the drug is acting, so it would still be a useful marker of drug action, even if it is not precisely reflecting compromised flow. Whether the VDA affects lectin binding would not be straightforward to determine with OPT. Nonetheless, the vessels appear as filled tubes rather than empty ones, which indicates that a reasonable amount of lectin can be seen in the vessel lumen and not just bound to the vessel wall.

Treated and untreated SW1222 colorectal tumours are compared in the OPT reconstructions shown in Figures 4.10- 4.12. Clear differences in the vasculature (yellow arrows) can be observed in the two channels used to image the treated tumours, showing the effect of the vascular disrupting agent. Vessels that are perfused prior to dosing with Oxi4503 are no longer perfused two hours later. This affect was not observed in images from control tumours, in which the vasculature appears unchanged at baseline and following dosing with saline (Figure 4.11).

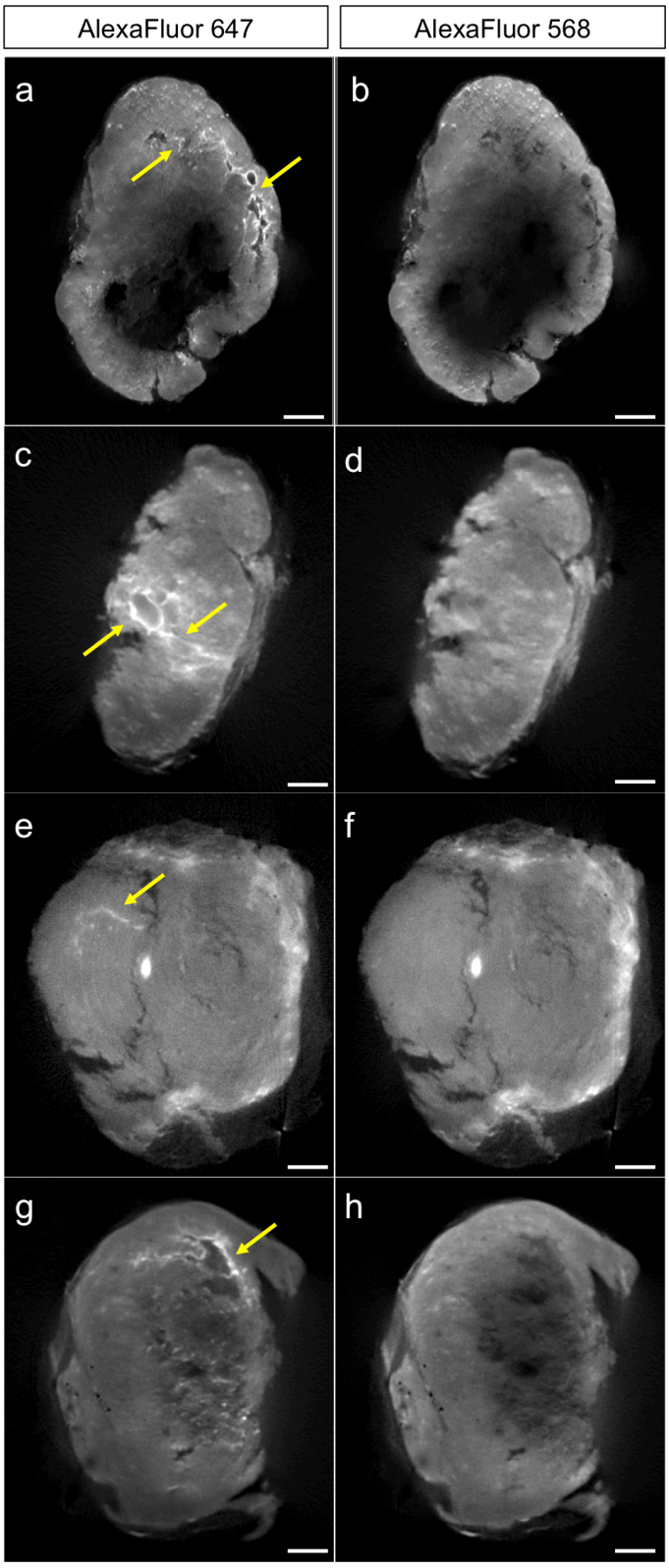

Figure 4.10: Images of OPT reconstructions showing four example SW1222 xenograft colorectal carcinomas. Each row represents an image of the sample acquired with two channels, Channel 1 (First column, AlexaFluor 647) and Channel 2 (Second column, AlexaFluor 568). The mice were sacrificed 2 hours after OXi4503 dosing. Yellow arrows point at lectin-labelled vasculature, which can clearly be observed. Scale bar, 1 mm.

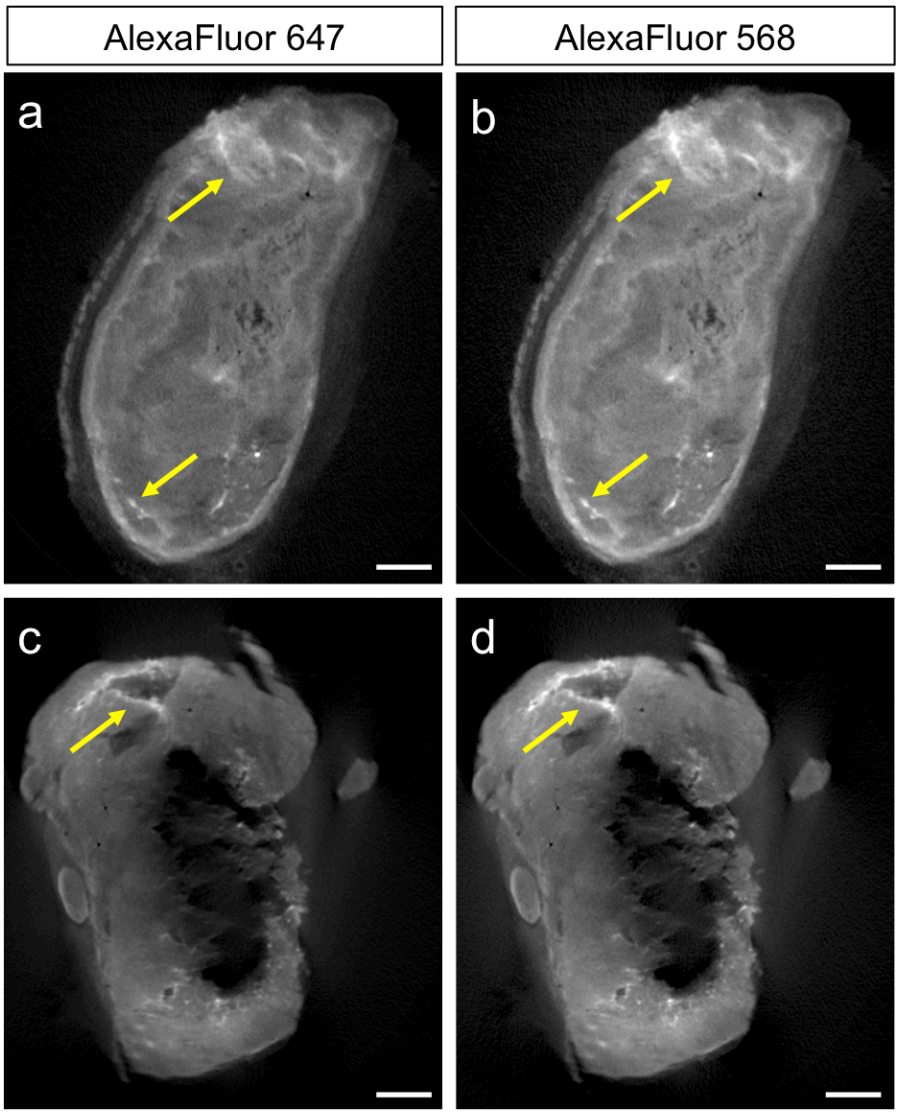

Figure 4.11: Images of OPT reconstructions showing untreated SW1222 xenograft colorectal carcinoma. a) Sample 1, Channel 1 (AlexaFluor 647) b) Sample 1, Channel 2 (AlexaFluor 568) c) Sample 2, Channel 1 (AlexaFluor 647) d) Sample 2, Channel 2 (AlexaFluor 568). No differences in vasculature were appreciated before and after administration of the VDA. Scale bar, 1 mm.

The effect of combretastatin can also be observed in 3-D in figure 4.12, where the vessels prior to Oxi4503 injection are represented in blue/green, while the vessels at 2 hours following Oxi4503 injection are represented in green. The clear regions show the areas where the vessels have been disrupted. In figure 4.12 b the loss of small vessel connections can be appreciated in higher detail.

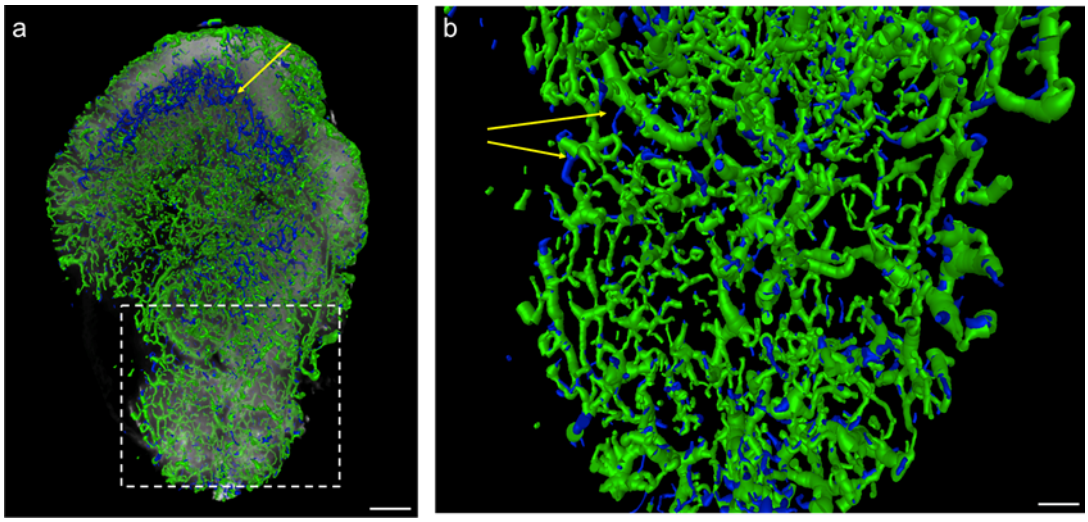

Figure 4.12: 3-D rendering of OPT images of LS174T colorectal tumour vasculature. a) Whole sample. The complex and chaotic structure of the lectin-AlexaFluor 647 stained tumour vessels is clearly visible. The clear regions represent the areas where the blood vessels are disappearing. b) Blow-up image. Blue/green: vessels prior to Oxi4503 injection. Green: vessels at 2 hours following Oxi4503 injection. The arrows point at regions where loss of vessels connecting central and peripheral tumour regions can be observed. Scale bar, 1 mm and 3 mm (blow-up).

4.1.7 Next step: vascular tree modelling

The structural data in colorectal carcinoma gathered in this study by OPT is being used to parameterize a mathematical model using *in vivo* blood rheology descriptions to simulate blood flow, perfusion and oxygenation in microvascular networks with the aim of simulating drug delivery. It is indeed evident how the development of drug delivery and new anti-angiogenic therapies can depend on crucial parameters such as intravascular pressure and vascular permeability. Therefore it can benefit from mathematical simulations of tumour microvascular hemodynamic, as demonstrated by Jain et al. (215). In their study, they developed a mathematical model to simulate interstitial fluid pressure (IFP) and interstitial fluid velocity (IFV) profiles in tumours. This is crucial since it has been observed that high IFP caused by hyperpermeable tumour vessels is an obstacle against drug delivery (132). Jain demonstrated that antiangiogenic therapy is able to decrease IFP by decreasing tumour size and vascular hydraulic permeability. Furthermore, the effect of anti-angiogenic therapy on tumour vasculature can be predicted with 3-D computational model, as it was shown by Wu et al. (216). Against this background, detailed information about the 3-D geometry of tumour vascular networks could improve

computational models, which would both increase the efficacy of drug delivery and contribute to the development of blood biomarkers for cancer detection (217).

In our preliminary study, network fluid pressure and tissue oxygen distributions in tumour vasculature were compared with the parameters typical of healthy networks (Paul Sweeney and Dr. Rebecca Shipley, UCL Department of Mechanical Engineering). The model used takes the structural data acquired with OPT and segments it into a series of cylindrical tubes of constant circular cross-section. For simplicity, a subnetwork is then extracted. Figure 4.13 shows some preliminary pressure distribution and vessel size data estimated in an untreated LS147T colorectal carcinoma (Dr Simon Walker-Samuel, Paul Sweeney).

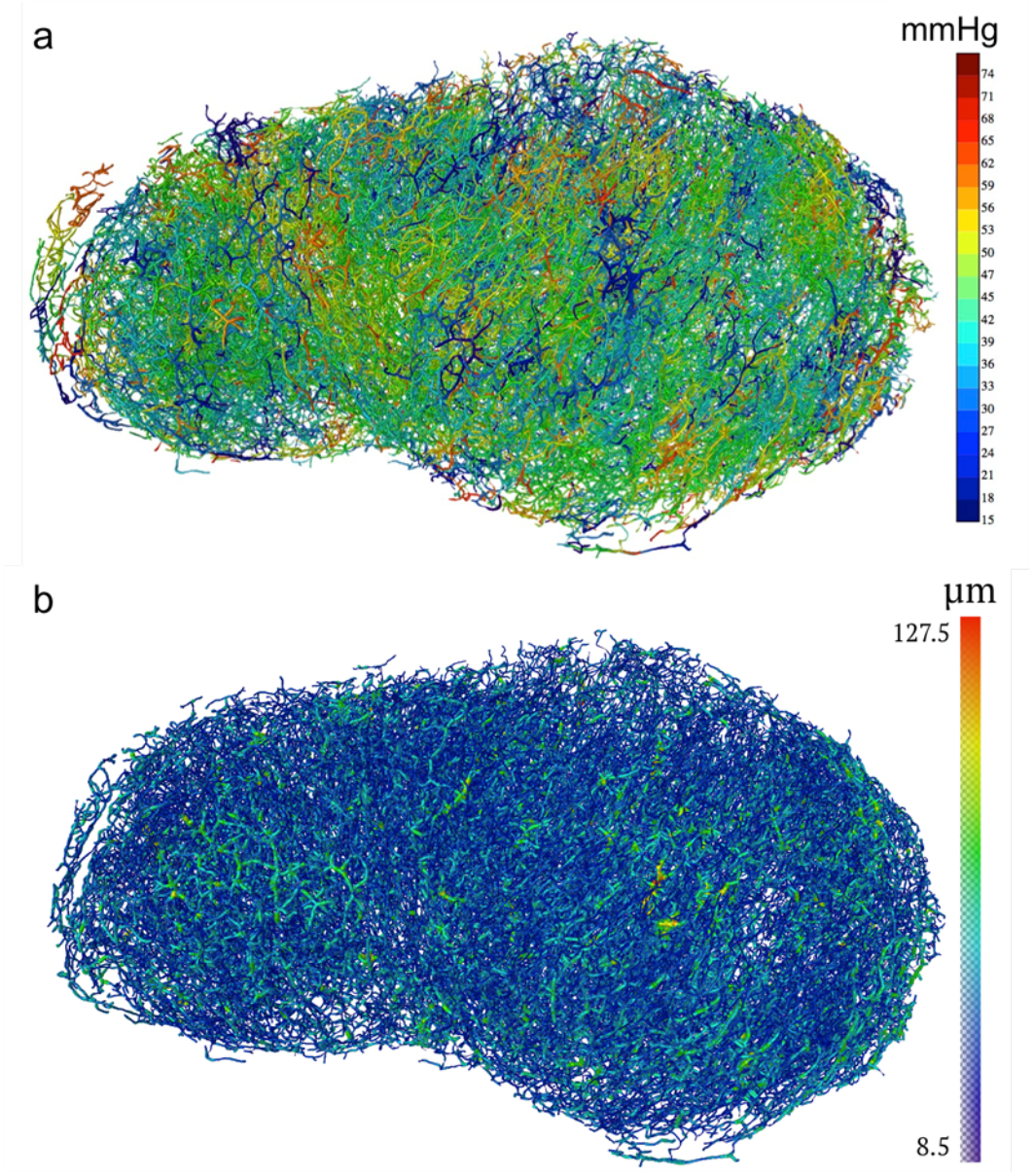

Figure 4.13: Example solutions of mathematical modelling of tumour blood flow in an example LS147T human colorectal carcinoma. a) Colours correspond to flow within the vasculature. Pressure goes from low (blue vessels) to high (red vessels). The diameters are shown as 20% of their actual value for visualization convenience. b) The colour distribution represents the vessel size. Vessel size goes from small (blue) to bigger (green and red). The diameters are shown as 25% of their actual value for visualization. The images were created by Paul Sweeney.

Potential development of this work is to induce a drug transport model which, combined with the above data, could prove useful in the advancements in cancer treatments. Indeed, current methods for 3-D imaging of microvasculature can benefit from the recently developed theoretical computational models. These can address limitations such as the difficulty to obtain detailed flow information, fundamental to

assess microcirculatory function together with structure information provided in our study where vessels were labelled with fluorescently conjugated lectin conjugated to analyse parameters such as vascular length density, vascular volume fractions or vessel-vessel spacing. The combination of morphological and flow information is crucial for understanding pathologies such as cancer. Indeed, networks with similar values of these parameters may nonetheless have entirely different functional characteristics because of different connectivity or diameter distributions. For example, in tumour networks high levels of perfusion and vascular density may coexist with significant tissue hypoxia because of functional shunting of blood flow through short pathways (218). Ideally, assessment of microcirculatory function should thus be based on information on both structure and flow distribution.

Therefore, mathematical modelling will assist in the interpretation of data obtained from 3-D images of microvascular networks acquired with optical projection tomography containing large numbers of segments, and will potentially lead to new insights into functional properties of the microcirculation in cancerous tissues.

4.1.8 Discussion

The purpose of this study was to investigate, using optical projection tomography, the effects of vascular disrupting therapies on colorectal carcinoma. Although it has very rarely been used to image tumours, high-resolution 3-D OPT imaging is a powerful approach for investigation of relationships between tumour angiogenesis and distribution of hypoxic and necrotic regions, as well as actions of the therapeutic agents (219, 220). Optical sectioning of tumour specimens allows 3-D analysis of relevant tumour parameters such as angiogenesis and vessel size on a cellular resolution, which cannot be achieved with classical histology. Indeed, two-dimensional investigation of tumour slices may not provide a sufficient overview of the inhomogeneous tumour morphology and physiology (113).

This study clearly demonstrated that OPT, in combination with fluorescence markers and advanced image processing techniques, enables 3-D visualization of vascular networks in whole big tumours with high isotropic resolution and allows quantification of tumour parameters such as total blood volume and vessel size. This

type of data is of particular importance when studying drug efficacy: in this research the use of OXi4503 as a vascular disrupting treatment was tested in two models of colorectal carcinoma and proved successful in destroying tumour blood vessels. In all xenograft tumours, the effect of the combretastatin could be assessed with unprecedented details after only 2 hours after i.v. administration of the drug, and significant changes in vascular structure, such as disruption of vessels and volume reduction in surviving vessels, occurred within 48 hours following therapy.

4.2 Vascular analysis of colorectal liver metastases

In this ongoing study, the optical methods developed in this thesis were applied to the analysis of vascular networks in both healthy and metastatic livers. Compared to subcutaneous tumours, orthotopic models of cancer are more clinically relevant and better predict drug efficacy (221, 222). Indeed they reflect the tumour microenvironment better than conventional subcutaneous xenograft tumour models since they are implanted directly into the organ of origin. Tumour cells can also be injected in a specific organ to create metastases in the organ of interest. For this study, models were established using previously published protocols, which show that injection of human colorectal cancer cell lines into the spleen of athymic mice produces tumour foci in the liver (223).

Previous OPT experiments were focussed on relatively large subcutaneous tumours, therefore the aim of this study was to investigate the feasibility of using OPT for visualizing small *in situ* metastases. Furthermore, the dual-labelling fluorescence technique was used to study the blood supply to liver metastases, and investigate whether it is primarily from the hepatic or the portal blood supply.

4.2.1 Background

4.2.1.1 Liver anatomy

The liver is the largest abdominal organ in the human body. Although the physiology of the mouse liver is essentially the same as the human liver, the anatomy is slightly different. Indeed, human liver is made up of four lobes- right, left, quadrate and caudate- while the rodent liver is divided into six lobes: upper and lower right, upper

and lower caudate, left lateral and mediane (Figure 4.14 a). The liver is located in the upper right-hand portion of the abdominal cavity, beneath the diaphragm and on top of the stomach, right kidney, and intestines. Its primary role is to clear the blood stream from toxins and foreign bodies. Its main functions are excretion of bile, lipid carbohydrate and protein metabolism, storage of vitamins and minerals.

The liver receives oxygenated blood from the descending aorta through the hepatic artery and venous blood from the intestines, pancreas and spleen through the portal vein (PV), which delivers approximately 75% of the blood to the liver (224) (Figure 4.14 b). The complex structure and physiology of the liver makes it complicated to formulate pharmacokinetic models (109).

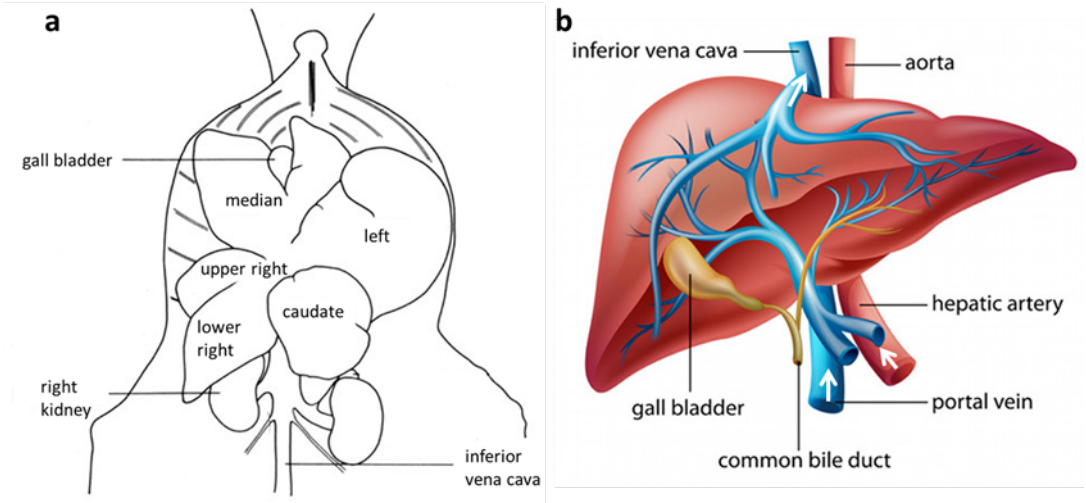

Figure 4.14: Liver anatomy and blood supply. a) A mouse liver schematic shows where the organ is located and its structure made of different lobes. b) A human liver schematic shows the blood supply of the organ. The blood is supplied by the portal vein and the hepatic artery (arrows at the bottom). The blood is processed through the liver and collected into the inferior vena cava (upper arrow). Image adapted from ref. (225).

4.2.1.2 Liver cancer and metastases

Hepatocellular carcinoma (HCC), the most common type of primary hepatic cancer, is the sixth most prevalent cancer worldwide and the third most frequent cause of cancer-related death (226). However, hepatic metastases are up to 40 times more common than primary liver tumours (227). The organs which are sites of primary malignancies and more often metastasise to the liver are part of the gastrointestinal apparatus (colon, pancreas, oesophagus), but organs such as breast, lungs, and

genitourinary apparatus can also metastasize to the liver. For instance, in the UK every year about 6 in 10,000 people are diagnosed with primary colorectal cancer (CRC), and approximately 40% of these develop liver metastases (228). In liver cancer, hepatectomy of the lobes affected by cancer is most commonly performed, as livers are estimated to be fully functional with only 25% remaining (229). However, despite technical advances, the procedure has a number of complications, such as infections, intraperitoneal haemorrhage, gastrointestinal tract bleeding and liver failure (230), and management of hepatic resection is challenging. Furthermore, hepatectomy can only be performed if the cancer is restricted to a small area of one lobe. Therefore, investigation has been done on tumour-targeted therapies with the aim of minimising hepatic surgery (231).

In order to develop new treatments for secondary liver carcinoma, over the past few decades much research has been done on the vasculature, blood supply and perfusion of colorectal liver metastases. Despite the first formulated theories suggested that the blood supply to hepatic metastases was only arterial (232), extensive experimental evidence is now available which enables us to reevaluate this hypothesis and provide evidence that primary as well as metastatic tumours in the liver receive blood supply from both the hepatic artery and the portal vein (233-237). Paku et al (235) have even suggested that the portal vein is the predominant supplier of the blood to tumours.

These findings are of crucial importance since they suggest that the optimal approach for treatment of liver metastases of colon cancer is regional rather than systemic chemotherapy (238). Indeed, the mode of delivery of chemotherapeutic agents is based upon those early reports suggesting that liver tumours primarily receive blood supply via the hepatic artery (239), hence treatment is generally administered via the hepatic artery.

4.2.2 Imaging the hepatic vasculature *in vivo*

The vasculature of the liver is unique, as the portal vein delivers approximately 75% of the blood, whilst the remaining 25% is drawn from the hepatic artery (224). This dual supply makes the quantification of liver blood flow with *in vivo* imaging

techniques, such as dynamic contrast-enhanced MRI (DCE-MRI), particularly challenging in preclinical research. DCE-MRI is currently the most common form of clinical liver perfusion imaging. It consists in the acquisition of serial MRI images before, during, and after the administration of an MR contrast agent (240). In the clinic, DCE-MRI has been successfully applied to HCC and in patients with liver metastases undergoing various therapies (241). DCE-MRI is used for qualitative diagnostic evaluation to determine tissue malignancy from arterial and portal phases (242). However, because of the limited temporal resolution, separation of arterial and venous blood supply can be challenging in small animal models of disease (243, 244). Furthermore, the liver is significantly affected by respiratory motion, hence accurately capturing the passage of a bolus of contrast agent during arterial and portal phases can be particularly challenging.

4.2.3 Aim of the study and study design

In this study, 9.4T MRI was used for tumour volume assessment in mice, to characterise the development of liver metastases over four weeks. *In vivo* MRI data were further visually compared with *ex vivo* images acquired with OPT.

The main aim of this study was to analyse the vasculature of metastatic liver and determine whether the blood supply to the tumours is mainly arterial or portal. The first step was to verify the ability of OPT to acquire information about the hepatic vasculature by imaging fluorescent compounds, as it was done in the subcutaneous tumour model showed in section 4.1. Due to the resolution of OPT, higher compared to that of MRI, the data acquired by OPT would add to the MRI data and allow better understanding of metastatic liver perfusion, particularly given the differences in blood flow between normal and tumour tissue discussed in section 4.1.1. OPT could be a valuable technique to determine whether the main blood supply to the tumours within the liver is arterial or portal. Indeed, as discussed in the previous section, pharmacokinetic modelling of livers is extremely challenging, and knowledge of how contrast agents are distributed in liver and liver tumours at micron scale would be extremely useful to easy the delivery of drugs.

4.2.4 Methods

4.2.4.1 Orthotopic liver metastases model

Human cancer cells were prepared using tissue culture techniques (described in section 4.1.3) to a concentration of $1x10^6$ per 100 µl of serum free media. A surgery suite was prepared in advance by disinfecting all surfaces. Sterile surgical drapes were placed over the operating table. All surgical instruments to be used were sterilised by autoclaving. Sterile surgical gown, mask and gloves were used at all times. Animals were brought individually into the surgical suite and anaesthetised with 4% isoflurane (Abbott Laboratories, USA) in oxygen (BOC, UK) at a flow rate of 1 L/min. Anaesthetised mice were placed on the operating table with an individual nose cone supplying 1-2% isoflurane in 0.5 L/min O_2 for maintenance of anaesthesia. The flank of the animal was swabbed with clorhexidine solution above the location of the spleen in order to sterilise the skin before operation. Pre-operative analgesia was provided through subcutaneous injection of 0.1 mg/kg buprenorphine (Vetergesic, Reckitt Benckiser, UK) just above the site of incision. Depth of anaesthesia was monitored by a paw-pinch response; surgery commenced when no pinch response was observed.

A set of surgical scissors and tweezers were used to make a ~1 cm incision through the skin above the spleen; these were then considered to be 'outside' instruments and therefore not used internally. A further set of 'internal' round-edged scissors and non-toothed tweezers were used to make an incision through the exposed muscle wall. The spleen was located and gently held in place in order to allow intrasplenic injection of cells; a fine gauge 27 g needle was introduced into the spleen and 100 µl of cell suspension injected. Care was taken to inject at a steady pressure, with correct injection noted by a paling of the spleen with no spillage of liquid into the opened cavity. Following injection, cells were allowed to wash through to the liver for 5 minutes, after which the splenic artery and vein were ligated with undyed, absorbable, coated vicryl sutures (Ethicon, Johnson & Johnson, UK) and splenectomy performed to prevent formation of intrasplenic tumours (245). The muscle wall was then sutured with PC-5 4-0 coated vicryl sutures (Ethicon, Johnson & Johnson, UK). The skin layer was securely closed using the Autoclip wound closure system (Harvard apparatus Ltd, UK), the area swabbed with clorhexadine,

and mice returned to a recovery box. Full recovery of the animals was checked before returning the IVCs to the holding room and at 24 hours post operation. One week following surgery, when wounds had completely healed, the wound clips were removed.

4.2.4.2 MRI measurements for structural analysis

The development of liver metastases over 4 weeks in 12 female *nu/nu* mice (8 weeks of age, 20-15 g) was monitored using a 9.4T MRI scanner (Agilent Technologies, CA, USA) (collaboration with Dr Rajiv Ramasawmy and Dr Thomas Roberts, UCL Centre for Advanced Biomedical Imaging). A 2-D, axial, T2-weighted, respiratory-triggered fast-spin echo MRI sequence (resolution: 0.11 x 0.11 x 0.5 mm, TR/TE: 1000/17 ms and 4 averages) provided contrast between tumour and liver tissue, as well as the major liver vasculature. Liver metastases appeared hyper-intense (Figure 4.15 A, arrows) relative to the liver parenchyma (outlined). The imaging volume was set to cover the whole liver (typically 30-40 slices).

Animals were anaesthetised using 4% isoflurane at 1 L/min of O_2, and maintained within the scanner at 1.5% at 0.5 L/min O_2. Body temperature was maintained by heated water pipes and animal physiology was monitored using a rectal probe and respiratory bellows. 3-D anatomical representations of liver and tumours was performed using Amira 5.4 (Visage Imaging, USA).

4.2.4.3 Procedures for lectin-mediated vasculature labelling and *ex vivo* imaging

At the fourth week after intrasplenic injection of human colon cancer cells, the mice imaged with MRI (6 *nu/nu* mice) received an intravenous injection of 100 µg of lectin-AlexaFluor 647 fluorophore diluted in sterile saline at neutral pH (100 µl) containing 1 mM $CaCl_2$. After 5 minutes' incubation of lectin-AlexaFluor 647 mice were anaesthetized and sacrificed by pentobarbital overdose. The anesthetized mouse was pinned onto the dissecting tray, ventral side up. Procedures for perfusion-fixation were carried out as explained in section 2.2.3. After fixation, all the livers were extracted and the lobes were separated. Individual samples were then optically cleared with BABB. Details of the clearing procedure can be found in section 2.2.4.1.

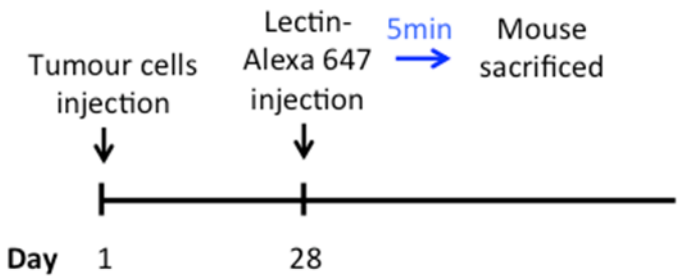

Figure 4.15: Timeline for the liver single labelling experiment

4.2.4.4 *Ex vivo* tumour imaging and image processing

The first group of samples (single labelling) was imaged with OPT with two channels: white light to obtain structural and morphological details and fluorescence, with the filter set: excitation range 620/60 nm, emission range 700/75 nm. The measurements were performed with exposure times of ~400-600 ms per projection for the AlexaFluor 647 channel. The rotation step was 0.45 degrees. The final xy resolution ranged from 6 to 8 µm, depending on the sample size. The images were reconstructed and processed as described in section 4.1.4.

4.2.5 Results

A 3-D rendering of the segmented MRI data relative to the single labelling hepatic and tumour vasculature study can be seen in figure 4.21 D: liver (red), metastases (yellow) and major vasculature (blue) were compared with OPT images. Mean (± SD) final tumour volume detected by MRI was 0.24 ± 0.02 mm^3, with a doubling rate of 4.6 ± 0.5 days. Multispectral fluorescence OPT imaging of the livers allowed visualization of metastatic tumour morphology (Figure 4.21 B) and vascular network (Figure 4.21 E) in high resolution.

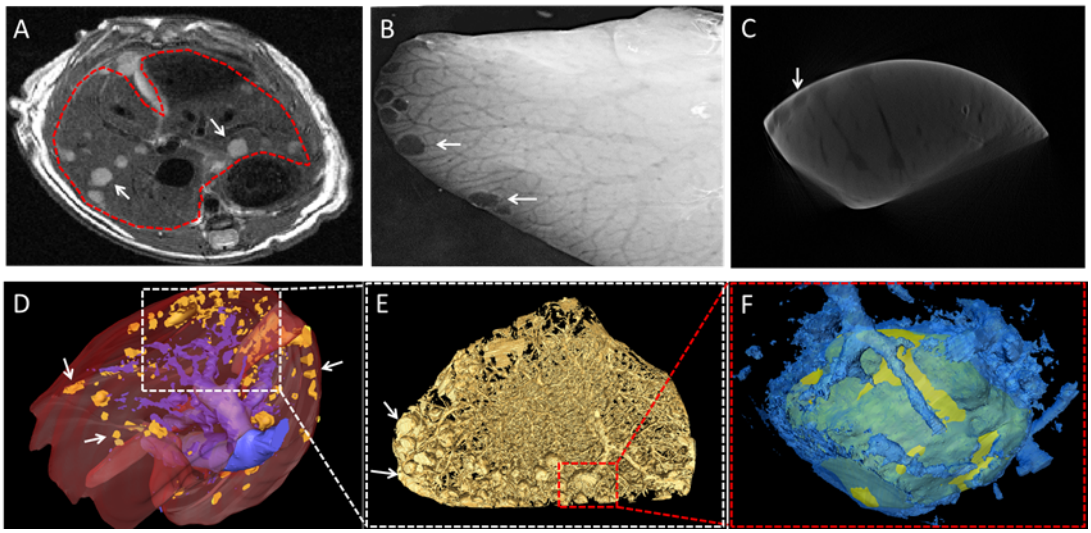

Figure 4.16: Multimodal imaging of a mouse model of colorectal liver metastases. (A, D) MRI images (B, C, E, F) OPT images. (A) Anatomical high resolution T_2-weighted MRI. Tumour deposits (arrows) appear to be relatively brighter than the normal liver (outlined red). (B) OPT raw projection of a single metastatic liver lobe. The arrows point at tumour deposits. Liver vasculature is shown. (C) Single sagittal slice of OPT reconstruction from projections (D) 3-D representation of liver (red) and metastases (yellow) from manual segmentation of the MRI. (E) OPT 3-D reconstruction of the metastatic liver microvascular architecture. (F) Zoom-in of one single liver metastasis (yellow), showing vasculature around the tumour (blue).

Figure 4.17 shows reconstructed images acquired with OPT in the metastatic liver samples with single lectin vasculature labelling. Each of the five liver samples belongs to a different mouse. The darker areas represent the tumours, and the white arrows point at vessels within the liver tumours.

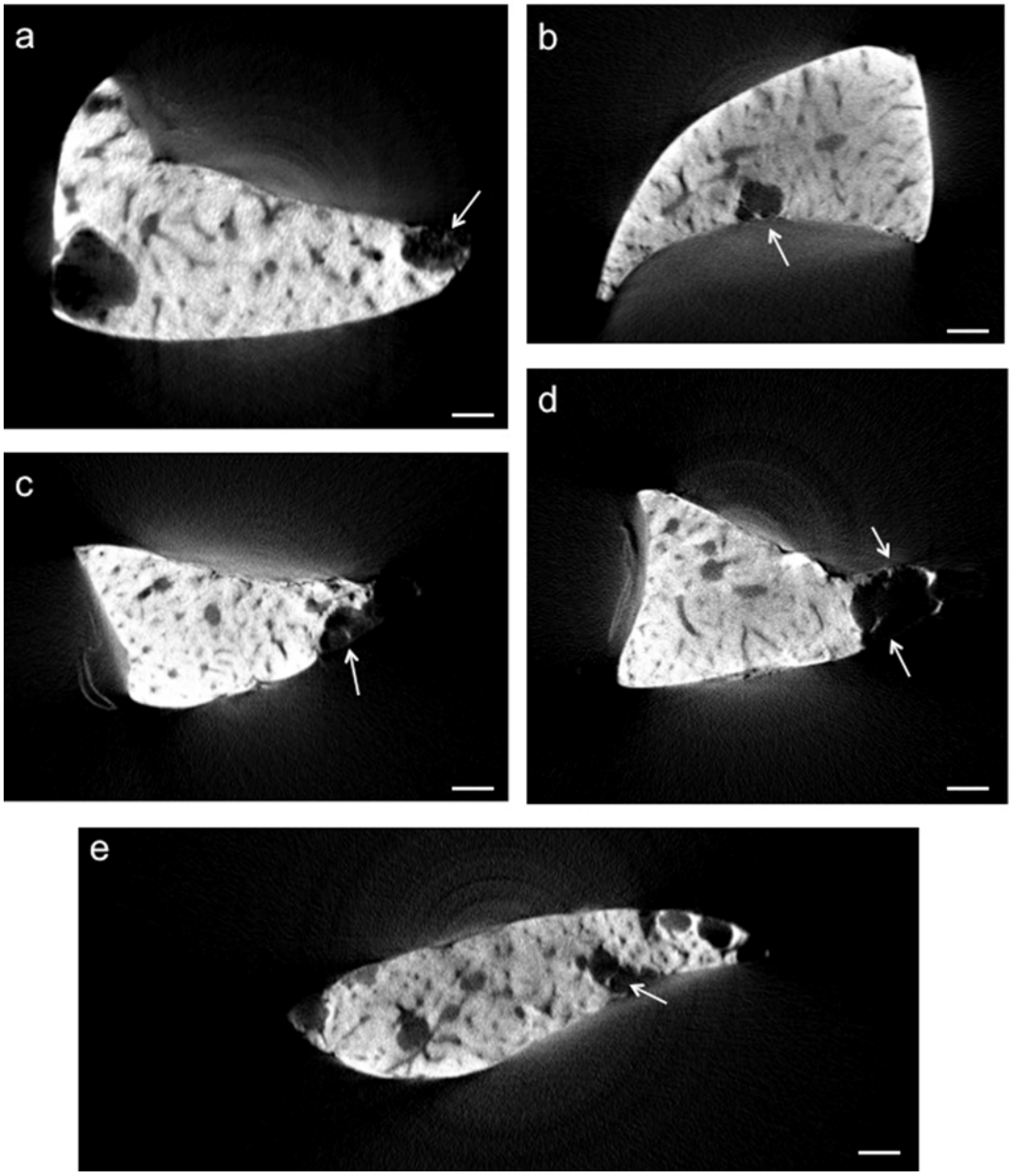

Figure 4.17: OPT reconstructed images of metastatic mouse livers. The samples were labelled with lectin-AlexaFluor 647, and the arrows point at the stained vessels within the tumours. Each image represents a liver lobe excised from a different mouse. Scale bar, 1 mm.

4.2.6 Dual labelling of hepatic vasculature

After confirming the ability of OPT to detect fluorescently labelled vessels within metastatic liver, the next step of this study was to analyse the hepatic vascular network and measure the blood supply to the metastases. This was done by using two

lectins conjugated with two different fluorophores (AlexaFluor 647 and AlexaFluor 568) to label the mouse metastatic liver vasculature.

4.2.6.1 Methods

Human colon cancer cells were injected in 6 female *nu/nu* mice as described in section 4.2.4.1, and the growth of the tumours within the livers was monitored by MRI as described in section 4.2.4.2.

4.2.6.1.1 Procedures for lectin-mediated vasculature labelling and *ex vivo* imaging

Four weeks after intrasplenic injection of tumour cells the animals received an intravenous (tail vein) injection of 100 µg of lectin from *Griffonia simplicifolia* conjugated with AlexaFluor 647 fluorophore diluted in sterile saline at neutral pH (100 µl) containing 1 mM $CaCl_2$. After 5 minutes, mice were anaesthetized and sacrificed by pentobarbital overdose. The anesthetized mouse was pinned onto the dissecting tray. An incision was made below the xyphoid process, and the thoracic cavity was exposed by cutting through the diaphragm. The lower inferior vena cava (IVC) was ligated; suture was placed around the portal vein, which was cannulated with a quick catheter (Terumo Surflo, 26G x 19 mm). The upper IVC was severed to allow blood outflow. 100 µg of lectin PNA conjugated with AlexaFluor 568 fluorophore diluted in sterile saline (200 µl) at neutral pH were injected through the portal vein via a 1 ml syringe to label the portal blood supply. 5 minutes after injections, mice were perfused-fixed. The excised livers were cleared with BABB.

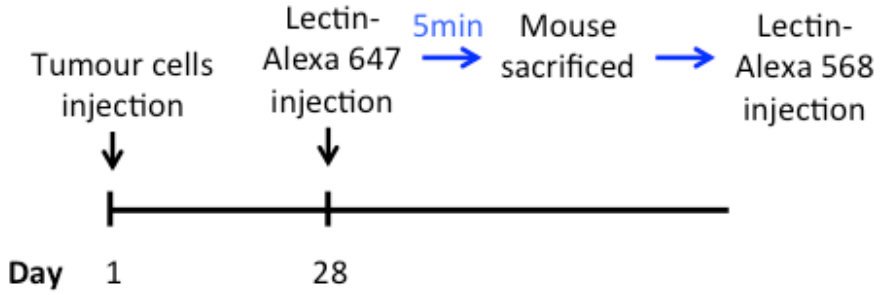

Figure 4.18: Timeline for the liver dual labelling experiment

4.2.6.1.2 Ex vivo tumour imaging and image processing

The samples were imaged with OPT with two different channels: the systemic blood supply (lectin-AlexaFluor 647) was imaged with the filter set: excitation range 620/60 nm, emission range 700/75 nm; the portal blood supply (lectin-AlexaFluor 568) was imaged with the filter set: excitation range 560/40 nm, emission LP610 nm. White light (OPT transmission mode) was used to acquire morphological information of the liver. The measurements were performed with exposure times of ~200 ms per projection for the first channel (AlexaFluor 568) and of ~400-500 ms for the second channel (AlexaFluor 647). The rotation step was 0.45 degrees. The final xy resolution ranged from 6 to 10 μm, depending on the field of view. The images were reconstructed and processed as described in section 4.1.4.

4.2.6.2 Results

The images in figures 4.19 and 4.20 show liver samples labelled with two lectins. Images 4.19 a,c and 4.20 a,c were acquired with the first channel (AlexaFluor 568) and images 4.19 b,d and 4.20 b,d were acquired with the second channel (AlexaFluor 647). Despite the low quality of the images, the vasculature labelled with AlexaFluor 647 could be visualized with OPT, as it is showed in the images, where the arrows point at the vessels. Instead, the first channel does not show a clear signal from the AlexaFluor 568 fluorophore. Vasculature can be seen in image 4.19 a, but it is not certain if this was stained with the AlexaFluor 568 fluorophore, or if the signal coming from the AlexaFluor 647, quite clear in image 4.19 b, is being detected by both the channels.

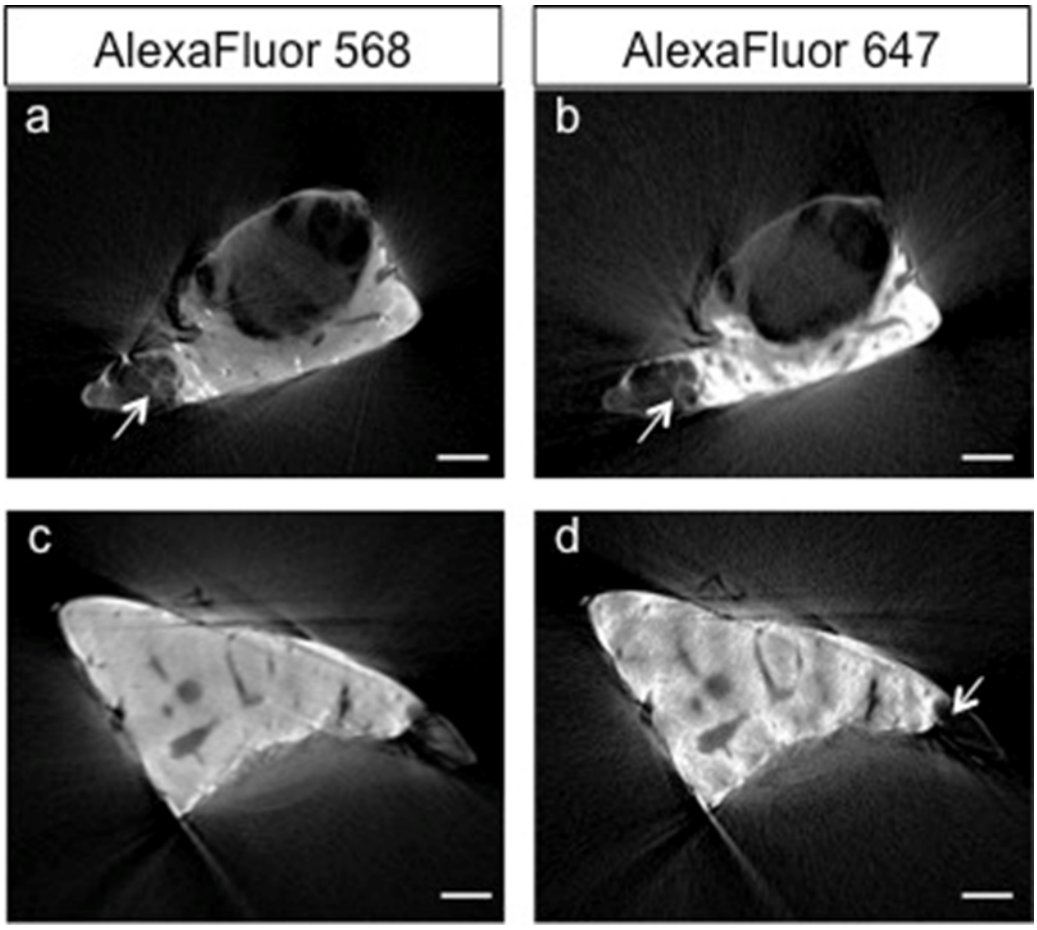

Figure 4.19: OPT reconstructed images of metastatic mouse livers. The image shows two liver lobes coming from two different mice. The arrows point at the vessels within the tumours. a,b) Same liver lobe imaged with two different channels. a, c) TXR channel was used to image the vasculature stained via the portal vein with AlexaFluor 568. b, d) AlexaFluor 647 channel was used to image the vasculature stained systemically with AlexaFluor 647. Scale bars, 2 mm.

Image 4.20 shows two slices acquired with OPT at different depth within of the same liver lobe, imaged with two different channels. As in the previous image, while the signal from the AlexaFluor 647 fluorophore could be detected (white arrows), the vessels stained with AlexaFluor 568 fluorophore could not be visualized. The reason for this in not certain. An hypothesis could be that the fluorophore bound to the vessels was not visible due to its low signal. Indeed, the vessels were difficult to segment, and this is probably due to the difficulties encountered in the process of optical clearing.

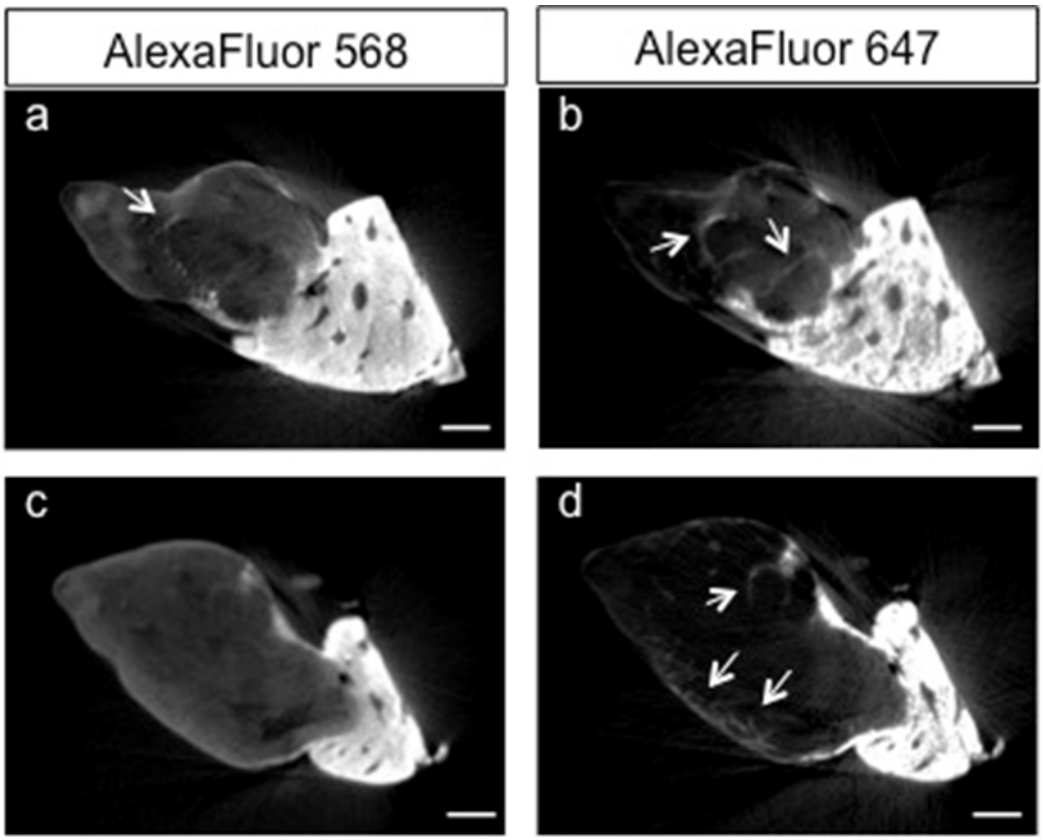

Figure 4.20: OPT reconstructed images of a metastatic mouse liver. The image shows different slices within the same liver lobe. The arrows point at the vessels within the tumours. a,b) Same slice within the liver lobe imaged with two different channels. a, c) TXR channel was used to image the vasculature stained via the portal vein with AlexaFluor 568. b, d) AlexaFluor 647 channel was used to image the vasculature stained systemically with AlexaFluor 647. Scale bars, 2 mm.

4.2.6.3 Discussion

Over the past few years, imaging of biological samples at whole-organ level has been widely investigated. As discussed in Chapter 1, imaging techniques such as OPT and LSFM, characterized by higher resolution and which overcome the *in vivo* limitations due to animal movements, have been used as validation methods for imaging modalities used in clinics, such as MRI and CT.

In this study, an orthotopic mouse model of colorectal liver metastasis was investigated *in vivo* to characterise tumour volume and vascular morphology, and *ex vivo* to analyse metastases and their vascular network in 3-D and at subcellular resolution.

The tumour vasculature was analysed with a fluorescently labelled lectin as described for tumours xenograft in 4.1.3.6. Vessels within the tumours could be visualized with OPT. However, the metastases within the liver did not show a high degree of vessels. This could be due to low level of vascularization of the tumours, or it could be an imaging issue. Indeed, the degree of optical clearing could be not high enough to allow the resolution necessary to pick up the smaller vessels.

The second part of this study focussed on dual labelling of vascular networks in hepatic metastases, with the aim of separating and analysing tumour venous and arterial blood supply. However, the analysis of dual blood supply in the liver with OPT was not possible due to the difficulties encountered in the segmentation process. Indeed, the level of noise in the OPT images was very high (Figures 4.19 and 4.20), probably due to the poor degree of optical clearing of liver tissue. This influenced the resolution of the images, which was not high enough to resolve the vessels and to assign regions to each specific lectin, hence to allow discrimination of portal and arterial supply.

Because of the complications encountered and the limitations of this study, the same samples will be processed to reverse the optical clearing and examined with a different *ex vivo* technique such as high-resolution episcopic microscopy (HREM), as it is discussed in the next section.

4.3 Analysis of liver metastases with HREM

As shown in section 4.2, liver vasculature could not be analysed *ex vivo* with OPT, mainly due to poor optical clearing of liver tissue. A more suitable technique could be HREM, briefly covered in chapter 1. With this technique, detailed greyscale images from biological structures are obtained using fluorescent dyes in a resin embedding medium such as JB4 (Polyscience) (95). As the images are obtained from the block surface of the sample as they are physically sectioned, they are inherently aligned and free of sectioning and mounting artefacts, typical of 3-D images obtained with computer-based 3-D rendering using realigned 2-D images of histological tissue sections (246). Because HREM sections the sample, and images the surface directly,

optical clearing is not necessary. This would allow imaging of tissue that is difficult to optically clear, such as liver tissue.

Some preliminary work has been done to analyse the vascular supply of metastatic liver in details with HREM with the collaboration of Dr. Tim Mohun (The Francis Crick Institute). This experiment aimed to analyse the resolution obtainable with the HREM technique in the orthotopic liver metastases model, by multimodal imaging and comparisons of datasets obtained with OPT and HREM.

4.3.1 Methods

4.3.1.1 Sample preparation and OPT imaging

Liver metastases were induced in a female *nu/nu* mouse as explained in section 4.2.4.1. As this was a pilot study aimed at testing the new HREM technique on liver samples, only one mouse was analysed. After a period of 4 weeks, the mouse was anaesthetized and sacrificed by pentobarbital overdose. Anaesthesia was confirmed and procedures for perfusion-fixation were carried out as described in section 2.2.3. Optical clearing was performed with BABB (section 2.2.4.1) and OPT imaging was done as described in section 4.1.4.

4.3.1.2 Sample preparation and HREM imaging

After OPT imaging, optical clearing of the liver was reversed by immersing the sample in 100% ethanol. After 3 washes (one each 12 hours) the sample was taken through a gradual MeOH series (10%, 20%, 30%, 40% 50%, 60%, 70%), with 2 hours per step. It was then washed for a few minutes in 70% MeOH containing 1% ammonia and then dehydrated completely (80%, 90%, 95%, 100% MeOH), 2 hours each step. A 50:50 MeOH:JB4 mix was used as a final step before infiltration for 12 hours. JB4 is a water-soluble, 2-hydroxyethyl methacrylate (HEMA), plastic resin kit generally used for preparation of embedded samples for high resolution light microscopy. 100 ml of JB4 mix are composed of 100 ml solution A, 1.25 g of catalyst, 6 ml of solution B.

After immersion in MeOH:JB4 mix, the sample was briefly rinsed in JB4/dyes mix. The dyes used are eosin B (Sigma Aldrich, 861006) and acridine orange (Sigma

Aldrich, A6014). For 100 ml of JB4 mix, 0.275 g of eosin B and 0.0563 g of acridine orange were added. The sample was left immersed in fresh JB4 mix for 7 days, after which it was embedded for imaging.

The sample needs to be completely surrounded by the embedding plastic rather than sitting at the surface of the polymerised block to ensure that the entire specimen is imaged with no loss of data from the start of the imaging. During polymerisation the sample was moved into a chosen position and orientation with the use of a stereomicroscope (Edmund Optics, 81274). After the embedding medium had set, the surplus JB4 was removed before filling the polytetrafluoroethylene (PTFA) 3-D printed mould with the fresh polymerising mix into which the sample was placed. Following positioning of the sample, a circular plastic chuck was placed into the top of the mould, with enough JB4 mix to ensure the chuck was bound onto the final polymerised block. A few drops of mineral oil were put onto the exposed surface of the polymerising JB4, especially in the central canal of the plastic chuck. The block was left polymerising in the mould for 12 hours before removing it. JB4 polymerisation is inhibited by oxygen, so any exposed surface of the mix was covered with mineral oil. A manual microtome was used to trim off enough of the cushion so that the sample was near the surface, but not exposed (~20 μm). This makes setting up the HREM imaging much easier and faster. The block was then hardened by baking it for 12 hours at 100°C. It was then allowed to cool at 4°C for 12 hours.

The embedded sample was mounted in the HREM system for imaging. The section thickness was 3 μm and the cut speed was set to 5 mm/sec. After each section a digital image of the surface of the block was captured with a CCD camera (MF, Jenoptics), which sits on the phototube of a magnification optic. Tissue morphology was visualised using GFP emission and excitation filter sets only. Indeed, eosin and acridine orange dyes in the JB4 give a very bright and broad spectrum emission across most of the wavelengths generally used for detecting individual fluorophores in microscopy. The physical resin sections were discarded through a vacuum system after imaging. A series of 2000 single digital section images with pixel sizes of 0.5 x

0.5 μm^2 to 3 x 3 μm^2 were produced and processed with ImageJ and Amira software to create a 3-D rendering (Figure 4.18 a, c) as explained in section 4.1.5.

4.3.2 Preliminary results

Figure 4.21 shows the comparison of HREM and OPT for imaging of liver structure and vasculature. OPT imaging did not allow good segmentation of the liver vasculature (Figure 4.21 b) mainly due to the poor level of optical clearing obtained in liver tissue, as discussed in section 4.2. The larger vessels were much easier to resolve on HREM images (Figure 4.21 a, c), which had bright eosin signal throughout the whole of the vasculature, as the eosin filled the entire lumen. Figure 4.21 d shows a single metastasis within the liver and allows better investigation of blood supply to the tumour. However, the vasculature cannot be identified in the image acquired with OPT.

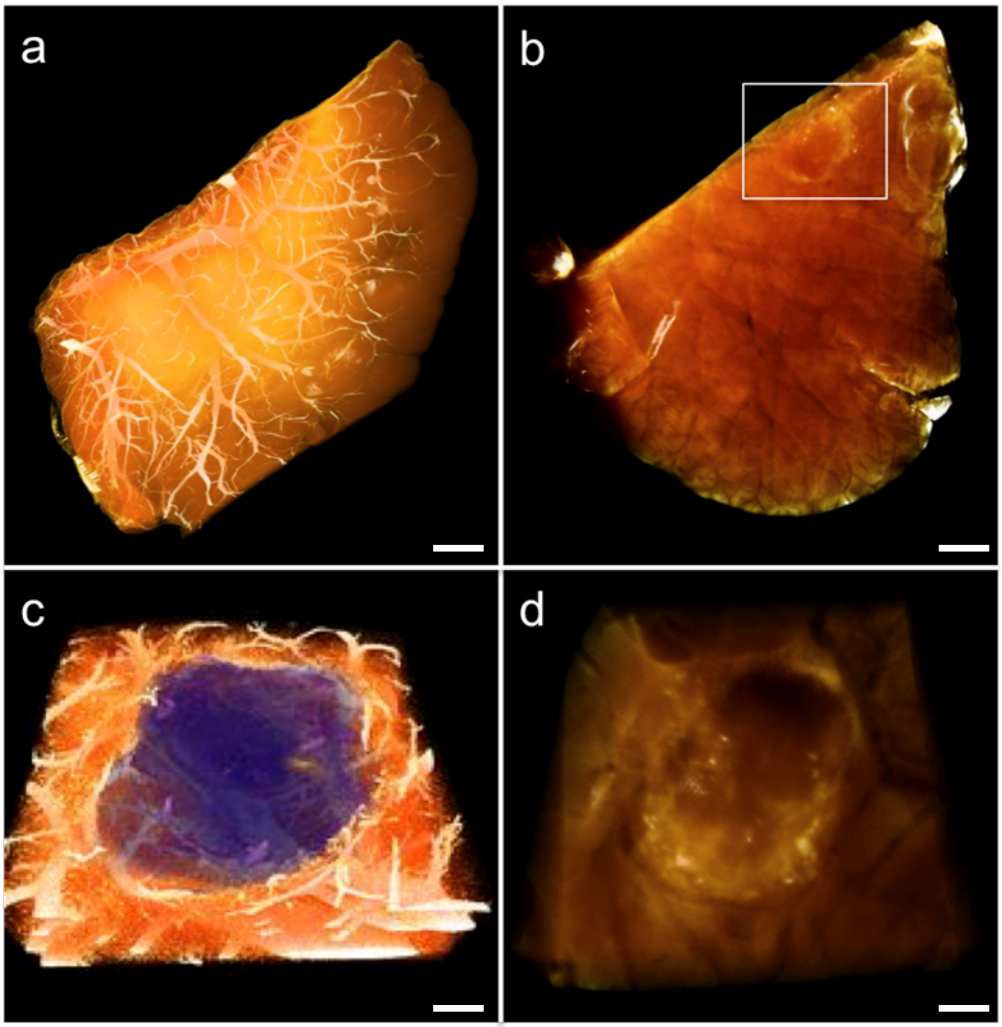

Figure 4.21: Multimodal imaging of liver metastases. a,b) Whole mouse liver lobe imaged with HREM (a) and OPT (b). The white rectangle indicates a single metastasis, which is zoomed-in and shown in images c and d. c) Blow up image of a), acquired with HREM. The tumour is shown in purple, against the surrounding healthy tissue in orange. d) OPT blow up image from b. The vasculature around the tumour cannot be distinguished clearly. Scale bar, 1 mm and 300 μm (blow up).

4.3.3 Discussions and future work

After having assessed with this pilot study that HREM is a suitable *ex vivo* technique for 3-D liver vascular network imaging, minor adjustments to the embedding protocol will be done. Indeed, when first developed HREM was mainly used to image small samples such as mouse embryos or embryo organs (95, 247). The embedding steps for bigger organs are slightly different in terms of timing. For instance, in this study the liver samples were left in JB4 mix for 7 days prior to embedding, while the optimal time for embryos is 3 days (247). For better resin

infiltration, the liver samples could be immersed in the JB4 mix for longer times. Also, for better dehydration the immersion in series of different percentages of MeOH could be prolonged. In summary, as discussed in Chapter 1, processes such as optical clearing and resin embedding for HREM have been developed only recently so they are still relatively new. Since they strongly depend on the type and size of tissue, many adjustments can be made to the protocols.

The next step of this study will be to fluorescently label the vasculature to investigate the hepatic dual blood supply. Once acquired, vascular architecture information could be used to create mathematical models of blood flow in hepatic metastases, with the aim of improving existing treatments or developing new drug delivery approaches.

4.4 *In situ* optical clearing of whole intact liver

4.4.1 Research rationale

Optical clearing, introduced in Chapter 1, is the process used to render tissue optically transparent with the aim of acquiring physiological and structural information deep in tissue without damage. As explained in Chapter 1, many techniques have been developed to achieve tissue transparency. Each one of these techniques is based on a different approach: lipids extraction and hydrogel embedding to stabilize tissue structure (CLARITY) (68), dehydration and additional lipid solvation by refractive index matching (BABB, 3DISCO, iDISCO) (57, 59, 248), and hyperhydration and lipid removal by detergents (Scale, CUBIC) (66, 72). However, the feature that is common to all techniques is immersion: after extraction, samples are submerged in different solutions until optically clear. This approach is limited by the sample size: large samples can take weeks or even months to clear.

The aim of this study was to develop a new methodology for *in situ* clearing, building upon previous techniques such as CUBIC (clear, unobstructed brain imaging cocktails) (72) and PARS (perfusion-assisted agent released *in situ*) (249). As in the PARS approach, here whole-organ clearing is facilitated using systemic circulation to directly deliver clarifying agents, which were the two reagents used for

clearing in the CUBIC technique. All steps, including preservation and clearing, are performed *in situ* prior to tissue extraction. This approach was applied to the analysis of perfusion in both healthy and metastatic livers.

4.4.2 Methods

The present study was done in collaboration with Dr Thomas Roberts and Dr Rajiv Ramasawmy, who helped recording the *in situ* liver perfusion.

A female *nu/nu* mouse was anaesthetized and sacrificed by pentobarbital overdose. After confirmation of anaesthesia, the mouse was pinned onto the dissecting tray, the thoracic cavity was exposed by cutting through the diaphragm, and the lower IVC was ligated; suture was placed around the portal vein, which was cannulated with a quick catheter (Terumo Surflo, 26G x 19 mm). The upper IVC was severed to allow blood outflow. A peristaltic pump (Watson Marlow, 5058) was connected to the cannula inside the portal vein and heparinized PBS (20 ml; 37 °C) was administered for liver blood clearing at a flow rate of 2 ml/min to simulate natural blood flow. After the complete drainage of blood (Figure 4.22 b), 20 ml of 4% formaldehyde solution was administrated. Formaldehyde was also administrated intracardially to impede whole body degradation for 48 hours.

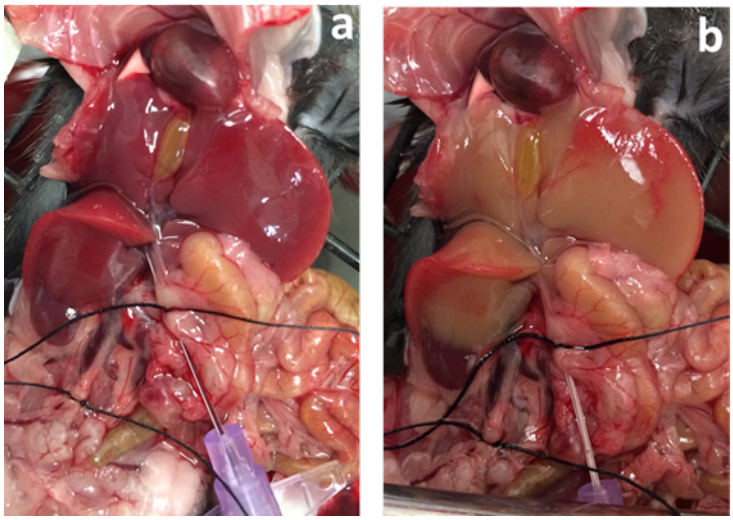

Figure 4.22: Perfusion-fixation of mouse liver. After catheterization of the portal vein (purple catheter) and severing of the upper IVC (a) the liver was perfused-fixed with saline and PFA (b). The images show how the pigment is removed from the liver by outflushing of blood.

After perfusion-fixation, the perfusion tray was filled with 2L of CUBIC reagent 1 at 37°C creating a closed-loop for 24 hours' perfusion-clearing of the whole liver. Reagent 1 includes N,N,N',N'-tetrakis(2-hydroxypropyl)ethylenediamine, Triton X-100 and urea. This first solution does not achieve high tissue transparency as its refractive index does not match the refractive index of the tissue.

24 hours of treatment resulted in a highly though not completely transparent liver (Figure 4.23 a). Also, the liver was slightly swollen. Reagent 1 in the perfusion tray was then replaced by 2 L of reagent 2 warmed to 37 °C and developed by modification of reagent 1, more specifically by adding a high concentration of sucrose, which increases the refractive index of the solution to match the tissue refractive index. Also, in reagent 2, the N,N,N',N'-tetrakis(2-hydroxypropyl)ethylenediamine is substituted by 2,2',2"-nitrilotriethanol. Thereafter the mouse was perfused for further 24 hours, making sure to arrest the perfusion pump while switching between the two reagents to avoid the introduction of air bubbles which might disrupt the vasculature. The higher percentage of sucrose contained in reagent 2 increased the reagent RI, in turn increasing light transmittance due to better matching with the tissue RI. Figure 4.23 b shows the cleared liver at the end of the total 48 hours' perfusion.

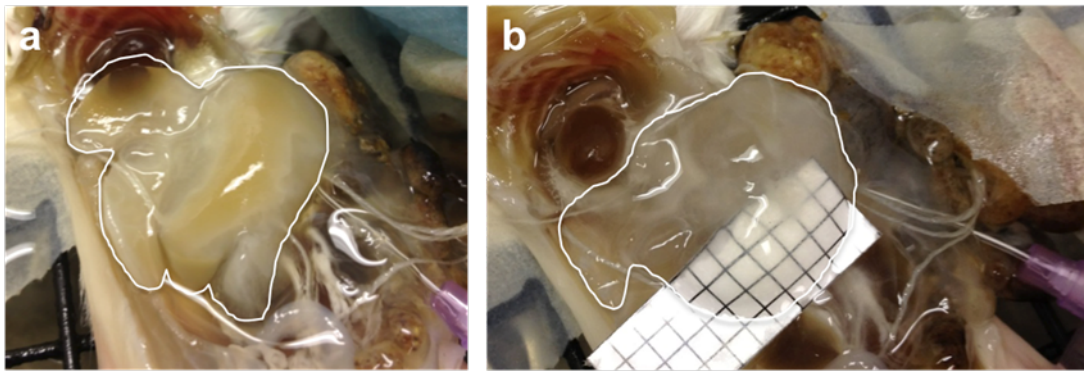

Figure 4.23: *In situ*-CUBIC clearing of whole liver. The liver is indicated with a white line. a) The liver is cleared but not transparent after perfusion of reagent 1 for 24 hours. b) The liver is optically cleared: it appears completely see-through after perfusion of reagent 2 for 24 hours.

After 48 hours, the pump was disconnected and the perfusion stopped. Two different dyes were injected consecutively with a 50 ml syringe connected to a syringe pump (Harvard apparatus, PHD 2000) through the portal vein to study and record the

perfusion of the liver (Nikon COOLPIX L31), figure 4.24. The flow rate for injection was 2.5 ml/min.

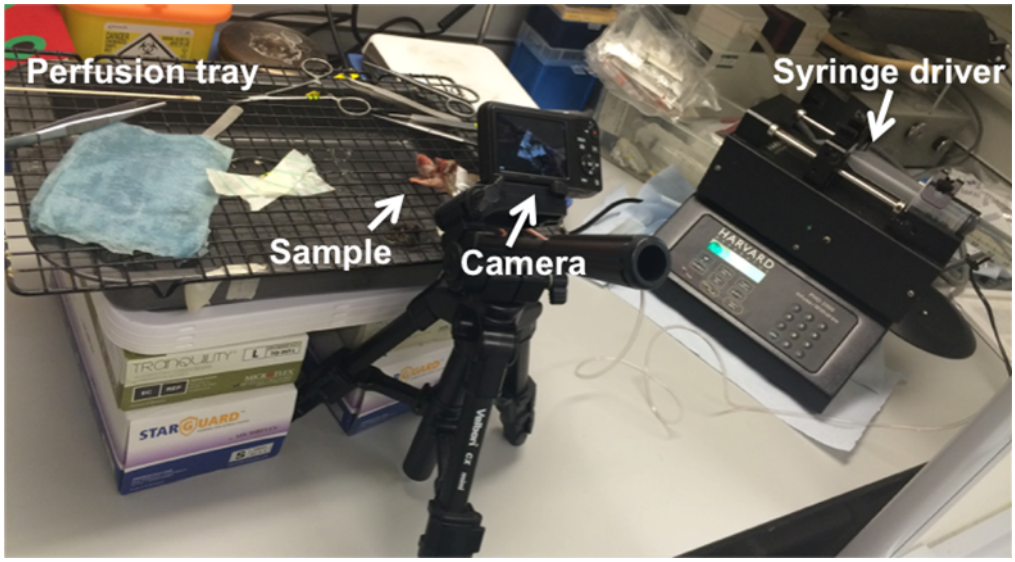

Figure 4.24: Experimental setup for recording *in situ* liver perfusion.

At first, 50 ml of 2% 2,3,5-Triphenyltetrazolium chloride (TTC, Sigma Aldrich, T8877) (1g TTC diluted in 50 ml PBS) was injected in the liver and the perfusion of the solution thought the hepatic vascular network was recorded. Thereafter, 50 ml of Evans Blue solution (or T-1824, Sigma Aldrich, E2129) was perfused. Prior to injection, Evans Blue was diluted with PBS at a concentration of 2 g/100 ml with 4% bovine serum albumin (BSA, Sigma Aldrich, A2058).

The colourless TTC is enzymatically reduced to a red product (1,3,5-triphenylformazan or TPF) by various dehydrogenases when in contact with living tissue. However, the tissue in this experiment was no longer viable, hence the enzymes had denatured, causing TTC to remain transparent and not allowing the view and recording of the solution diffusing through the liver and of the organ being perfused. The experiment was consequently repeated replacing the TTC with a green food dye, principally made of glycerine, spirulina concentrate and curcumin (Figure 4.25).

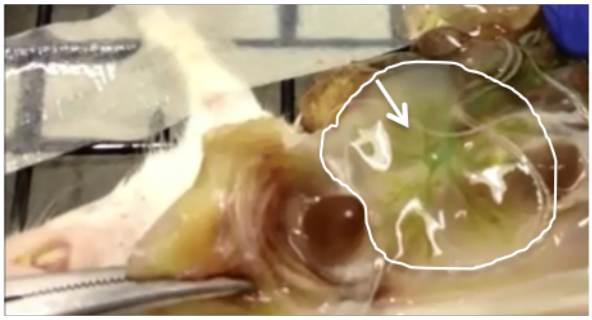

Figure 4.25: Hepatic vasculature stained after in-situ clearing. The liver is indicated with a white line. After 48 hours of perfusion-clearing, a green food dye was perfused through the portal vein to analyse perfusion in the liver (arrow).

The CUBIC *in situ* clearing protocol allows a high degree of transparency in a whole liver. Based on the CUBIC established technique and inspired by the PARS method for whole body clearing, the CUBIC *in situ* clearing protocol is the first approach for *in situ* clearing of a single isolated organ.

While sample clearing with immersion in CUBIC solutions requires 2 weeks for completion, clearing with *in situ* CUBIC can be completed in 48 hours. Indeed, passive diffusion, typical of traditional passive clearing approaches such as CUBIC, is slow and prevents high degree of clearing in large volume samples. *In situ* CUBIC differs from the classical clearing methods mainly in the way the clearing agent is delivered. Indeed, while generally samples are immersed in clearing solution, which is slowly absorbed by the tissue, in the *in situ* CUBIC approach the clearing reagents are administered from the inside of the organ (injected directly in the vessels) using perfusion, as it was done in PARS (66) for the whole organism.

This study is still at an early stage of development: several methods have been established and several are being optimized. For instance, one issue that arises when switching from clearing solution to the staining dyes is the air introduced in the cannula used to catheterize the portal vein, and this results in the formation of bubbles that are perfused through the vasculature and disrupt it. One possible solution would be to temporarily submerge the whole mouse, hence the cannula, in the clearing solution inside the perfusion tray and proceed with the switching, preventing the formation of bubbles. Another difficulty relies in the catheterization of the portal vein itself. Indeed, despite securing the cannula by ligation to the distal

part of the portal vein, micro movements during perfusion-clearing and during the set up for recording can cause displacement of the cannula, with the potential rupture of the vein. To minimize the risk of motion, the cannula could also be secured to the vein at another point, closer to the point of vessel perforation. Furthermore, catheterization of the descending aorta could be performed to provide a second way of perfusion in case the portal vein gets damaged. However, this would make the whole system more delicate hence difficult to move if needed. These are all minor issues that are currently being addressed.

With this *in situ* clearing technique a high level of transparency can be obtained in liver tissue. The hypothesis was that it could be used in the study of liver structure and vasculature with OPT, which was tested in samples cleared with BABB but did not obtain good results due to the poor tissue clearing. However, after optical clearing with *in situ* CUBIC technique the sample lost its original rigidity and became so soft and gelatine-like that it could not be embedded in agarose for OPT imaging, as it folded on itself.

4.4.3 Conclusion

This section describes the methods for *in situ* whole liver clearing. In this approach, the existing liver vasculature network was used to introduce clearing agents directly to tissue by performing the entire fixation and clearing procedure in situ. The main advantage of this procedure is the high degree of transparency achieved. Also, this being similar to the level of other clearing techniques such as CLARITY (69, 249), this method allows a remarkable reduction of clearing times compared to passive clearing methods such as conventional CUBIC (72). Furthermore, *in situ* clearing allows reduction of tissue expansion during clearing (249). Finally, this method is cost-effective relative to the original CLARITY process (249).

The main application for which the *in situ* CUBIC technique was intended in this study is the *ex vivo* analysis of liver perfusion, which could be used as a validation method for DCE-MRI perfusion studies. Moreover, despite not including analysis of fluorescence and measurement of protein loss, this is indeed possible, and the *in situ* CUBIC clearing technique could be also used for 3-D immunostaining of samples.

As OPT cannot be used for imaging specimens cleared with the approach described in this section, the optically transparent and fluorescently labelled samples would be visualized with confocal and 2P microscopy.

4.5 Summary

In this work, fluorescence optical projection tomography was applied to the analysis of cancerous tissue and allowed the creation of unprecedented quantitative, 3-D measurements of whole tumours, at cellular resolution. This *ex vivo* imaging technique uses optical clearing in combination with vascular labelling agents to increase penetration depth and image quality. As shown in Chapter 3, two different vasculature labelling techniques were tested with the aim of studying tumour vascularization. These are radiopaque polymer injection media and fluorescent compounds. The second approach was found to be superior, as it allowed better preservation of vascular architecture. The high signal-to-noise ratio resulting from optical clearing enabled measurement of whole tumour samples, up to 1 cm in diameter, with isotropic resolution.

The next step of this study was the application of the imaging method to preclinical research, to investigate the effect of OXi4503, the diphosphate prodrug of combretastatin, on colorectal tumours. A quantitative analysis of the tumour vascular network was performed. A significant reduction of the tumour vessel volume and an increase of vessel size were detected 48 hours after injection of Oxi4503. Changes in tumour vascular networks were also detected as early as 2 hours after administration of the VDA. The unprecedented 3-D insights into treated tumours were coherent with previous studies done with different imaging techniques (214).

In a separate study, the lectin labelling approach for vasculature staining was applied to the study of perfusion in metastatic livers. Despite some initial results showed that fluorescently labelled lectins could be visualized in hepatic tumours, the resolution of the OPT system and issues with optical clearing did not allow the analysis of blood supply to the tumours within the liver. A preliminary analysis showed that HREM could be a more suitable imaging technique for this study.

Finally, a new clearing approach was developed to clarify liver tissues *in situ* and achieve a higher degree of transparency in order to study liver perfusion.

In preclinical research and drug development, OPT represents a link between current *in vivo* imaging methods and classic 2-D histology. This *ex vivo* imaging approach together with classic histology and mathematical modelling enables a detailed analysis of tumour biology and drug behaviour at a microscopic scale. The comprehensive information about these tangled mechanisms which will be obtained with the aid of *in silico* models of vasculature, simulating the delivery of anti-angiogenic therapies, could help to improve the existing cancer treatments and to accurately design new anti-cancer drugs. Furthermore, since emerging fluorescently labelled compounds are becoming more relevant for clinical applications regarding tumour diagnosis, *ex vivo* imaging approaches such as OPT could be used in the future for 3-D analysis of human tissue samples providing more extensive information than the currently used conventional histology methods (250).

Chapter 5: Conclusions

5.1 Summary and future work

The primary aim of this thesis was to develop new methods to analyse organs and tumour structure as well as tumour response to therapy with high resolution. Recent developments in *ex vivo* optical imaging have allowed whole-tumour analysis with microscopic resolution (106, 251). This thesis describes the development and first application of OPT, used in combination with tissue optical clearing methods, to obtain high resolution 3-D images of internal structures in whole tumours. More specifically, this work is the first demonstration of the use of OPT to visualise complete tumour blood vessel networks and analyse drug delivery on a microscopic scale.

Several optical imaging techniques, including OPT, use optical clearing to reduce light absorption and scattering in tissue and therefore increase light penetration depth and image quality (54). In this thesis, a novel method for quantifying light attenuation in tissue was developed. This was based on spectrometric analysis, and was used to compare the degree of transparency achieved by a number of techniques. This was useful to identify the most suitable approach for the application which represents the focus of this thesis. The clearing methods investigated included pBABB, which was developed in this thesis and is a modification of an existing technique for optical clearing (BABB). pBABB aims at optimizing optical clearing through the use of reagents, such as hydrogen peroxide, which act on the tissue pigments to reduce light absorption and solvents, such as dimethyl sulfoxide, that increase the penetration of clearing agents within the tissue (60). This method to quantify the efficacy of optical clearing protocols showed that the degree of clearing obtained with pBABB methodology is greater than that given by established techniques such as CLARITY (163).

Optical clearing was combined with a new approach for imaging vascular networks, in three dimensions, by labelling blood vessels wish exogenously administered, fluorescent agents. In Chapter 3, several approaches for labelling vasculature were

compared, including microvascular casting and fluorescently labelled lectin. It was found that labelling with fluorescent lectins was preferred over perfusion with radiopaque polymer, due to the multiple technical challenges that microvascular casting presented (such as, for example, labelling discontinuities). However, the choice of fluorophore conjugated to the lectin appeared to be crucial to label the vascular architecture. Indeed, several fluorophores were tested, and those emitting in the green part of the spectrum could not be detected with OPT, due to intrinsic properties of the biological tissue described in Chapter 3.

Furthermore, OPT was compared with μCT, to analyse the ability of both techniques to image vascular networks in mouse organs and tumours. For this purpose, mouse brains were perfused with a radiopaque resin (Microfil) and imaged with the two *ex vivo* techniques. The comparison was made possible by the aid of computerized analysis.

The combination of several sources of image contrast (such as autofluorescence) allowed the acquisition and analysis of various aspects of tumour pathophysiology, including tumour morphology, vessel networks and drug efficacy. Three-dimensional analysis of these data was undertaken with a novel set of custom-developed image analysis algorithms. These algorithms appeared to work robustly, and can produce complete tumour vascular networks in a graph (node and segment) format.

This vascular imaging approach was then applied to the investigation of the response of xenograft colorectal carcinoma to a vascular disrupting agent (Oxi4503) at several time points post-dosing (Chapter 4). Oxi4503 selectively targets tumour vasculature, resulting in extensive central necrosis at 24 hours following administration (187), and reductions in perfusion have been observed *in vivo* as early as 90 post-dosing. The effects of Oxi5403 could be detected in this study at 2 hours post-administration, evidenced by a significantly reduced vessel volume and number of vessel segments, particularly in the central region of the tumours. Moreover, the remaining vessels showed an increased radius, sign of a higher vascular permeability. Both single and dual-lectin approaches were developed: in the single-lectin case, one fluorescent lectin was used to evaluate vasculature in individual mice, at a single timepoint; in the dual lectin case, two lectins were administered, with different fluorophores

attached, and at different timepoints. The latter set of experiments allowed two timepoints (pre- and post-dosing) to be evaluated in the same mouse, providing much greater specificity. This was the first demonstration of a dual-fluorophore study of this kind, and demonstrated the potential of OPT of tumour blood vessel networks for detecting regional response to vascular targeting therapies.

In Chapter 4 the use of OPT as a method to validate *in vivo* imaging techniques (such as MRI) at a microscopic level was also investigated. An orthotopic mouse model of colorectal liver metastasis was studied *in vivo* by MRI to characterise vascular development and *ex vivo* by OPT to analyse metastases and their vascular network in 3-D and at cellular resolution. However, OPT was found to be unsuitable for analysis of liver vasculature due to limitations associated with optical clearing in liver tissue, which made the vessels hard to segment. Indeed, the level of optical clearing obtained in the liver samples was not as high as that of tumours, probably due to the high content of iron in the liver tissue. As an alternative approach, one sample was also imaged with HREM to compare the two imaging techniques in liver tissue. This pilot study demonstrated that HREM is potentially a better for 3-D liver vascular network imaging, due to non-reliance on tissue clearing (which also potentially reduces tissue distortion) and inherent vessel lumen contrast afforded by the infiltration of resin.

The methods developed in this thesis will find application as a preclinical tool for studying the pathophysiology of tumours and their response to antivascular treatment. Indeed, the tumour data gathered in this study by 3-D imaging of microvascular networks in colorectal primary and metastatic cancer could help understanding functional properties of the microcirculation in cancerous tissues and could prove useful in colorectal cancer treatment.

5.2 Final conclusions

The aim of this thesis was to develop new tools and techniques for *ex vivo* investigation of healthy and diseased mouse tissues. The methods developed here include the use of fluorescent compounds, optical clearing approaches and *ex vivo*

optical imaging techniques. These methods, which were mainly applied to a preclinical model of colorectal carcinoma, offer a novel approach to analyse the response to therapy of complete tumours, in three dimensions, and with cellular resolution.

Appendix: Development of a selective plane illumination microscope

A.1 Research rationale

In conventional and confocal microscopy as well as in optical projection tomography, whenever a single plane of a sample is observed, light is shone through the whole specimen which is in this way highly photobleached and photodamaged (92, 252). On the contrary, as extensively described in Chapter 1, in single plane illumination microscopy only the focal plane is illuminated, preserving fluorescence of the cells whose image is not registered. Part of this thesis was focussed on building a single plane illumination microscope to reduce sample photobleaching as well as to overcome the other main limitations of optical projection tomography and achieve 3-D images in small live animals with cellular resolution. The main advantage of a custom built imaging system over a commercially released one is the customizability, hence the possibility to build the system according to the specific biological needs.

A custom built SPIM was implemented according to the OpenSpim (253), an open access platform for the control of different types of light sheet microscopes. Open access to design and operational protocols of imaging systems such as SPIM is essential for further development of the system itself as well as new biological applications.

A.1.1 Microscope assembly

The setup built is shown in figures A.2 (SolidWorks simulation) and A.3 (real system). Parts for the hardware are grouped and listed in the tables below (Tables A.1-A.7).

Table A.1 Illumination parts			
Component	**Model number**	**Description**	**Manufacturer**
Laser	Cube 488-50 C Cube 730-30C	Fixed wavelengths lasers	Coherent
Heat sink	--	Metal	Self-made
Alignment disk	DG05-1500-H1-MD	Mounted Frosted Glass Alignment Disk	Thorlabs

Table A.1: Illumination parts

Table A.2 Opto-mechanical parts			
Component	**Model**	**Description**	**Manufacturer**
Optical breadboard	MB3045/M	300 mm x 450 mm x 12.7 mm, M6 Taps	Thorlabs
Optical rails	RLA300/M RLA150/M RLA075/M	300, 150 and 75 mm rails	Thorlabs
Rail carriers	RC1	25.4 mm x 25.4 mm	Thorlabs
Vertical slit stilts	For mirrors, lenses, adjustable slit	To elevate components from the rail carriers	Self-made (3-D printed)
Adjustable slit	VA 100/M	To adjust the thickness of the light sheet	Thorlabs
Optic mount	LMR05/M	Fixed mount	Thorlabs
Metric rotation mount	RSP1X15/M	360° rotation	Thorlabs
Kinematic mirror mount	POLARIS-K1	25 mm diameter	Thorlabs

Table A.2: Opto-mechanical parts

Table A.3 Illumination axis optical parts			
Component	**Model**	**Description**	**Manufacturer**
Broadband dielectric mirror	BB1-E02	25 mm	Thorlabs
Achromatic doublet (beam expander)	AC127-050-A-ML	50 mm, for 488 nm laser	Thorlabs
Achromatic doublet (beam expander)	AC127-025-A-ML	25 mm, for 488 nm laser	Thorlabs
Achromatic doublet (beam expander)	AC127-025-B-ML	50 mm, for 730 nm laser	Thorlabs
Achromatic doublet (beam expander)	AC127-025-B-ML	25 mm, for 730 nm laser	Thorlabs
Cylindrical achromatic	ACY254-050-A ACY254-050-B	50 mm	Thorlabs
Objective lens for illumination	UMPLFLN 10XW	Water dipping, 10X	Olympus

Table A.3: Illumination axis optical parts

Table A.4 Chamber parts			
Component	**Model**	**Description**	**Manufacturer**
Sample chamber	--	Acrylic	Self-made (3-D printed)
Chamber holder	--	Metal	Self-made (3-D printed)
Objective holder ring	--	Metal	Self-made (3-D printed)
O-rings	NBR 70, 20x3mm	For watertight seal around objectives. Nitrile	Any

Table A.4: Chamber parts

Table A.5 Detection axis optical parts			
Component	**Model**	**Description**	**Manufacturer**
Objective lens for detection	UMPLFLN 20XW	Water dipping, 20x	Olympus
Detection axis holder	--	60 mm diameter	Self-made (3-D printed)
Infinity space tube	--	104 mm length, 60 mm diameter	Self-made (3-D printed)
Fluorescent filters	XF3092/25 3RD750LP	500ALP 25 mm diameter 750LP 25 mm diameter	Omega
Filter holders	--	Metal	Self-made (3-D printed)
Tube lens for detection	U-TLU	--	Olympus
Magnifying camera mount	U-TCV1X & U-CMAD3	1x	Olympus
Magnifying camera mount	U-TV0.5XC-3	0.5x	Olympus

Table A.5: Detection axis optical parts

Table A.6 4-D motor system parts			
Component	**Model**	**Description**	**Manufacturer**
USB-4D-Stage	USB-4D-Stage	4 motors	Picard-Industries
Pulley system	--	For the motor arm	Self-made
O-ring	Any	Nitrile	Any
Ball bearing	NSK 6001Z	28 mm diameter	Any

Table A.6: Detection axis optical parts

Table A.7 Electronics			
Component	**Model**	**Description**	**Manufacturer**
Computer	--	--	Dell
Camera	Hamamatsu ORCA Flash 4.0		Hamamatsu
USB to serial adaptor	Any	--	Tripplite
USB cables	Any	--	Any
USB led lamp	Any	--	Any

Table A.7: Electronics

The 1 mm diameter cone beam from the laser (Coherent CUBE 488-50C and Coherent CUBE 730-30C, Coherent, Inc., CA, USA) [Figure A.2, a] is directed by two mirrors into a beam expander (25 mm and 50 mm achromatic doublets) [b]. The resulting 2 mm diameter cone beam reaches the cylindrical lens [d] through the vertical slit [c]. The cylindrical lens shapes the beam in a sheet of light. An optical telescope (50 mm and 25 mm achromatic doublets) [f] focuses the light from the corner mirror [e] into the illumination objective [g]. The optical arrangement is fixed. The sample holder (glass capillary or syringe) is based on a rotation system, containing a stepper 4 axis motor (Picard Industries, NY, USA, USB-4D-Stage, three translational and one rotational stages) [i] with a custom made sample holder. The stages move the sample along three dimensions and rotate it around its vertical axis (Figure A.1).

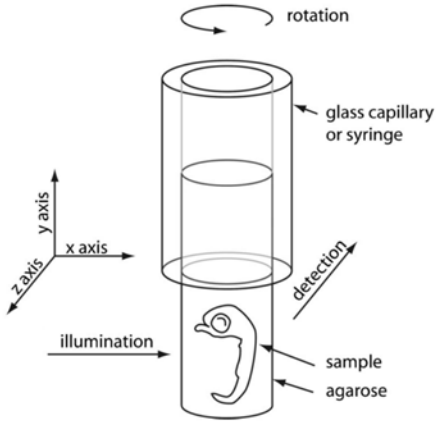

Figure A.1: Sample holding and handling. The specimen, embedded in a block of agarose and hold by a syringe or glass capillary, is translated in three dimensions and rotated around its vertical axis. Illumination and detection axes are perpendicular. The image was adapted from ref. (254).

The pulley system attached to the sample holder arm for sample rotation was self-made [l]. The sample is embedded in a block of agarose, a biocompatible gel which enables live imaging over a few days, and it is immersed in water or PBS. The imaging solution fills a 3-D printed acrylic sample chamber [m] that holds the water dipping objective lenses for illumination (Olympus, UMPLFLN 10XW) and detection (Olympus, UMPLFLN 20XW) [h]. The main advantage of this setup with water dipping lenses, which cannot be employed in case of cleared samples since the chamber would have to be filled with clearing solution, is that there are no additional glass surfaces between the sample and the detection axis.

The metal holder for the acrylic sample chamber [n] was custom-designed and 3-D printed. The imaging unit consists of a 3-D printed infinity space tube [o] that defines the distance between the detection objective and its tube lens. It contains a custom-made filter slide [p] for fluorescent emission microscopy filter (Omega, 488 nm, 25 mm XF3092/25 or/and Omega, 730 nm, 25 mm 3RD750LP) which blocks the excitation light and transmits the fluorescence from the sample. At the sample side of the lens tube we may optionally attach a 0.5x or 1x magnifying camera mount [q] depending on the sample size hence the required FOV. Finally there is a complementary metal oxide semiconductor (CMOS) scientific camera (Orca Flash 4.0, Hamamatsu, 2048x2048 pixel resolution, frame rate: 30 f/s at full resolution) at the imaging side [r]. The microscope is controlled by a computer running μManager

(255) on the Fiji platform. Image analysis is performed by the same computer used for image acquisition. The minimum requirements for the SPIM computer hardware include a dual-core central processing unit and a discrete graphics processing unit. The computer used was with a Intel Xeon E5645 CPU and was running a Windows 7 Professional 64-bit edition operating system.

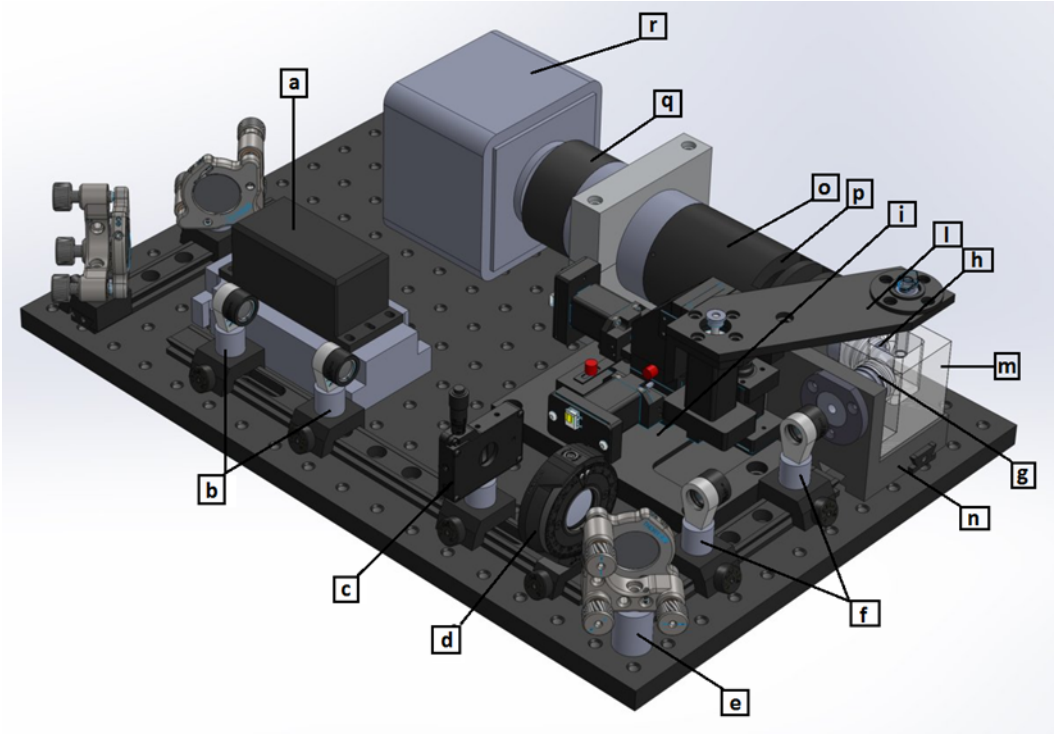

Figure A.2: Schematic of the openSPIM setup simulated with SolidWorks. [a] laser, [b] beam expander, [c] vertical slit, [d] cylindrical lens, [e] corner mirror, [f] optical telescope, [g] illumination objective, [h] detection objective, [i] stepper motor, [l] sample holder arm, [m] acrylic chamber, [n] chamber holder, [o] infinity space tube, [p] filter slide, [q] magnifying camera mount, [r] camera.

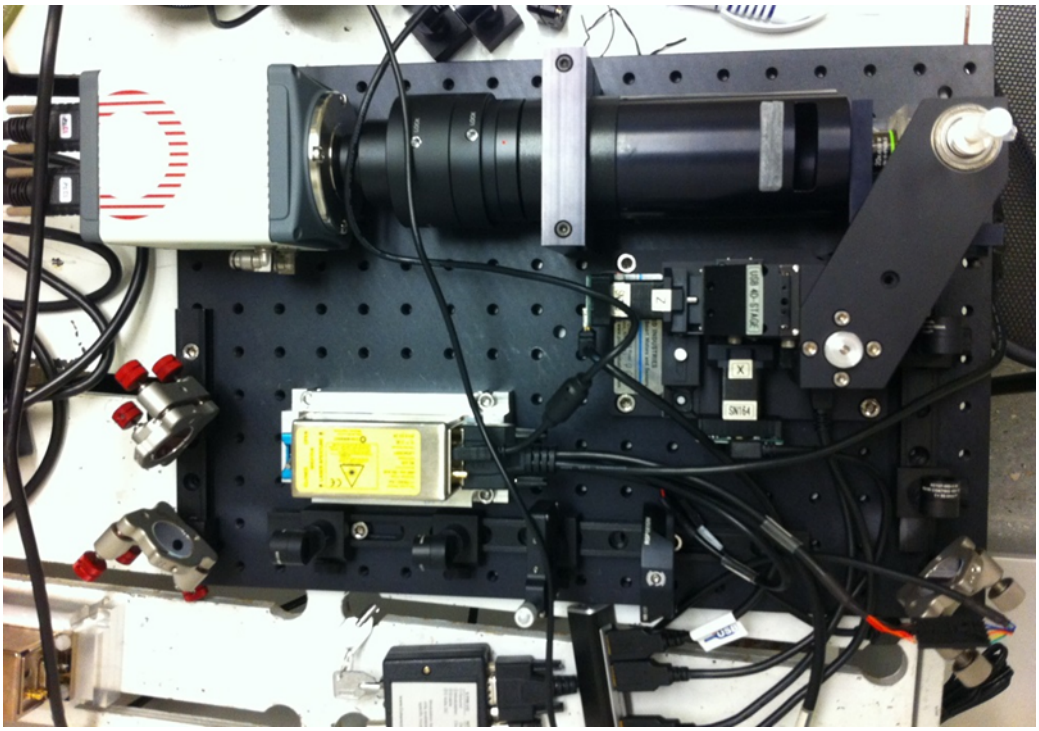

Figure A.3: OpenSPIM- custom built setup

A.1.2 Camera

The camera used in this system is a CMOS camera, which has a lower readout noise than the conventional charged coupled device (CCD) cameras. High-speed readout (100 frame/second with 2048 x 2048 pixels) with low readout noise can be achieved.

The pixel of a CMOS image sensor is composed of the photodiode and the amplifier that converts the charge into voltage (Fig. A.4). Entered light is converted to charge and converted to voltage in the pixel. The voltage of each pixel is output by switching the switch one by one. Instead of one amplifier at the side of the array, each individual pixel has its own personal amplifier. This individual amplifier linked to each photo diode is typical of the architecture of a CMOS sensor and can increase the noise. To minimise this effect, the FL-400 sensor used in this camera has an on-chip correlated double sampling circuit. Low noise and high speed readout are also achieved with the structure of the sensor, where the top and bottom halves are readout independently, and the data of each horizontal line is read by two lines of column amplifier and A/D (clocking frequency) in the top and the bottom in parallel

and simultaneously. The FL-400 sensor has 6.5 µm x 6.5 µm pixel sizes and is cooled down by the peltier element to suppress the dark current.

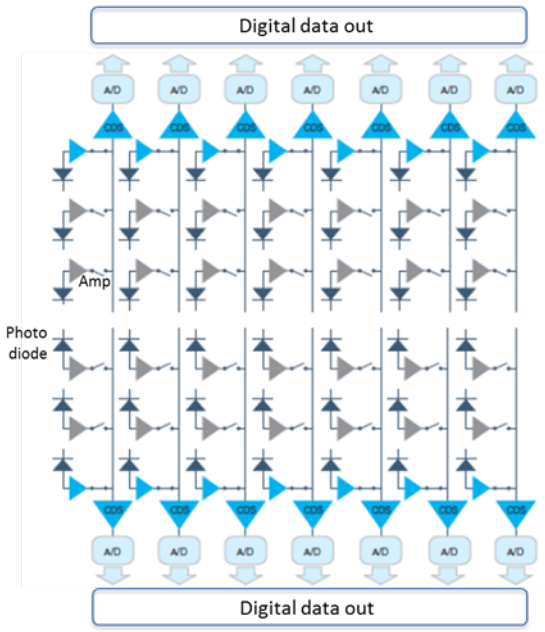

Figure A.4: Structure of the FL-400 sensor. In a CMOS sensor, each pixel has its own charge-to-voltage conversion: an individual amplifier (light grey) is linked to each single photo diode (dark grey). This architecture can result in high noise, that in this camera is lowered with an on-chip CDS circuit.

As mentioned, CMOS image sensors convert the incident light into a charge in each pixel and detect it as a signal. An important factor in determining the sensitivity of a camera is the quantum efficiency (QE), which is the efficiency in converting light into electric charge. Since CMOS image sensors have multiple amplifiers arrayed in one pixel, the sensor unit that performs the light-to-charge conversion is limited to a part of the pixel. Therefore, by providing an on-chip microlens for each pixel, the utilization efficiency of light is increased and the sensor has improved sensitivity (Figure A.5).

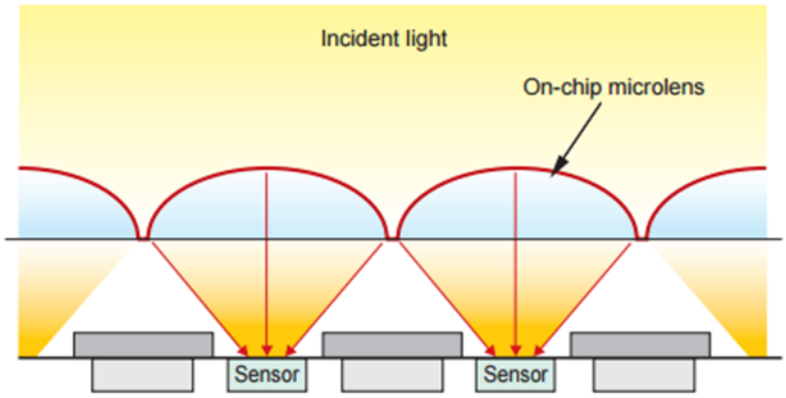

Figure A.5: Structural diagram of the on-chip microlens

Furthermore, by optimizing the element structure, the light utilization efficiency or the OrcaFlash 4.0 is increased, achieving increased sensitivity in comparison with conventional CMOS image sensors (Figure A.6).

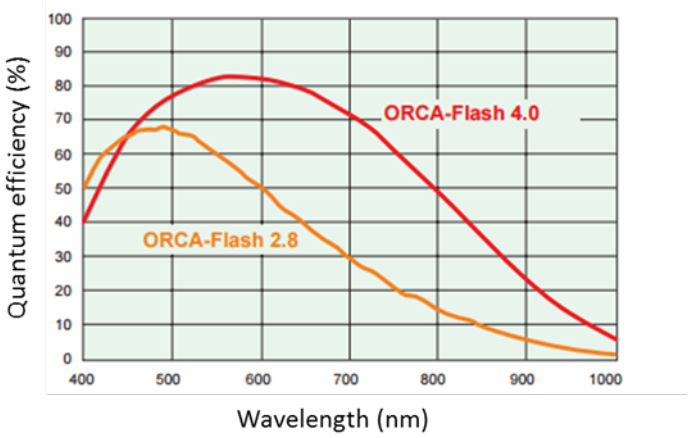

Figure A.6: Spectral sensitivity table. The sensor of the camera used for the SPIM built in this project is compared with conventional CMOS image sensors (e.g. the sensor of a precedent ORCA model). The improved element structure of the ORCA Flash 4.0 allows higher QE (peak 82%).

The exposure and the readout method of the sensor is rolling shutter. In this configuration, the exposure and readout are done line by line (Figure A.7). Therefore, the exposure timing is different on one screen. The main advantage of rolling shutters over global shutters, where light hits the entire sensor array at one time, is the shorter time they take to deliver the image. Generally speaking, CCD sensors utilize a global shutter and CMOS sensors utilize rolling shutter. For a

CMOS sensor in rolling shutter mode, the frame rate is determined by the speed of the A/D and the number of rows in the sensor.

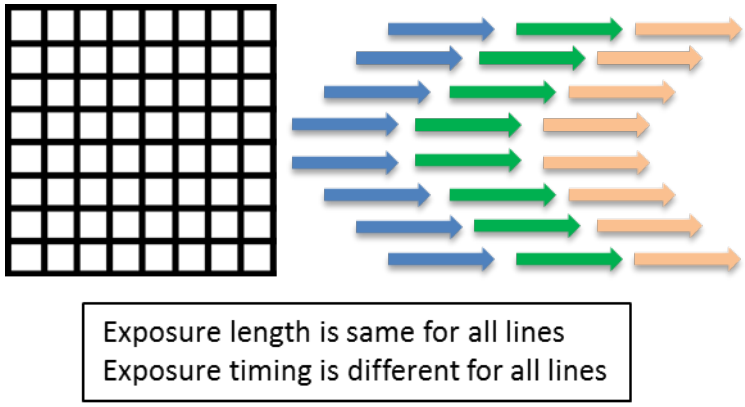

Figure A.7: Readout timing of rolling shutter. Each row in a frame expose for the same amount of time but begins exposing at a different point in time, allowing overlapping exposures for two frames.

With the Orca Flash 4.0 camera, 2x2 and 4x4 binning readout are available by adding the signal of adjacent pixels in the digital domain. The advantage of using binning is the reduction of signal noise and thereby an increase of the signal-to-noise ratio (SNR) which describes the information content. Whenever a detector is exposed to light, there is always a certain amount of noise associated with the image. Read noise is generated due to the process of downloading the image from a chip, which, due to imperfection of information transfer, creates an uncertain noise, which is intrinsically random and unavoidable. Another major noise source is the dark noise, which is reduced by cooling the temperature of the CCD chip respectively to the ambient temperature. The benefit of binning is the amplification of the signal-to-noise ratio. Considering that each pixel is noise afflicted, the adding of 4 pixels (as shown in figure A.8) will result in an increased SNR by a factor $(4 \cdot \text{signal}/\sqrt{(4 \cdot \text{noise})}$ since larger pixel areas constitute larger SNR's. Noise adds as the square root since it's a random process. This results in a higher sensitivity of the camera.

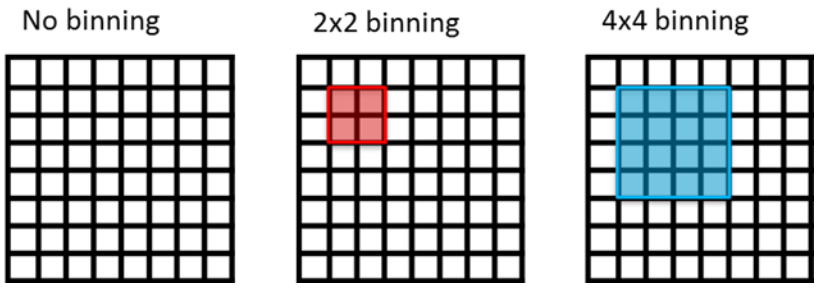

Figure A.8: Schematic of a binning procedure. No binning (left), 2 by 2 binning (centre), 4 by 4 binning (right).

Although binning increases the SNR, its drawback is the loss of resolution. Larger pixels detect more portions of an object. Thus, this always requires an agreement between resolution and signal detection.

The Hamamatsu Flash 4.0 camera has both Camera Link and USB 3.0 interface. We use the Camera Link interface. This can transfer 4 megapixels image with 100 frame/s.

To achieve full 100 fps speed recording, further recommended PC configurations for optimal camera functioning are a RAM of 24 GB or more, at least one free x8 Gen2 slot for the frame grabber, Active Silicon AS-FBD-1XCLD-2PE8 Frame Grabber. In case of storing on SSD card instead of on RAM, two free x8 Gen2 slots are required (for the frame grabber and the RAID card).

A.1.3 Laser

The 488 nm laser used in this microscope is a diode laser system that has an output power of 50 mW, beam diameter of 1 mm at $1/e^2$, beam divergence of 1 mrad. The 730 nm laser has an output power of 30 mW, beam diameter of 1.2 mm at $1/e^2$, beam divergence of 0.9 mrad.

A.1.4 Stage

The USB 4D-Stage is a motorized precision motion control system powered and controlled with USB ports. All linear position movements are relative to the home

(fully retracted) position. A built-in magnetic sensor (based on the Hall effect) is used to establish this home position. The 4D-Stage is characterized by linear (X, Y, Z) range of about 9 mm, positional resolution of 1.5 microns, and rotational resolution of 200 steps/revolution (1.8 degrees).

A.1.5 Hardware configuration

The Fiji version used to control the microscope was the Fiji package updated with the OpenSpim, version 1.0. When Micro-Manager is first started, it requires a hardware configuration to run the microscope. A new configuration was created for the SPIM. The laser was added by selecting the appropriate port and setting the Baud Rate property to 192000. The camera was configured by adding the HamamatsuHam_DCAM device. Finally, the twister, the Z stage and the XY stages were added to configure the motor. At this stage, the configuration is saved and loaded, and the SPIM is ready to acquire an image.

A.1.6 Alignment procedure

For successful SPIM image acquisition the aforementioned hardware components were optically aligned. Indeed, the light sheet needs to be shaped by the optics of the system to be parallel to the imaging plane of the camera, perpendicular to the detection axis, as thin as possible, uniform across the field of view and in focus with the detection objective. Although the light sheet is rather stable once aligned, it should be aligned at regular intervals.

A phantom was used for the alignment process: a scratch was made on a small silver mirror (5 mm diameter, 1 mm thick), which was attached to the 1ml syringe and immersed in water within the chamber. First we focussed on the scratch on the mirror, by illuminating it with a white LED or simple lamp through the projection objective. Then we switched to the laser and first brought it to the sharp line on the mirror and finally align it with the lenses of the illumination beam path.

Fluorescent microbeads (Invitrogen, T-7279, 0.1 μm) were also used for microscope calibration. For phantom preparation, 0.5% agarose gel was made with deionized

water (section 3.2.4.2). The top part of a 1 ml syringe is cut off. $MgSO_4$ was added to the agarose solution to an end concentration of 0.1%. While still >40°C, the beads are added to 1 ml of the solution (different concentrations: 5-10 µl). The solution is mixed, 300 µl are then pulled up into a syringe and refrigerated at 4 °C until the gel solidifies and is ready to be inserted in the SPIM.

Since during calibration the laser is reflected right onto the camera, an absorptive Neutral Density (ND) filter was used to turn down the laser intensity far enough to avoid camera damages. ND filters have a neutral grey colour and are calibrated in unities of absorbance or optical density (OD):

$$OD = \log_{10} \frac{1}{T} \qquad \text{Eq. A.1}$$

where T is the transmittance (intensity of light transmitted/intensity of incident light). Therefore the ND depends on the lowest power that can be set on the laser to and on the sensitivity of the camera. For calibration of the microscope built in this study, a ND filter with OD= 6.0 was introduced in the detection path (NE560B, Thorlabs), thus 0.001% of light was transmitted. Also, a notch filter was inserted in the excitation path to clean up the 488 line of the Cube laser, since a small amount of light >500 nm could get through the emission filters and cause a reflection.

A.1.7 Sample preparation

The sample needs to be suspended in a water filled chamber in front of the lens so that it can be rotated. This was achieved by embedding the sample in a low melting point agarose inside a 1 ml syringe. The procedure for sample embedding is described in section 3.2.4.2.

A.1.8 Images acquisition

The µManager plugin of Fiji is used to acquire images. Camera, motor and laser are powered on before the µManager program was initiated. Once initialized, the motors are homed and reset to their default position. The white light source is powered on to properly position the sample within the FOV of the camera within the chamber.

CMOS camera setting such as exposure time, electronic gain, image size and binning are adjusted in the live view. The sample is placed in the SPIM system and is suspended from the arm of the rotator stage through a 1 ml syringe. The sample is then lowered into the water filled chamber until it is fully immersed and within the FOV of the camera. The sample is centred with manual fine adjustment with a set of forceps. To ensure that the sample is centred on the axis of rotation, it is rotated another 90 degrees. This is done iteratively until the sample rotates on the motor centre of rotation and in-focus.

The white light source is powered off and the laser is powered on. The appropriate emission filter is placed in the detection axis. At the initialization of the scan, an image is acquired per each angle of rotation for a whole rotation of 360 °. To acquire a single image, the 4-D stage is navigated to the location of interest. The stack depth is set to 0 to limit the position to a single plane and the image is taken.

An example of a preliminary image is shown in figure A.9. This represents a 24 hours old zebrafish embryo (courtesy of Dr. Paula Alexandre, UCL Institute of Child Health). The zebrafish was injected with rab8 conjugated with GFP then fixed in formalin. Rab8 is a 24 kDa vesicular marker that belongs to the Rab GTPase family. Prior to imaging, the sample was rinsed with saline and embedded in agarose.

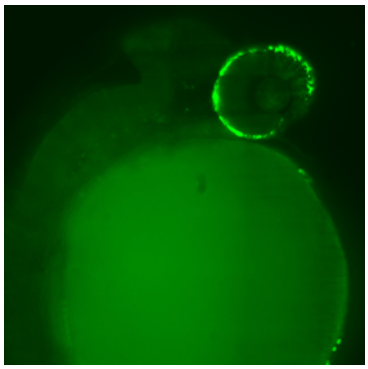

Figure A.9: SPIM image of a 24 hours old zebrafish embryo. The fish was stained with Rab8 conjugated with GFP, which stained the fish's retina (upper bright circle). The lower circle represents the yolk sack.

A.2 Discussions and future work

Light sheet microscopy allows fast, high resolution 3-D imaging of whole organisms with low photodamage (94). The setup built in this project is a basic one-side illumination configuration assembled mainly following the directions from the OpenSpim platform. The main application is the study of fixed or live uncleared small specimens, such as fruit fly and zebrafish. Indeed, these samples are already intrinsically transparent and do not require optical clearing prior to imaging. This setup will be modified to allow imaging of big samples, such as mouse organs and tumours, after optical clearing. Although hardware components such as camera and laser will be the same as the setup already assembled, the optics will change according to the sample size, e.g. to allow a bigger FOV.

References

1. Massoud TF, Gambhir SS. Molecular imaging in living subjects: seeing fundamental biological processes in a new light. Genes & development. 2003;17(5):545-80.

2. Kak A SM. Principles of computerized tomographic imaging, IEEE Press, 1988.

3. Gilbert ES. Ionizing Radiation and Cancer Risks: What Have We Learned From Epidemiology? International journal of radiation biology. 2009;85(6):467-82.

4. Prasad KN, Cole WC, Hasse GM. Health risks of low dose ionizing radiation in humans: a review. Experimental biology and medicine (Maywood, NJ). 2004;229(5):378-82.

5. Jensen JA. Medical ultrasound imaging. Progress in biophysics and molecular biology. 2007;93(1-3):153-65.

6. Hornak JP. The Basics of MRI.

7. Minsky M. Memoir on inventing the confocal scanning microscope. Scanning. 1988;10(4):128-38.

8. Lakowicz JR. Principles of Fluorescence Spectroscopy. Third Edition ed. Springer, 2006.

9. http://www.thermofisher.com.

10. Chalfie M, Tu Y, Euskirchen G, Ward WW, Prasher DC. Green fluorescent protein as a marker for gene expression. Science (New York, NY). 1994;263(5148):802-5.

11. Ballou B, Lagerholm BC, Ernst LA, Bruchez MP, Waggoner AS. Noninvasive imaging of quantum dots in mice. Bioconjugate chemistry. 2004;15(1):79-86.

12. Chen N, He Y, Su Y, Li X, Huang Q, Wang H, et al. The cytotoxicity of cadmium-based quantum dots. Biomaterials. 2012;33(5):1238-44.

13. Mahendra S, Zhu H, Colvin VL, Alvarez PJ. Quantum dot weathering results in microbial toxicity. Environmental science & technology. 2008;42(24):9424-30.

14. Oh E, Liu R, Nel A, Gemill KB, Bilal M, Cohen Y, et al. Meta-analysis of cellular toxicity for cadmium-containing quantum dots. Nature Nanotechnology. 2016;11(5):479-86.

15. Benson RC, Meyer RA, Zaruba ME, McKhann GM. Cellular autofluorescence--is it due to flavins? The journal of histochemistry and cytochemistry : official journal of the Histochemistry Society. 1979;27(1):44-8.

16. Chorvat D, Kirchnerova J, Cagalinec M, Smolka J, Mateasik A, Chorvatova A. Spectral Unmixing of Flavin Autofluorescence Components in Cardiac Myocytes. Biophysical Journal. 2005;89(6):L55-L7.

17. Heureux BL, Gurden H, Pain F. Autofluorescence imaging of NADH and flavoproteins in the rat brain: insights from Monte Carlo simulations. Optics express. 2009;17(12):9477-90.

18. Schnell SA, Staines WA, Wessendorf MW. Reduction of lipofuscin-like autofluorescence in fluorescently labeled tissue. The journal of histochemistry and cytochemistry : official journal of the Histochemistry Society. 1999;47(6):719-30.

19. Billinton N, Knight AW. Seeing the wood through the trees: a review of techniques for distinguishing green fluorescent protein from endogenous autofluorescence. Analytical biochemistry. 2001;291(2):175-97.

20. Monici M. Cell and tissue autofluorescence research and diagnostic applications. Biotechnology Annual Review. Volume 11: Elsevier; 2005. p. 227-56.

21. Weber P, Wagner M, Kioschis P, Kessler W, Schneckenburger H. Tumor cell differentiation by label-free fluorescence microscopy. Journal of biomedical optics. 2012;17(10):101508.

22. Haringsma J, Tytgat GNJ. Fluorescence and autofluorescence. Best Practice & Research Clinical Gastroenterology. 1999;13(1):1-10.

23. Clancy B, Cauller LJ. Reduction of background autofluorescence in brain sections following immersion in sodium borohydride. Journal of neuroscience methods. 1998;83(2):97-102.

24. Tagliaferro P, Tandler CJ, Ramos AJ, Pecci Saavedra J, Brusco A. Immunofluorescence and glutaraldehyde fixation. A new procedure based on the Schiff-quenching method. Journal of neuroscience methods. 1997;77(2):191-7.

25. Shimomura O, Johnson FH, Saiga Y. Extraction, purification and properties of aequorin, a bioluminescent protein from the luminous hydromedusan, Aequorea. Journal of cellular and comparative physiology. 1962;59:223-39.

26. Prasher DC, Eckenrode VK, Ward WW, Prendergast FG, Cormier MJ. Primary structure of the Aequorea victoria green-fluorescent protein. Gene. 1992;111(2):229-33.

27. Sekar RB, Periasamy A. Fluorescence resonance energy transfer (FRET) microscopy imaging of live cell protein localizations. The Journal of Cell Biology. 2003;160(5):629-33.

28. Hanson MR, Kohler RH. GFP imaging: methodology and application to investigate cellular compartmentation in plants. Journal of experimental botany. 2001;52(356):529-39.

29. Wallrabe H, Periasamy A. Imaging protein molecules using FRET and FLIM microscopy. Current opinion in biotechnology. 2005;16(1):19-27.

30. White JJ. An evaluation of confocal versus conventional imaging of biological structures by fluorescence light microscopy. The Journal of Cell Biology. 1987;105(1):41-8.

31. Göppert-Mayer M. Über Elementarakte mit zwei Quantensprüngen. Annalen der Physik. 1931;401(3):273-94.

32. Helmchen F, Denk W. Deep tissue two-photon microscopy. Nature methods. 2005;2(12):932-40.

33. Stephens DJ, Allan VJ. Light microscopy techniques for live cell imaging. Science (New York, NY). 2003;300(5616):82-6.

34. Huang B, Bates M, Zhuang X. Super resolution fluorescence microscopy. Annual review of biochemistry. 2009;78:993-1016.

35. Hell SW, Wichmann J. Breaking the diffraction resolution limit by stimulated emission: stimulated-emission-depletion fluorescence microscopy. Optics Letters. 1994;19(11):780-2.

36. Klar TA, Hell SW. Subdiffraction resolution in far-field fluorescence microscopy. Optics Letters. 1999;24(14):954-6.

37. Betzig E, Patterson GH, Sougrat R, Lindwasser OW, Olenych S, Bonifacino JS, et al. Imaging intracellular fluorescent proteins at nanometer resolution. Science (New York, NY). 2006;313(5793):1642-5.

38. Beard P. Biomedical photoacoustic imaging. Interface focus. 2011;1(4):602-31.

39. Duck FA. Physical Properties of Tissue: A comprehensice reference book. London: Academic; 1990.

40. Laufer J, Johnson P, Zhang E, Treeby B, Cox B, Pedley B, et al. In vivo preclinical photoacoustic imaging of tumor vasculature development and therapy. Journal of biomedical optics. 2012;17(5):056016.

41. Rudenberg HG, Rudenberg PG. Chapter 6 - Origin and Background of the Invention of the Electron Microscope: Commentary and Expanded Notes on Memoir of Reinhold Rüdenberg*. Advances in Imaging and Electron Physics. Volume 160: Elsevier; 2010. p. 207-86.

42. Potter SM. Vital imaging: Two photons are better than one. Current Biology. 1996;6(12):1595-8.

43. Boas DA, O'Leary MA, Chance B, Yodh AG. Scattering of diffuse photon density waves by spherical inhomogeneities within turbid media: analytic solution and applications. Proceedings of the National Academy of Sciences of the United States of America. 1994;91(11):4887-91.

44. Contag CH, Contag PR, Mullins JI, Spilman SD, Stevenson DK, Benaron DA. Photonic detection of bacterial pathogens in living hosts. Molecular Microbiology. 1995;18(4):593-603.

45. Conchello J-A, Lichtman JW. Optical sectioning microscopy. Nature Methods. 2005;2(12):920-31.

46. Horecker BL. The absorption spectra of hemoglobin and its derivatives in the visible and near infra-red regions. Journal of Biological Chemistry. 1943;148:173-83.

47. Alnuami AA, Zeedi B, Qadri SM, Ashraf SS. Oxyradical-induced GFP damage and loss of fluorescence. International journal of biological macromolecules. 2008;43(2):182-6.

48. Ntziachristos V. Going deeper than microscopy: the optical imaging frontier in biology. Nature Methods. 2010;7(8):603-14.

49. Schotland JC. Continuous-wave diffusion imaging. Journal of the Optical Society of America A. 1997;14(1):275-9.

50. Cheong WF, Prahl, S. A., Welch, A. J. A review of the Optical Properties of Biological Tissues. IEEE Journal of Quantum Electronics. 1990;26:2166-85.

51. van der Zee P, Cope M, Arridge SR, Essenpreis M, Potter LA, Edwards AD, et al. Experimentally measured optical pathlengths for the adult head, calf and forearm and the head of the newborn infant as a function of inter optode spacing. Advances in experimental medicine and biology. 1992;316:143-53.

52. Simpson CR, Kohl M, Essenpreis M, Cope M. Near-infrared optical properties of ex vivo human skin and subcutaneous tissues measured using the Monte Carlo inversion technique. Physics in medicine and biology. 1998;43(9):2465-78.

53. Genina EA, Bashkatov AN, Tuchin VV. Tissue optical immersion clearing. Expert review of medical devices. 2010;7(6):825-42.

54. Richardson Douglas S, Lichtman Jeff W. Clarifying Tissue Clearing. Cell.162(2):246-57.

55. Spalteholz. Über das Durchsichtigmachen von menschlichen und tierischen Präparaten und seine theoretischen Bedingungen, nebst Anhang: Über Knochenfärbung 1914.

56. Rylander CG, Stumpp OF, Milner TE, Kemp NJ, Mendenhall JM, Diller KR, et al. Dehydration mechanism of optical clearing in tissue. Journal of biomedical optics. 2006;11(4):041117.

57. Erturk A, Mauch CP, Hellal F, Forstner F, Keck T, Becker K, et al. Three-dimensional imaging of the unsectioned adult spinal cord to assess axon regeneration and glial responses after injury. Nature Medicine. 2012;18(1):166-71.

58. Bucher D, Scholz M, Stetter M, Obermayer K, Pfluger HJ. Correction methods for three-dimensional reconstructions from confocal images: I. Tissue shrinking and axial scaling. Journal of neuroscience methods. 2000;100(1-2):135-43.

59. Becker K, Jahrling N, Saghafi S, Weiler R, Dodt HU. Chemical clearing and dehydration of GFP expressing mouse brains. PloS one. 2012;7(3):e33916.

60. Jiang J, Boese M, Turner P, Wang RK. Penetration kinetics of dimethyl sulphoxide and glycerol in dynamic optical clearing of porcine skin tissue in vitro studied by Fourier transform infrared spectroscopic imaging. Journal of biomedical optics. 2008;13(2):021105.

61. Zhi Z, Han Z, Luo Q, Zhu DAN. Improve optical clearing of skin in vitro with propylene glycol as a penetration enhancer Journal of Innovative Optical Health Sciences. 2009;02(03):269-78.

62. Ursin C, Hansen CM, Van Dyk JW, Jensen PO, Christensen IJ, Ebbehoej J. Permeability of commercial solvents through living human skin. American Industrial Hygiene Association journal. 1995;56(7):651-60.

63. Kuwajima T, Sitko AA, Bhansali P, Jurgens C, Guido W, Mason C. ClearT: a detergent- and solvent-free clearing method for neuronal and non-neuronal tissue. Development (Cambridge, England). 2013;140(6):1364-8.

64. Yeh AT, Hirshburg J. Molecular interactions of exogenous chemical agents with collagen--implications for tissue optical clearing. Journal of biomedical optics. 2006;11(1):014003.

65. Ke M-T, Fujimoto S, Imai T. SeeDB: a simple and morphology-preserving optical clearing agent for neuronal circuit reconstruction. Nature Neuroscience. 2013;16(8):1154-61.

66. Hama H, Kurokawa H, Kawano H, Ando R, Shimogori T, Noda H, et al. Scale: a chemical approach for fluorescence imaging and reconstruction of transparent mouse brain. Nature Neuroscience. 2011;14(11):1481-8.

67. Kim S-Y, Chung K, Deisseroth K. Light microscopy mapping of connections in the intact brain. Trends in Cognitive Sciences.17(12):596-9.

68. Chung K, Wallace J, Kim S-Y, Kalyanasundaram S, Andalman AS, Davidson TJ, et al. Structural and molecular interrogation of intact biological systems. Nature. 2013;497(7449):332-7.

69. Chung K, Deisseroth K. CLARITY for mapping the nervous system. Nature methods. 2013;10(6):508-13.

70. Tomer R, Ye L, Hsueh B, Deisseroth K. Advanced CLARITY for rapid and high-resolution imaging of intact tissues. Nature Protocols. 2014;9(7):1682-97.

71. Yang B, Treweek Jennifer B, Kulkarni Rajan P, Deverman Benjamin E, Chen C-K, Lubeck E, et al. Single-Cell Phenotyping within Transparent Intact Tissue through Whole-Body Clearing. Cell. 2014;158(4):945-58.

72. Susaki EA, Tainaka K, Perrin D, Kishino F, Tawara T, Watanabe TM, et al. Whole-brain imaging with single-cell resolution using chemical cocktails and computational analysis. Cell. 2014;157(3):726-39.

73. Chen B-C, Legant WR, Wang K, Shao L, Milkie DE, Davidson MW, et al. Lattice Light Sheet Microscopy: Imaging Molecules to Embryos at High Spatiotemporal Resolution. Science (New York, NY). 2014;346(6208):1257998-.

74. Peachey LD. Thin sections. I. A study of section thickness and physical distortion produced during microtomy. The Journal of biophysical and biochemical cytology. 1958;4(3):233-42.

75. Sharpe J. Optical projection tomography as a new tool for studying embryo anatomy. Journal of anatomy. 2003;202(2):175-81.

76. Sharpe J. Optical projection tomography. Annual review of biomedical engineering. 2004;6:209-28.

77. Sharpe J, Ahlgren U, Perry P, Hill B, Ross A, Hecksher-Sorensen J, et al. Optical projection tomography as a tool for 3D microscopy and gene expression studies. Science (New York, NY). 2002;296(5567):541-5.

78. Walls JR, Coultas L, Rossant J, Henkelman RM. Three-dimensional analysis of vascular development in the mouse embryo. PloS one. 2008;3(8):e2853.

79. Lickert H, Takeuchi JK, Von Both I, Walls JR, McAuliffe F, Adamson SL, et al. Baf60c is essential for function of BAF chromatin remodelling complexes in heart development. Nature. 2004;432(7013):107-12.

80. Jeansson M, Gawlik A, Anderson G, Li C, Kerjaschki D, Henkelman M, et al. Angiopoietin-1 is essential in mouse vasculature during development and in response to injury. The Journal of clinical investigation. 2011;121(6):2278-89.

81. Takeuchi JK, Lou X, Alexander JM, Sugizaki H, Delgado-Olguin P, Holloway AK, et al. Chromatin remodelling complex dosage modulates transcription factor function in heart development. Nature Communications. 2011;2:187.

82. Short K SL. Kidney Development2012.

83. Alanentalo T, Asayesh A, Morrison H, Loren CE, Holmberg D, Sharpe J, et al. Tomographic molecular imaging and 3D quantification within adult mouse organs. Nature Methods. 2007;4(1):31-3.

84. Kumar V, Chyou S, Stein JV, Lu TT. Optical projection tomography reveals dynamics of HEV growth after immunization with protein plus CFA and features shared with HEVs in acute autoinflammatory lymphadenopathy. Frontiers in immunology. 2012;3:282.

85. Colas JF, Sharpe J. Live optical projection tomography. Organogenesis. 2009;5(4):211-6.

86. Rieckher M, Birk UJ, Meyer H, Ripoll J, Tavernarakis N. Microscopic optical projection tomography in vivo. PloS one. 2011;6(4):e18963.

87. Zhu S, Dong D, Birk UJ, Rieckher M, Tavernarakis N, Qu X, et al. Automated motion correction for in vivo optical projection tomography. IEEE transactions on medical imaging. 2012;31(7):1358-71.

88. Fieramonti L, Bassi A, Foglia EA, Pistocchi A, D'Andrea C, Valentini G, et al. Time-gated optical projection tomography allows visualization of adult zebrafish internal structures. PloS one. 2012;7(11):e50744.

89. Miller SF, Summerhurst K, Runker AE, Kerjan G, Friedel RH, Chedotal A, et al. Expression of Plxdc2/TEM7R in the developing nervous system of the mouse. Gene expression patterns : GEP. 2007;7(5):635-44.

90. Huisken J, Swoger J, Del Bene F, Wittbrodt J, Stelzer EHK. Optical Sectioning Deep Inside Live Embryos by Selective Plane Illumination Microscopy. Science (New York, NY). 2004;305(5686):1007-9.

91. Siedentopf H, Zsigmondy R. Uber Sichtbarmachung und Größenbestimmung ultramikoskopischer Teilchen, mit besonderer Anwendung auf Goldrubingläser. Annalen der Physik. 1902;315(1):1-39.

92. Verveer PJ, Swoger J, Pampaloni F, Greger K, Marcello M, Stelzer EH. High-resolution three-dimensional imaging of large specimens with light sheet-based microscopy. Nature methods. 2007;4(4):311-3.

93. Engelbrecht CJ, Stelzer EH. Resolution enhancement in a light-sheet-based microscope (SPIM). Optics Letters. 2006;31(10):1477-9.

94. Huisken J, Stainier DYR. Selective plane illumination microscopy techniques in developmental. Development (Cambridge, England). 2009;136(12):1963-75.

95. Weninger WJ, Geyer SH, Mohun TJ, Rasskin-Gutman D, Matsui T, Ribeiro I, et al. High-resolution episcopic microscopy: a rapid technique for high detailed 3D

analysis of gene activity in the context of tissue architecture and morphology. Anatomy and Embryology (Berl). 2006;211(3):213-21.

96. Weissleder R. Scaling down imaging: molecular mapping of cancer in mice. Nature reviews Cancer. 2002;2(1):11-8.

97. Pautler RG, Fraser SE. The year(s) of the contrast agent - micro-MRI in the new millennium. Current opinion in immunology. 2003;15(4):385-92.

98. Meng Y, Shaw CC, Liu X, Altunbas MC, Wang T, Chen L, et al. Comparison of two detector systems for cone beam CT small animal imaging - a preliminary study. Proceedings of SPIE--the International Society for Optical Engineering. 2006;6142:614245-.

99. Ciobanu L, Pennington CH. 3D micron-scale MRI of single biological cells. Solid state nuclear magnetic resonance. 2004;25(1-3):138-41.

100. Murphy GE, Jensen GJ. Electron cryotomography. BioTechniques. 2007;43(4):413, 5, 7 passim.

101. Muscariello L, Rosso F, Marino G, Giordano A, Barbarisi M, Cafiero G, et al. A critical overview of ESEM applications in the biological field. Journal of cellular physiology. 2005;205(3):328-34.

102. Koster AJ, Klumperman J. Electron microscopy in cell biology: integrating structure and function. Nature reviews Molecular cell biology. 2003;Suppl:Ss6-10.

103. Stan RV. Structure of caveolae. Biochimica et biophysica acta. 2005;1746(3):334-48.

104. Stelzer EHK, Lindek S. Fundamental reduction of the observation volume in far-field light microscopy by detection orthogonal to the illumination axis: confocal theta microscopy. Optics Communications. 1994;111(5):536-47.

105. Santi PA. Light sheet fluorescence microscopy: a review. The journal of histochemistry and cytochemistry : official journal of the Histochemistry Society. 2011;59(2):129-38.

106. Willmann JK, van Bruggen N, Dinkelborg LM, Gambhir SS. Molecular imaging in drug development. Nature Reviews Drug Discovery. 2008;7(7):591-607.

107. Weissleder R. Molecular imaging in cancer. Science (New York, NY). 2006;312(5777):1168-71.

108. Cuenod C, Leconte I, Siauve N, Resten A, Dromain C, Poulet B, et al. Early changes in liver perfusion caused by occult metastases in rats: detection with quantitative CT. Radiology. 2001;218(2):556-61.

109. Thng CH, Koh TS, Collins DJ, Koh DM. Perfusion magnetic resonance imaging of the liver. World Journal of Gastroenterology : WJG. 2010;16(13):1598-609.

110. Tyszka JM, Fraser SE, Jacobs RE. Magnetic resonance microscopy: recent advances and applications. Current opinion in biotechnology. 2005;16(1):93-9.

111. Kalender WA. CT: the unexpected evolution of an imaging modality. European radiology. 2005;15 Suppl 4:D21-4.

112. Brown EB, Campbell RB, Tsuzuki Y, Xu L, Carmeliet P, Fukumura D, et al. In vivo measurement of gene expression, angiogenesis and physiological function in tumors using multiphoton laser scanning microscopy. Nature Medicine. 2001;7(7):864-8.

113. Fukumura D, Duda DG, Munn LL, Jain RK. Tumor microvasculature and microenvironment: novel insights through intravital imaging in pre-clinical models. Microcirculation (New York, NY : 1994). 2010;17(3):206-25.

114. Guo X, Guo Z, Wei H, Yang H, He Y, Xie S, et al. In vivo comparison of the optical clearing efficacy of optical clearing agents in human skin by quantifying permeability using optical coherence tomography. Photochemistry and photobiology. 2011;87(3):734-40.

115. Zhu D, Larin KV, Luo Q, Tuchin VV. Recent progress in tissue optical clearing. Laser & Photonics Reviews. 2013;7(5):732-57.

116. Choi B, Tsu L, Chen E, Ishak TS, Iskandar SM, Chess S, et al. Determination of chemical agent optical clearing potential using in vitro human skin. Lasers in surgery and medicine. 2005;36(2):72-5.

117. Dodt HU, Leischner U, Schierloh A, Jahrling N, Mauch CP, Deininger K, et al. Ultramicroscopy: three-dimensional visualization of neuronal networks in the whole mouse brain. Nature methods. 2007;4(4):331-6.

118. Workman P, Aboagye EO, Balkwill F, Balmain A, Bruder G, Chaplin DJ, et al. Guidelines for the welfare and use of animals in cancer research. British Journal of Cancer. 2010;102(11):1555-77.

119. Chia R, Achilli F, Festing MF, Fisher EM. The origins and uses of mouse outbred stocks. Nature genetics. 2005;37(11):1181-6.

120. Janssen FJ. A study of the absorption and scattering factors of light in whole blood. Medical & biological engineering. 1972;10(2):231-40.

121. Dent JA, Polson AG, Klymkowsky MW. A whole-mount immunocytochemical analysis of the expression of the intermediate filament protein vimentin in Xenopus. Development (Cambridge, England). 1989;105(1):61-74.

122. White JJ, Reeber SL, Hawkes R, Sillitoe RV. Wholemount immunohistochemistry for revealing complex brain topography. Journal of visualized experiments : JoVE. 2012(62):e4042.

123. Querry MR, Cary PG, Waring RC. Split-pulse laser method for measuring attenuation coefficients of transparent liquids: application to deionized filtered water in the visible region. Applied optics. 1978;17(22):3587-92.

124. Biwas T, Gupta A. Retrieval of true color of the internal organ of CT images and attempt to tissue characterization by refractive index : Initial experience. Indian Journal of Radiology and Imaging. 2002;12(2):169-78.

125. Yaroslavsky AN, Schulze PC, Yaroslavsky IV, Schober R, Ulrich F, Schwarzmaier HJ. Optical properties of selected native and coagulated human brain tissues in vitro in the visible and near infrared spectral range. Physics in medicine and biology. 2002;47(12):2059-73.

126. Roggan A, Minet O, Schroeder C, Mueller GJ. Determination of optical tissue properties with double integrating sphere technique and Monte Carlo simulations. 1994; Proc.SPIE2100.

127. Purves A, Fitzpatrick, Katz, McNamara, Williams. Neuroscience. 4th Ed. 2007. 15-6 p.

128. Bui AK, McClure RA, Chang J, Stoianovici C, Hirshburg J, Yeh AT, et al. Revisiting optical clearing with dimethyl sulfoxide (DMSO). Lasers in surgery and medicine. 2009;41(2):142-8.

129. Tuchin VV, Maksimova IL, Zimnyakov DA, Kon IL, Mavlyutov AH, Mishin AA. Light propagation in tissues with controlled optical properties. Journal of biomedical optics. 1997;2(4):401-17.

130. Konerding MA, Malkusch W, Klapthor B, van Ackern C, Fait E, Hill SA, et al. Evidence for characteristic vascular patterns in solid tumours: quantitative studies using corrosion casts. British Journal of Cancer. 1999;80(5-6):724-32.

131. Jain RK. Determinants of tumor blood flow: a review. Cancer research. 1988;48(10):2641-58.

132. Fukumura D, Jain RK. Tumor microvasculature and microenvironment: targets for anti-angiogenesis and normalization. Microvascular research. 2007;74(2-3):72-84.

133. van den Wijngaard JP, Schwarz JC, van Horssen P, van Lier MG, Dobbe JG, Spaan JA, et al. 3D Imaging of vascular networks for biophysical modeling of perfusion distribution within the heart. Journal of biomechanics. 2013;46(2):229-39.

134. Bassingthwaighte JB, Chizeck HJ. The Physiome Projects and Multiscale Modeling. IEEE signal processing magazine. 2008;25(2):121-44.

135. Krams R, Wentzel JJ, Oomen JA, Vinke R, Schuurbiers JC, de Feyter PJ, et al. Evaluation of endothelial shear stress and 3D geometry as factors determining the development of atherosclerosis and remodeling in human coronary arteries in vivo. Combining 3D reconstruction from angiography and IVUS (ANGUS) with computational fluid dynamics. Arteriosclerosis, thrombosis, and vascular biology. 1997;17(10):2061-5.

136. Kim E, Stamatelos S, Cebulla J, Bhujwalla ZM, Popel AS, Pathak AP. Multiscale imaging and computational modeling of blood flow in the tumor vasculature. Annals of biomedical engineering. 2012;40(11):2425-41.

137. Couffinhal T, Dufourcq P, Barandon L, Leroux L, Duplaa C. Mouse models to study angiogenesis in the context of cardiovascular diseases. Frontiers in bioscience (Landmark edition). 2009;14:3310-25.

138. Doblas S, He T, Saunders D, Pearson J, Hoyle J, Smith N, et al. Glioma morphology and tumor-induced vascular alterations revealed in seven rodent glioma models by in vivo magnetic resonance imaging and angiography. Journal of magnetic resonance imaging : JMRI. 2010;32(2):267-75.

139. Zhang HF, Maslov K, Li ML, Stoica G, Wang LV. In vivo volumetric imaging of subcutaneous microvasculature by photoacoustic microscopy. Optics express. 2006;14(20):9317-23.

140. Fu D, Ye T, Matthews TE, Chen BJ, Yurtserver G, Warren WS. High-resolution in vivo imaging of blood vessels without labeling. Optics Letters. 2007;32(18):2641-3.

141. Murakami T. Application of the scanning electron microscope to the study of the fine distribution of the blood vessels. Archivum histologicum Japonicum = Nihon soshikigaku kiroku. 1971;32(5):445-54.

142. Folarin AA, Konerding MA, Timonen J, Nagl S, Pedley RB. Three-dimensional analysis of tumour vascular corrosion casts using stereoimaging and micro-computed tomography. Microvascular research. 2010;80(1):89-98.

143. Ghanavati S, Yu LX, Lerch JP, Sled JG. A perfusion procedure for imaging of the mouse cerebral vasculature by X-ray micro-CT. Journal of neuroscience methods. 2014;221:70-7.

144. Manelli A, Sangiorgi S, Binaghi E, Raspanti M. 3D analysis of SEM images of corrosion casting using adaptive stereo matching. Microscopy research and technique. 2007;70(4):350-4.

145. Baroldi G, Mantero O, Scomazzoni G. The collaterals of the coronary arteries in normal and pathologic hearts. Circulation research. 1956;4(2):223-9.

146. Krucker T, Lang A, Meyer EP. New polyurethane-based material for vascular corrosion casting with improved physical and imaging characteristics. Microscopy research and technique. 2006;69(2):138-47.

147. Barger AC, Beeuwkes R, 3rd, Lainey LL, Silverman KJ. Hypothesis: vasa vasorum and neovascularization of human coronary arteries. A possible role in the pathophysiology of atherosclerosis. The New England journal of medicine. 1984;310(3):175-7.

148. Vasquez SX, Gao F, Su F, Grijalva V, Pope J, Martin B, et al. Optimization of microCT imaging and blood vessel diameter quantitation of preclinical specimen vasculature with radiopaque polymer injection medium. PloS one. 2011;6(4):e19099.

149. Arribas SM, Daly CJ, González MC, McGrath JC. Imaging the vascular wall using confocal microscopy. The Journal of Physiology. 2007;584(1):5-9.

150. Drake CJ, Fleming PA. Vasculogenesis in the day 6.5 to 9.5 mouse embryo. Blood. 2000;95(5):1671-9.

151. Chaturvedi K, Sarkar DK. Isolation and characterization of rat pituitary endothelial cells. Neuroendocrinology. 2006;83(5-6):387-93.

152. Berger R, Albelda SM, Berd D, Ioffreda M, Whitaker D, Murphy GF. Expression of platelet-endothelial cell adhesion molecule-1 (PECAM-1) during melanoma-induced angiogenesis in vivo. Journal of cutaneous pathology. 1993;20(5):399-406.

153. Vermeulen PB, Gasparini G, Fox SB, Toi M, Martin L, McCulloch P, et al. Quantification of angiogenesis in solid human tumours: an international consensus on the methodology and criteria of evaluation. European journal of cancer (Oxford, England : 1990). 1996;32a(14):2474-84.

154. Ritman EL. Molecular imaging in small animals—roles for micro-CT. Journal of Cellular Biochemistry. 2002;87(S39):116-24.

155. Savai R, Langheinrich AC, Schermuly RT, Pullamsetti SS, Dumitrascu R, Traupe H, et al. Evaluation of Angiogenesis Using Micro-Computed Tomography in a Xenograft Mouse Model of Lung Cancer. Neoplasia (New York, NY). 2009;11(1):48-56.

156. Chugh BP, Lerch JP, Yu LX, Pienkowski M, Harrison RV, Henkelman RM, et al. Measurement of cerebral blood volume in mouse brain regions using micro-computed tomography. NeuroImage. 2009;47(4):1312-8.

157. Daneyemez M. Microangiographic changes following cerebral contusion in rats. Neuroscience. 1999;92(2):783-90.

158. Rennie MY, Whiteley KJ, Kulandavelu S, Adamson SL, Sled JG. 3D visualisation and quantification by microcomputed tomography of late gestational changes in the arterial and venous feto-placental vasculature of the mouse. Placenta. 2007;28(8-9):833-40.

159. Weyers JJ, Carlson DD, Murry CE, Schwartz SM, Mahoney WM, Jr. Retrograde perfusion and filling of mouse coronary vasculature as preparation for micro computed tomography imaging. Journal of visualized experiments : JoVE. 2012(60):e3740.

160. Young SW, Hollenberg NK, Kazam E, Berkowitz DM, Hainen R, Sandor T, et al. Resting host and tumor perfusion as determinants of tumor vascular responses to norepinephrine. Cancer research. 1979;39(6 Pt 1):1898-903.

161. Pathak AP, Kim E, Zhang J, Jones MV. Three-Dimensional Imaging of the Mouse Neurovasculature with Magnetic Resonance Microscopy. PloS one. 2011;6(7):e22643.

162. Marxen M, Sled JG, Yu LX, Paget C, Henkelman RM. Comparing microsphere deposition and flow modeling in 3D vascular trees. American Journal of Physiology - Heart and Circulatory Physiology. 2006;291(5):H2136-H41.

163. d'Esposito A, Nikitichev D, Desjardins A, Walker-Samuel S, Lythgoe MF. Quantification of light attenuation in optically cleared mouse brains. Journal of biomedical optics. 2015;20(8):80503.

164. Bies C, Lehr CM, Woodley JF. Lectin-mediated drug targeting: history and applications. Advanced drug delivery reviews. 2004;56(4):425-35.

165. Sharon N, Lis H. Lectins as cell recognition molecules. Science (New York, NY). 1989;246(4927):227-34.

166. Jilani SM, Murphy TJ, Thai SN, Eichmann A, Alva JA, Iruela-Arispe ML. Selective binding of lectins to embryonic chicken vasculature. The journal of histochemistry and cytochemistry : official journal of the Histochemistry Society. 2003;51(5):597-604.

167. Porter GA, Palade GE, Milici AJ. Differential binding of the lectins Griffonia simplicifolia I and Lycopersicon esculentum to microvascular endothelium: organ-specific localization and partial glycoprotein characterization. European Journal of Cell Biology. 1990;51(1):85-95.

168. Debbage PL, Griebel J, Ried M, Gneiting T, DeVries A, Hutzler P. Lectin intravital perfusion studies in tumor-bearing mice: micrometer-resolution, wide-area mapping of microvascular labeling, distinguishing efficiently and inefficiently

perfused microregions in the tumor. The journal of histochemistry and cytochemistry : official journal of the Histochemistry Society. 1998;46(5):627-39.

169. Lyer PN, Wilkinson KD, Goldstein LJ. An -N-acetyl-D-glycosamine binding lectin from Bandeiraea simplicifolia seeds. Archives of biochemistry and biophysics. 1976;177(1):330-3.

170. Laitinen L. Griffonia simplicifolia lectins bind specifically to endothelial cells and some epithelial cells in mouse tissues. The Histochemical journal. 1987;19(4):225-34.

171. Beisker W, Dolbeare F, Gray JW. An improved immunocytochemical procedure for high-sensitivity detection of incorporated bromodeoxyuridine. Cytometry. 1987;8(2):235-9.

172. Noden DM. Embryonic origins and assembly of blood vessels. The American review of respiratory disease. 1989;140(4):1097-103.

173. Conway EM, Collen D, Carmeliet P. Molecular mechanisms of blood vessel growth. Cardiovascular research. 2001;49(3):507-21.

174. Pettersson A, Nagy JA, Brown LF, Sundberg C, Morgan E, Jungles S, et al. Heterogeneity of the angiogenic response induced in different normal adult tissues by vascular permeability factor/vascular endothelial growth factor. Laboratory investigation; a journal of technical methods and pathology. 2000;80(1):99-115.

175. Maniotis AJ, Folberg R, Hess A, Seftor EA, Gardner LM, Pe'er J, et al. Vascular channel formation by human melanoma cells in vivo and in vitro: vasculogenic mimicry. The American Journal of Pathology. 1999;155(3):739-52.

176. http://www.lungevity.org/.

177. Folkman J. Tumor angiogenesis: therapeutic implications. The New England journal of medicine. 1971;285(21):1182-6.

178. Virchow R. Die krankhaften Geschwulste1863.

179. Thiersch C. Der Epithelialkrebs namentlich der Haut1865.

180. Baish JW, Jain RK. Fractals and cancer. Cancer research. 2000;60(14):3683-8.

181. Shang B, Cao Z, Zhou Q. Progress in tumor vascular normalization for anticancer therapy: challenges and perspectives. Frontiers of medicine. 2012;6(1):67-78.

182. Arap W, Pasqualini R, Ruoslahti E. Cancer treatment by targeted drug delivery to tumor vasculature in a mouse model. Science (New York, NY). 1998;279(5349):377-80.

183. Pasqualini R. Vascular targeting with phage peptide libraries. The quarterly journal of nuclear medicine : official publication of the Italian Association of Nuclear Medicine (AIMN) [and] the International Association of Radiopharmacology (IAR). 1999;43(2):159-62.

184. Ferrara N, Hillan KJ, Novotny W. Bevacizumab (Avastin), a humanized anti-VEGF monoclonal antibody for cancer therapy. Biochemical and biophysical research communications. 2005;333(2):328-35.

185. Di Costanzo F, Mazzoni F, Micol Mela M, Antonuzzo L, Checcacci D, Saggese M, et al. Bevacizumab in non-small cell lung cancer. Drugs. 2008;68(6):737-46.

186. Heath VL, Bicknell R. Anticancer strategies involving the vasculature. Nature reviews Clinical oncology. 2009;6(7):395-404.

187. Tozer GM, Kanthou C, Baguley BC. Disrupting tumour blood vessels. Nature reviews Cancer. 2005;5(6):423-35.

188. Pettit GR, Cragg GM, Singh SB. Antineoplastic agents, 122. Constituents of Combretum caffrum. Journal of natural products. 1987;50(3):386-91.

189. Thorpe PE, Chaplin DJ, Blakey DC. The first international conference on vascular targeting: meeting overview. Cancer research. 2003;63(5):1144-7.

190. Lin CM, Singh SB, Chu PS, Dempcy RO, Schmidt JM, Pettit GR, et al. Interactions of tubulin with potent natural and synthetic analogs of the antimitotic agent combretastatin: a structure-activity study. Molecular pharmacology. 1988;34(2):200-8.

191. Chaplin DJ, Pettit GR, Hill SA. Anti-vascular approaches to solid tumour therapy: evaluation of combretastatin A4 phosphate. Anticancer research. 1999;19(1a):189-95.

192. Dark GG, Hill SA, Prise VE, Tozer GM, Pettit GR, Chaplin DJ. Combretastatin A-4, an agent that displays potent and selective toxicity toward tumor vasculature. Cancer research. 1997;57(10):1829-34.

193. Landuyt W, Verdoes O, Darius DO, Drijkoningen M, Nuyts S, Theys J, et al. Vascular targeting of solid tumours: a major 'inverse' volume-response relationship following combretastatin A-4 phosphate treatment of rat rhabdomyosarcomas. European journal of cancer (Oxford, England : 1990). 2000;36(14):1833-43.

194. Chan LS, Malcontenti-Wilson C, Muralidharan V, Christophi C. Alterations in vascular architecture and permeability following OXi4503 treatment. Anti-Cancer Drugs. 2008;19(1):17-22.

195. Salmon HW, Mladinich C, Siemann DW. Evaluations of vascular disrupting agents CA4P and OXi4503 in renal cell carcinoma (Caki-1) using a silicon based microvascular casting technique. European Journal of Cancer. 2006;42(17):3073-8.

196. Salmon HW, Siemann DW. Effect of the second-generation vascular disrupting agent OXi4503 on tumor vascularity. Clinical cancer research : an official journal of the American Association for Cancer Research. 2006;12(13):4090-4.

197. Wankhede M, Dedeugd C, Siemann DW, Sorg BS. In vivo functional differences in microvascular response of 4T1 and Caki-1 tumors after treatment with OXi4503. Oncology reports. 2010;23(3):685-92.

198. El-Emir E, Boxer GM, Petrie IA, Boden RW, Dearling JL, Begent RH, et al. Tumour parameters affected by combretastatin A-4 phosphate therapy in a human colorectal xenograft model in nude mice. European journal of cancer (Oxford, England : 1990). 2005;41(5):799-806.

199. Fanelli M, Locopo N, Gattuso D, Gasparini G. Assessment of tumor vascularization: immunohistochemical and non-invasive methods. The International journal of biological markers. 1999;14(4):218-31.

200. Gijtenbeek JM, Wesseling P, Maass C, Burgers L, van der Laak JA. Three-dimensional reconstruction of tumor microvasculature: simultaneous visualization of multiple components in paraffin-embedded tissue. Angiogenesis. 2005;8(4):297-305.

201. McDonald DM, Choyke PL. Imaging of angiogenesis: from microscope to clinic. Nature Medicine. 2003;9(6):713-25.

202. Qutub AA, Mac Gabhann F, Karagiannis ED, Vempati P, Popel AS. Multiscale Models of Angiogenesis: Integration of Molecular Mechanisms with Cell- and Organ-Level Models. IEEE engineering in medicine and biology magazine : the quarterly magazine of the Engineering in Medicine & Biology Society. 2009;28(2):14-31.

203. McDougall SR, Anderson ARA, Chaplain MAJ, Sherratt JA. Mathematical modelling of flow through vascular networks: Implications for tumour-induced angiogenesis and chemotherapy strategies. Bulletin of Mathematical Biology.64(4):673-702.

204. Secomb TW, Hsu R, Dewhirst MW, Klitzman B, Gross JF. Analysis of oxygen transport to tumor tissue by microvascular networks. International journal of radiation oncology, biology, physics. 1993;25(3):481-9.

205. Mac Gabhann F, Ji JW, Popel AS. Computational model of vascular endothelial growth factor spatial distribution in muscle and pro-angiogenic cell therapy. PLoS computational biology. 2006;2(9):e127.

206. Lee J, Smith NP. Theoretical modeling in hemodynamics of microcirculation. Microcirculation (New York, NY : 1994). 2008;15(8):699-714.

207. Popel AS, Johnson PC. Microcirculation and Hemorheology. Annual review of fluid mechanics. 2005;37:43-69.

208. Hua J, Sheng Y, Pinney KG, Garner CM, Kane RR, Prezioso JA, et al. Oxi4503, a novel vascular targeting agent: effects on blood flow and antitumor activity in comparison to combretastatin A-4 phosphate. Anticancer research. 2003;23(2b):1433-40.

209. Dearling JL, Flynn AA, Qureshi U, Whiting S, Boxer GM, Green A, et al. Localization of radiolabeled anti-CEA antibody in subcutaneous and intrahepatic colorectal xenografts: influence of tumor size and location within host organ on antibody uptake. Nuclear medicine and biology. 2009;36(8):883-94.

210. http://www.lgcstandards-atcc.org/?geo_country=gb.

211. Tomayko MM, Reynolds CP. Determination of subcutaneous tumor size in athymic (nude) mice. Cancer chemotherapy and pharmacology. 1989;24(3):148-54.

212. Jonkman JE, Swoger J, Kress H, Rohrbach A, Stelzer EH. Resolution in optical microscopy. Methods in enzymology. 2003;360:416-46.

213. El Emir E, Qureshi U, Dearling JL, Boxer GM, Clatworthy I, Folarin AA, et al. Predicting response to radioimmunotherapy from the tumor microenvironment of colorectal carcinomas. Cancer research. 2007;67(24):11896-905.

214. Sheng Y, Hua J, Pinney KG, Garner CM, Kane RR, Prezioso JA, et al. Combretastatin family member OXI4503 induces tumor vascular collapse through the induction of endothelial apoptosis. International journal of cancer. 2004;111(4):604-10.

215. Jain RK, Tong RT, Munn LL. Effect of vascular normalization by antiangiogenic therapy on interstitial hypertension, peritumor edema, and lymphatic metastasis: insights from a mathematical model. Cancer research. 2007;67(6):2729-35.

216. Wu J, Long Q, Xu S, Padhani AR. Study of tumor blood perfusion and its variation due to vascular normalization by anti-angiogenic therapy based on 3D angiogenic microvasculature. Journal of biomechanics. 2009;42(6):712-21.

217. Hori SS, Gambhir SS. Mathematical model identifies blood biomarker-based early cancer detection strategies and limitations. Science translational medicine. 2011;3(109):109ra16.

218. Pries AR, Höpfner M, le Noble F, Dewhirst MW, Secomb TW. The shunt problem: control of functional shunting in normal and tumour vasculature. Nature reviews Cancer. 2010;10(8):587-93.

219. Dewhirst MW, Richardson R, Cardenas-Navia I, Cao Y. The relationship between the tumor physiologic microenvironment and angiogenesis. Hematology/oncology clinics of North America. 2004;18(5):973-90, vii.

220. Jain RK. Antiangiogenic therapy for cancer: current and emerging concepts. Oncology (Williston Park, NY). 2005;19(4 Suppl 3):7-16.

221. Bibby MC. Orthotopic models of cancer for preclinical drug evaluation: advantages and disadvantages. European Journal of Cancer. 2004;40(6):852-7.

222. Johnson JI, Decker S, Zaharevitz D, Rubinstein LV, Venditti JM, Schepartz S, et al. Relationships between drug activity in NCI preclinical in vitro and in vivo models and early clinical trials. British Journal of Cancer. 2001;84(10):1424-31.

223. Kozlowski JM, Fidler IJ, Campbell D, Xu ZL, Kaighn ME, Hart IR. Metastatic behavior of human tumor cell lines grown in the nude mouse. Cancer research. 1984;44(8):3522-9.

224. Schenk WG, McDonald JC, McDonald K, Drapanas T. Direct Measurement of Hepatic Blood Flow in Surgical Patients: With Related Observations on Hepatic Flow Dynamics in Experimental Animals. Annals of Surgery. 1962;156(3):463-9.

225. http://www.wisegeek.com.

226. Forner A, Llovet JM, Bruix J. Hepatocellular carcinoma. Lancet (London, England). 2012;379(9822):1245-55.

227. Kabbach G, Assi HA, Bolotin G, Schuster M, Lee HJ, Tadros M. Hepatobiliary Tumors: Update on Diagnosis and Management. Journal of Clinical and Translational Hepatology. 2015;3(3):169-81.

228. Bird NC, Mangnall D, Majeed AW. Biology of colorectal liver metastases: A review. Journal of surgical oncology. 2006;94(1):68-80.

229. Schnitzbauer AA, Lang SA, Goessmann H, Nadalin S, Baumgart J, Farkas SA, et al. Right portal vein ligation combined with in situ splitting induces rapid left

lateral liver lobe hypertrophy enabling 2-staged extended right hepatic resection in small-for-size settings. Annals of Surgery. 2012;255(3):405-14.

230. Jin S, Fu Q, Wuyun G, Wuyun T. Management of post-hepatectomy complications. World Journal of Gastroenterology : WJG. 2013;19(44):7983-91.

231. Van den Eynde M, Hendlisz A. Treatment of colorectal liver metastases: a review. Reviews on recent clinical trials. 2009;4(1):56-62.

232. Soo CS, Chuang VP, Wallace S, Charnsangavej C, Carrasco H. Treatment of hepatic neoplasm through extrahepatic collaterals. Radiology. 1983;147(1):45-9.

233. Lin G, Lunderquist A, Hagerstrand I, Boijsen E. Postmortem examination of the blood supply and vascular pattern of small liver metastases in man. Surgery. 1984;96(3):517-26.

234. Haugeberg G, Strohmeyer T, Lierse W, Bocker W. The vascularization of liver metastases. Histological investigation of gelatine-injected liver specimens with special regard to the vascularization of micrometastases. Journal of cancer research and clinical oncology. 1988;114(4):415-9.

235. Paku S, Lapis K. Morphological aspects of angiogenesis in experimental liver metastases. The American Journal of Pathology. 1993;143(3):926-36.

236. Terayama N, Terada T, Nakanuma Y. A morphometric and immunohistochemical study on angiogenesis of human metastatic carcinomas of the liver. Hepatology. 1996;24(4):816-9.

237. Yang Y-Y, Lin H-C. Alteration of intrahepatic microcirculation in cirrhotic livers. Journal of the Chinese Medical Association.78(8):430-7.

238. DeVita V, Hellman, S, Rosenberg, SA. Cancer, principles and practice of oncology. Philadelphia: Lippincott-Raven Publ. Co; 1997.

239. Breedis C, Young G. The Blood Supply of Neoplasms in the Liver. The American Journal of Pathology. 1954;30(5):969-85.

240. Choyke PL, Dwyer AJ, Knopp MV. Functional tumor imaging with dynamic contrast-enhanced magnetic resonance imaging. Journal of magnetic resonance imaging : JMRI. 2003;17(5):509-20.

241. Nathan P, Zweifel M, Padhani AR, Koh DM, Ng M, Collins DJ, et al. Phase I trial of combretastatin A4 phosphate (CA4P) in combination with bevacizumab in patients with advanced cancer. Clinical cancer research : an official journal of the American Association for Cancer Research. 2012;18(12):3428-39.

242. Maniam S, Szklaruk J. Magnetic resonance imaging: Review of imaging techniques and overview of liver imaging. World journal of radiology. 2010;2(8):309-22.

243. Coolen BF, Moonen RP, Paulis LE, Geelen T, Nicolay K, Strijkers GJ. Mouse myocardial first-pass perfusion MR imaging. Magnetic resonance in medicine. 2010;64(6):1658-63.

244. Makowski M, Jansen C, Webb I, Chiribiri A, Nagel E, Botnar R, et al. First-pass contrast-enhanced myocardial perfusion MRI in mice on a 3-T clinical MR scanner. Magnetic resonance in medicine. 2010;64(6):1592-8.

245. Raleigh JA, Chou SC, Arteel GE, Horsman MR. Comparisons among pimonidazole binding, oxygen electrode measurements, and radiation response in C3H mouse tumors. Radiation research. 1999;151(5):580-9.

246. Braverman MS, Braverman IM. Three-Dimensional Reconstructions of Objects from Serial Sections Using a Microcomputer Graphics System. Journal of Investigative Dermatology. 1986;86(3):290-4.

247. Mohun TJ, Weninger WJ. Imaging heart development using high-resolution episcopic microscopy. Current opinion in genetics & development. 2011;21(5-2):573-8.

248. Renier N, Wu Z, Simon DJ, Yang J, Ariel P, Tessier-Lavigne M. iDISCO: a simple, rapid method to immunolabel large tissue samples for volume imaging. Cell. 2014;159(4):896-910.

249. Yang B, Treweek Jennifer B, Kulkarni Rajan P, Deverman Benjamin E, Chen C-K, Lubeck E, et al. Single-Cell Phenotyping within Transparent Intact Tissue through Whole-Body Clearing. Cell.158(4):945-58.

250. Scheuer W, van Dam GM, Dobosz M, Schwaiger M, Ntziachristos V. Drug-based optical agents: infiltrating clinics at lower risk. Science translational medicine. 2012;4(134):134ps11.

251. Dobosz M, Ntziachristos V, Scheuer W, Strobel S. Multispectral fluorescence ultramicroscopy: three-dimensional visualization and automatic quantification of tumor morphology, drug penetration, and antiangiogenic treatment response. Neoplasia. 2014;16(1):1-13.

252. Pastrana E. Imaging life with thin sheets of light. Nature Methods. 2012;9(1):37-.

253. Pitrone PG, Schindelin J, Stuyvenberg L, Preibisch S, Weber M, Eliceiri KW, et al. OpenSPIM: an open-access light-sheet microscopy platform. Nature methods. 2013;10(7):598-9.

254. Greger K, Swoger J, Stelzer EH. Basic building units and properties of a fluorescence single plane illumination microscope. The Review of scientific instruments. 2007;78(2):023705.

255. Stuurman N. Computer Control of Microscopes using μManager. Current Protocols of Molecular Biology. 2010;Chapter:Unit 14.20.